Northern Cascadia Marine Gas Hydrate:
Constraints from Resistivity, Velocity, and AVO

by

Marc-André Paul Chen
B.Sc. McGill University, 2003

A Thesis Submitted in Partial Fulfillment of the
Requirements for the Degree of

MASTER OF SCIENCE

in the School of Earth and Ocean Sciences

Northern Cascadia Marine Gas Hydrate:
Constraints from Resistivity, Velocity, and AVO

by

Marc-André Paul Chen
B.Sc. McGill University, 2003

Supervisory Committee

Dr. Roy D. Hyndman (School of Earth and Ocean Sciences)
Supervisor

Dr. George D. Spence (School of Earth and Ocean Sciences)
Co-Supervisor

Dr. Stan E. Dosso (School of Earth and Ocean Sciences)
Departmental Member

Dr. Michael Riedel (Department of Earth and Planetary Sciences, McGill University)
Additional Member

Dr. Earl E. Davis (Pacific Geoscience Centre, Geological Survey of Canada)
External Examiner

Supervisory Committee

Dr. Roy D. Hyndman (School of Earth and Ocean Sciences)
Supervisor

Dr. George D. Spence (School of Earth and Ocean Sciences)
Co-Supervisor

Dr. Stan E. Dosso (School of Earth and Ocean Sciences)
Departmental Member

Dr. Michael Riedel (Department of Earth and Planetary Sciences, McGill University)
Additional Member

Dr. Earl E. Davis (Pacific Geoscience Centre, Geological Survey of Canada)
External Examiner

ABSTRACT

This thesis presents estimates of marine gas hydrate distribution and concentration obtained from various geophysical methods. The study area is located in the accretionary prism of the Northern Cascadia subduction zone, offshore Vancouver Island, Canada. The primary objective of this study was to assess the applicability of a suite of geophysical methods in estimating marine gas hydrate distribution and concentration. The measurements tested are downhole log electrical resistivity and seismic velocity, multi-channel seismic (MCS) velocity, and seismic amplitude vs. offset (AVO) of a gas hydrate-related bottom-simulating reflection (BSR). The downhole log data are from Integrated Ocean Drilling Program Expedition 311, along a transect of four wells, and the seismic data are from a conventional 2-D MCS line along the well transect.

Gas hydrate distribution and concentration estimates along the well transect exhibit high spatial variability, both from site to site, and within any given site. On average, estimates from electrical resistivity measurements give 5-15% gas hydrate pore space saturation, whereas velocity-based estimates are 15-25%. Some intervals in both cases show

concentrations over 40%. Nonlinear Bayesian inversion of seismic AVO data yields a gas hydrate concentration estimate of 0-23% of the pore space.

These results lead to the conclusion that resistivity and velocity data are effective tools for estimating marine gas hydrate concentration. The main uncertainty in the resistivity analysis is the in situ pore fluid salinity, whereas the main uncertainty in the velocity study is the magnitude of the bulk sediment velocity increase associated with gas hydrate occurrence (related to how gas hydrate forms). It is shown here that AVO of a gas hydrate BSR is not a useful method to estimate marine gas hydrate concentration. The method lacks the shear-wave velocity resolution necessary to add useful constraints to what is already known from compressional-wave velocity information.

RÉSUMÉ

Cette thèse présente des estimations de la distribution et de la concentration de l'hydrate de gaz marin, en utilisant de différentes méthodes géophysiques. L'emplacement de l'étude est sur la pente continentale de l'ouest canadien, à la latitude de l'île de Vancouver. L'objectif principal de l'étude était d'évaluer l'applicabilité de plusieurs méthodes géophysiques dans l'estimation de la distribution et de la concentration de l'hydrate de gaz marin. Les données géophysiques testées sont des levés de puits électriques et séismiques, ainsi des levés séismiques marins, utilisés pour obtenir des données de vélocité et d'amplitude en fonction de d'angle (AVO). Les données de puits ont été recueillies par Integrated Ocean Drilling Program, durant l'Expédition 311, où quatre puits ont été forés en croisé de la pente continentale. Les données séismiques marines utilisées proviennent d'un levé 2-D traversant les quatre puits.

Les estimations de la distribution et la concentration de l'hydrate de gaz aux quatre puits démontrent beaucoup de variations spatiales. En moyenne, les estimations provenant des données de résistivité électrique sont d'environ 5-15% de la porosité occupée par l'hydrate de gaz, tandis que les données de vélocité résultent en concentrations moyennes d'environ 15-25%. Certaines zones dans les puits démontrent des concentrations au delà

de 40%, dans les deux cas. La concentration d'hydrate de gaz calculée par l'inversion non-linéaire de données AVO est de 0-23% de la porosité occupée par l'hydrate de gaz. Ces résultats démontrent que l'étude de la résistivité et de la vélocité sont des moyens appropriés pour estimer la concentration d'hydrate de gaz dans l'emplacement marin. L'incertitude principale au niveau de la résistivité est la salinité in situ de l'eau présente dans les sédiments, tandis que l'incertitude principale au niveau de la vélocité concerne l'effet qu'a l'emplacement de l'hydrate de gaz sur la vélocité des sédiments en question. Cette étude démontre que la méthode AVO n'est pas un moyen efficace pour estimer la concentration d'hydrate de gaz dans les sédiments marins. Cette méthode manque de résolution au niveau de la vélocité d'ondes de cisaillement, et n'ajoute pas d'information à l'information que nous a fournit la l'étude des ondes de compression.

Table of contents

List of Tables

List of Figures

Acknowledgments

I would first like to thank my supervisor Roy Hyndman for the support and help he has continuously lent me throughout this project. I would also like to thank my committee members George Spence, Stan Dosso, and Michael Riedel, for all their insightful suggestions during my thesis.

I would also like to thank several individuals for helpful scientific discussions, particularly Ele Willoughby, Ross Haake, Ranjan Dash, Andrew McNeill, Evan Bianco, Ross Chapman, Pat Hart, Tim Collett, Dave Goldberg, and Alberto Malinverno. Thanks also to Andy Calvert, who lent archived data that would otherwise have been very difficult and time consuming to retrieve.

Thanks to Ikuko, Lucinda, and Sabine for all the shared carpooling miles to PGC.

Many thanks to NSERC and University of Victoria for fellowship funding.

I would also like thank my friends, particularly all my great roommates at 3561 Quadra, who have helped make my stay on the west coast very memorable. Thanks Tony, Dennis, Marina, Zach, Sabine, and Carrol!

Finalement, j'aimerais remercier mes parents, Monique et Peter, pour avoir encouragé mon intérêt pour les sciences dès un jeune âge.

Chapter 1

Introduction

1.1 Overview and Objectives

In this thesis, results from downhole well log and multi-channel seismic (MCS) studies are presented in an area of marine gas hydrate occurrence, offshore Vancouver Island, Canada. The study area is located on the continental slope, in the accretionary prism of the Northern Cascadia subduction zone. The primary objective of the study is to measure gas hydrate distribution and concentration, based on the effect of gas hydrate occurrence on measurable bulk sediment physical properties.

Geophysical log and core data were collected along a well transect in the study area during Integrated Ocean Drilling Program (IODP) Expedition 311 in September-October 2005. Electrical resistivity and seismic velocity logs are analyzed in conjunction with other log and core sample data collected during the drilling expedition, to obtain quantitative estimates of gas hydrate concentration. A 2-D MCS line along the well transect was collected in 1989, prior to Ocean Drilling Program (ODP) Leg 146. These data provide an independent measure of velocity at the well sites and adjacent areas, also used to estimate gas hydrate concentration. In related work, the MCS data is used for

amplitude vs. offset (AVO) analysis of gas hydrate-related bottom-simulating reflections (BSRs), to estimate gas hydrate and free gas concentrations above and below.

Chapter 1 of this thesis is an introduction to marine gas hydrate, and provides general background information on the subject. The second chapter reviews the models used to describe how the occurrence of gas hydrate in marine sediments affects the physical properties of those sediments. Chapters 3 and 4 are dedicated to the analysis of downhole electrical resistivity and seismic velocity, two methods providing independent measures of gas hydrate distribution and concentration. In Chapter 5, AVO analyses of gas hydrate-related seismic reflections are presented. Chapter 6 discusses the results and conclusions from the well log, MCS velocity, and AVO studies.

1.2 Gas Hydrate: Definition, Stability and Occurrence

Gas hydrate is a solid substance consisting of a water lattice in which hydrocarbon molecules (most often methane) are embedded. The occurrence of marine gas hydrate is limited by its temperature and pressure stability field, which usually includes the top few hundred meters of sediments on continental slopes (Figure 1.1), where low temperature and high pressure conditions exist. Below the base of the stability zone, where temperatures are too high for gas hydrate to exist, methane occurs as free gas in concentrations greater than solubility. Gas hydrate can substantially increase sediment electrical resistivity and seismic velocity, and therefore may be detected and quantified by seismic and electrical surveys and measurements. Regionally, its presence can be inferred by a prominent BSR on low-frequency seismic sections (Figure 1.2), which marks the base of the gas hydrate stability zone (GHSZ, e.g., Hyndman and Spence, 1992; Andreassen et al., 1997; Yuan et al., 1999). BSRs are observed in reflection

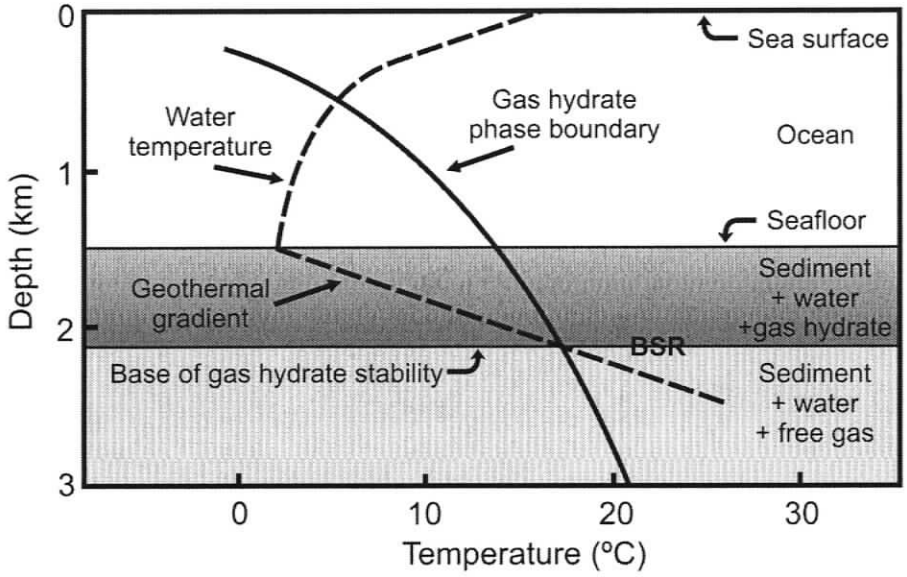

Figure 1.1 Schematic representation of the marine gas hydrate stability zone. Gas hydrate is stable under pressure and temperature conditions to the left of the gas hydrate phase boundary, and to the right, free gas and water are stable.

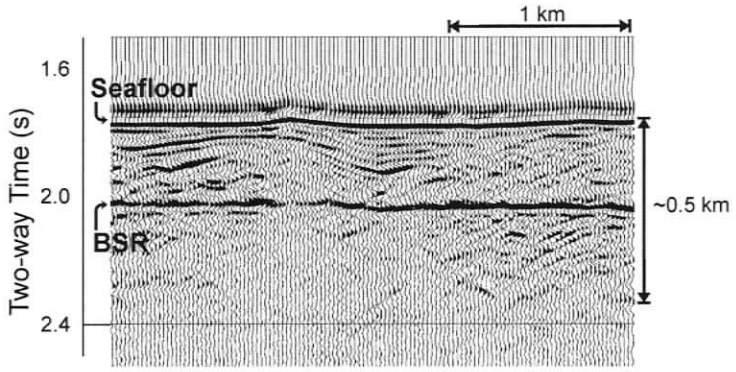

Figure 1.2 Low-frequency seismic section (line 89-08) near IODP Site U1327, showing a bottom-simulating reflection (BSR) that parallels the seafloor, marking the base of the gas hydrate stability zone. The seafloor reflection and BSR are of opposite polarity.

seismic data from continental margins worldwide, especially in subduction zone accretionary prisms (Kvenvolden et al., 1993). They occur as negative polarity reflections (relative to the seafloor), indicating a decrease in acoustic impedance, which is consistent with a transition in sediment pore-space saturation from gas hydrate and water above to free gas and water below the boundary.

1.3 Implications

Although there is substantial disagreement on global estimates of gas hydrate abundance (e.g., Kvenvolden 1993; Collett, 2000; Milkov, 2004), studies generally indicate an enormous amount of methane stored in marine and arctic terrestrial gas hydrate deposits. Interest in these gas hydrate deposits is related to the potential of gas hydrate as a future energy resource, its role in climate change, and its geologic hazard potential.

1.3.1 Future Energy Resource

The world's ever increasing energy demands and the depletion of conventional hydrocarbon reserves in many areas have recently prompted resource exploration in alternative, unconventional deposits, such as oil sands, coal bed methane and shale gas. One consequence of the increasing demand for oil and its decreasing worldwide supply is the growing proportion of the global energy mix held by natural gas (e.g., BP Statistical Review, 2006; Tertzakian, 2006). The main component of natural gas is methane (CH_4), which is the lowest order hydrocarbon, and is therefore one of the cleanest burning fossil fuels. Natural gas has now become an important energy commodity in many countries.

The methane stored in the world's marine and arctic terrestrial gas hydrate deposits are increasingly viewed as a possible unconventional energy resource that could help meet the world's increasing energy demands. Still, there is considerable work to be done in mapping the occurrence and distribution of gas hydrate, and in developing efficient production methods. Recently, the Mallik 2002 Gas Hydrate Production Research Well Program successfully tested natural gas production from permafrost gas hydrate in the Mallik 5L-38 well, MacKenzie Delta, Canada. Tests were made of both a pressure-drawdown method and a thermal stimulation method (Dallimore and Collett, 2005). Gas hydrate dissociation into methane and water was achieved in the depressurization method by lowering the reservoir pressure to conditions outside the stability field of gas hydrate. Similarly gas hydrate was dissociated in the thermal stimulation method by raising reservoir temperatures to conditions outside the stability field of gas hydrate. A third production method involving chemical ("antifreeze") stimulation of a gas hydrate reservoir has not as of yet been tested.

1.3.2 Impact on Climate Change

Ice cores from Antarctica and Greenland have shown cyclical fluctuations in atmospheric temperature over the past 740 k years, paralleled by changes in atmospheric CO_2 and CH_4 concentrations (Petit et al., 1999; Augustin et al., 2004; Andersen et al. 2004). These fluctuations are well correlated with variations is the Earth's orbit, known as Milankovitch cycles. However, since the observed temperature changes cannot be accounted for solely by the slight variations in the amount of solar radiation reaching the Earth, it has been proposed that feedback mechanisms within the Earth's climate system amplify the perturbations caused by Milankovitch cycles. Since gas hydrate represents a

large amount of sequestered carbon, its dissociation, and release of methane, a strong greenhouse gas, into the atmosphere, could represent one such feedback mechanism (e.g., Haq, 2000).

One suggested feedback mechanism is that low sea levels during glacial maxima could reduce hydrostatic pressure enough to initiate marine gas hydrate dissociation, which would cause an increase in oceanic and atmospheric methane concentration. The increased amount of greenhouse gas supplied to the atmosphere by this process could in turn increase atmospheric temperatures, thereby triggering a negative response to advancing glaciation (Paull et al., 1991). Initially, this process is only sustainable at low latitudes: at higher latitudes, the low temperatures caused by the glaciation favor the stability of gas hydrate. However, even a small increase in temperature caused by the dissociation of low-latitude gas hydrate can cause further dissociation of near-surface gas hydrate (i.e., permafrost gas hydrate) and amplified greenhouse warming (Haq, 2000). After a certain time lag, the warming could induce increases in ocean-bottom temperature, further favoring the dissociation of marine gas hydrate.

Because of its potential impact on future climate change, gas hydrate has been the subject of numerous climate modeling studies (e.g., Harvey and Huang, 1995; Archer and Buffett, 2005; Fyke, 2005). Results from these studies generally suggest that future warming causing increased ocean-bottom temperatures could significantly decrease the global volume of the GHSZ, producing a long-lasting effect on the global carbon cycle.

1.3.3 Geohazard Potential

It has been hypothesized that the dissociation of marine gas hydrate can cause weaknesses in continental margin sediments and lead to submarine landslides. Slope

failure occurs when the shear stress exerted on the sediments exceeds the strength of those sediments. Factors affecting the stress exerted on sediments include earthquakes and slope over-steepening from sediment deposition, whereas the sediment strength is affected by diagenesis and sediment pore pressure, amongst others (Paull et al., 2000). A slope failure therefore occurs as a result of a combination of factors.

The formation and dissociation of gas hydrate in marine sediments is thought to significantly affect sediment mechanical properties: if present in large enough quantities, the replacement of liquid water with solid gas hydrate could increase sediment shear strength. Conversely, the dissociation of gas hydrate can decrease sediment shear strength. Furthermore, since the volume of water and methane produced by the dissociation of gas hydrate is greater than the volume of gas hydrate from which it originated, the dissociation can increase pore pressure, further weakening the sediment (Kayen and Lee, 1991).

As of yet, no documented submarine landslides have been proven to be triggered by gas hydrate dissociation. However, much speculation has been made about their association, since gas hydrate-related BSRs are commonly observed in seismic images of sediments around slide scars (e.g., Dillon et al., 1993; Booth et al., 1994). Dillon et al. (2001) suggested seafloor collapse features observed at Blake Ridge to be related to gas hydrate occurrence. They postulated that free gas trapped beneath the base of the GHSZ caused overpressures in those sediments, eventually leading to their mobilization. This in turn would have triggered subsidence within the strata of the GHSZ, by normal faulting, gravity gliding, and folding. A further example is the Storrega slide on the Norwegian continental margin, which is one of the largest known submarine landslides, and has been

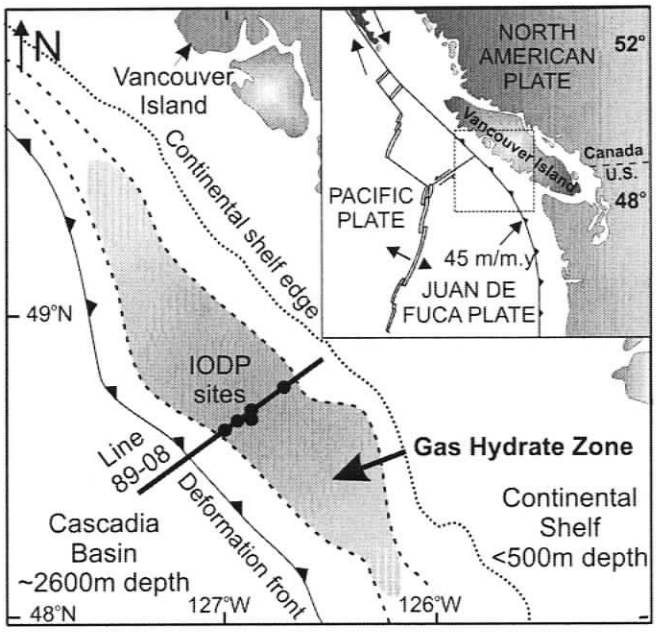

Figure 1.3 Map of the Northern Cascadia gas hydrate area, with IODP Expedition 311 drill sites and MCS line 89-08 indicated. After Expedition 311 Scientists (2005).

associated with an 11 m high tsunami on the Norwegian coast 7200 years ago (Bondevik et al., 1997). It too is surrounded by sediments where a gas hydrate-related BSR is observed (e.g., Bünz et al., 2003; Bünz et al., 2005).

1.4 Gas Hydrate in Northern Cascadia

1.4.1 Tectonic Setting

The Northern Cascadia gas hydrate area is located in the accretionary prism of the Cascadia subduction zone (Figure 1.3), where the Juan de Fuca oceanic plate subducts beneath the North American continental plate at ~45 mm/year (Riddihough, 1984). In the Cascadia Basin, seaward of the deformation front, a ~2500 m thick layer of sediments overlay the oceanic plate. They consist of pre-Pleistocene hemipelagic sediments overlain by Pleistocene turbidites (Davis and Hyndman, 1989). Most of the Cascadia Basin

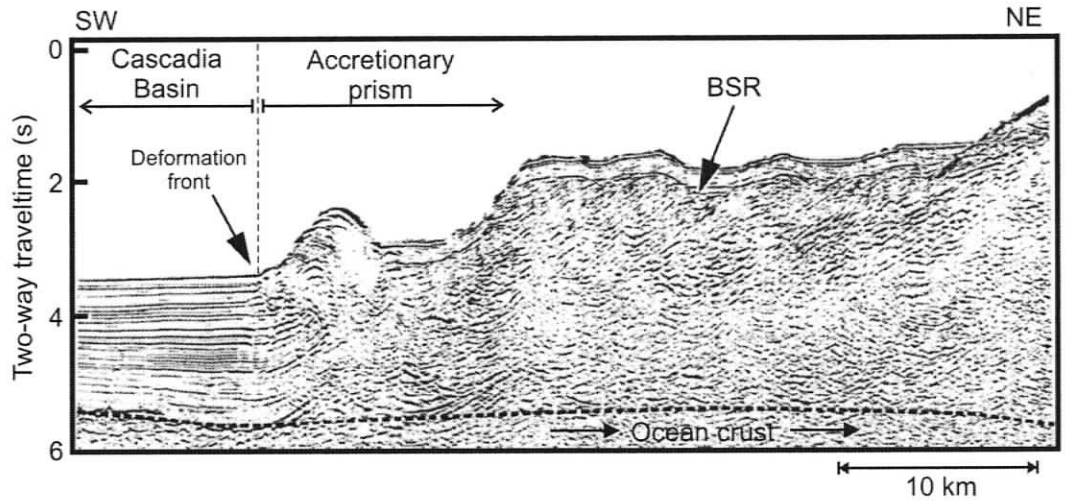

Figure 1.4 Seismic cross section of the Northern Cascadia accretionary prism (line 89-08). The deformation front marks the boundary between the undeformed sediments of the Cascadia Basin, and the deformed sediments of the accretionary prism. After Hyndman et al. (2001).

sediments entering the subduction zone are scraped off the oceanic crust, and are accreted to the North American plate in the accretionary prism, which is delimited seaward by the deformation front and landward by the Eocene volcanic Cresent Terrane. The sediments entering the accretionary prism undergo increased tectonic deformation and thickening by folding and thrust faulting, as they progress landward. As the sediment deformation in the accretionary prism progresses, sedimentation continues, and an irregular blanket of undeformed, slope basin sediments, recently deposited in place, accumulates on top of the accreted Cascadia Basin sediments, favorably infilling local topographic lows. Figure 1.4 shows a seismic cross section through the Northern Cascadia accretionary prism.

1.4.2 Fluid Expulsion Model

The fluid expulsion model proposed by Hyndman and Davis (1992) explains the occurrence of marine gas hydrate in accretionary prism sediments by the migration of (biogenic) methane into the GHSZ by upward fluid advection from deep within the accretionary prism. The fluid expulsion is thought to occur as a consequence of sediment deformation, compaction, and dewatering landward of the deformation front. As the methane-bearing fluids migrate upwards and enter the GHSZ, the methane reacts with the pore water to form gas hydrate (Figure 1.5). The fluid expulsion model predicts the highest concentrations of gas hydrate to be located at or near the base of the GHSZ, with a gradational decrease in concentration upwards, towards the seafloor.

A process that would further focus gas hydrate occurrence near the base of the GHSZ is the so-called mechanism of gas hydrate "recycling" (e.g., Minshull et al., 1994; Pecher et al., 1996). As accretionary prisms grow by continued sediment accretion and deposition of new sediment at the seafloor, the base of the GHSZ is continually moving upwards through the sediment. Consequently, gas hydrate immediately above the base of the GHSZ eventually dissociates into free gas and water as the base of the GHSZ moves upward. The mobile free gas then migrates upwards, by fluid advection, back into the GHSZ, where it reacts with water to form gas hydrate again. If the reaction generally occurs soon after the free gas enters the GHSZ, such a process would tend to focus gas hydrate near the base of the GHSZ.

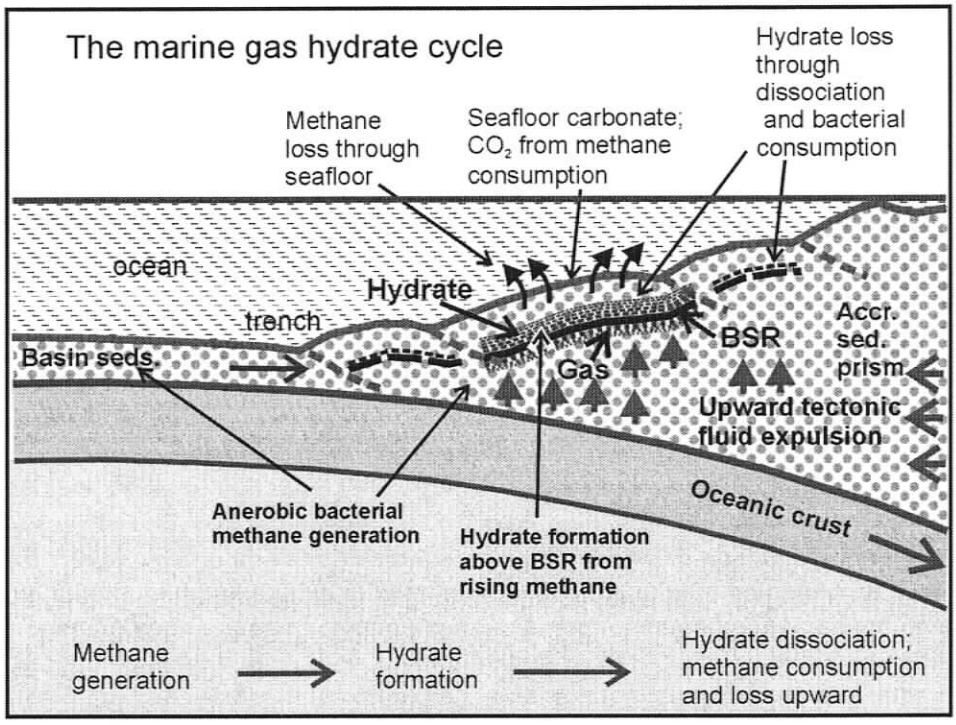

Figure 1.5 Schematic representation of the marine gas hydrate cycle, according to the fluid expulsion model. After Hyndman et al. (2001).

1.4.3 Other Controls

Recent findings from IODP Expedition 311 have suggested that factors other than the distance from the base of the GHSZ may also control gas hydrate occurrence and distribution. During the expedition, sandier intervals with high gas hydrate concentration were discovered well above the base of the GHSZ (Riedel et al., 2006), suggesting that grain size and associated sediment parameters, such as permeability, are also factors that control the occurrence of gas hydrate. Directly observed gas hydrate from recovered core samples occurred either as pore fill in sandier layers, or in the form of small nodules, lenses, veins, or as fracture-fill, by displacing the surrounding sediment, a process also known as microheave. Gas hydrate occurrence was also inferred by the observation of

sediment fabric disturbances (soupy and mousselike textures), associated with the dissociation of gas hydrate during core recovery. Other gas hydrate indicators included core liner infrared temperature anomalies and core pore fluid salinity reduction (Riedel et al., 2006).

These observations have led to the conclusion that gas hydrate occurrence is strongly lithologically controlled, and that the availability of a suitable host formation (i.e., coarse-grained sediments) is a key factor (Riedel et al., 2005). The requirement of a coarse-grained host formation is probably related to permeability control on fluid flow. IODP Expedition 311 geochemical analyses suggest that local methane solubility and fluid and gas advection rates are other controlling factors.

1.5 Recent Geophysical Studies

The Northern Cascadia accretionary prism is one of the most thoroughly studied marine gas hydrate areas. Seismic experiments include 2-D and 3-D MCS and single-channel seismic (SCS), over a wide range of frequencies (e.g., Hyndman and Spence, 1992; Fink and Spence, 1999; Riedel et al., 2002), high-resolution seismic surveying with a deep-towed array (Gettrust et al., 1999; Chapman et al., 2002), and ocean-bottom seismometer (OBS) experiments (Hobro et al., 2005). To characterize the gas hydrate distribution, various methods have been used to analyze the available seismic data, including (1) estimation of BSR reflection coefficients (Hyndman and Spence, 1992; Yuan et al., 1996), (2) normal moveout (NMO) velocity analysis (Yuan et al., 1996), (3) AVO modeling of BSR reflections (Hyndman and Spence, 1992; Yuan et al., 1999), (4) full waveform inversion (Singh and Minshull, 1994; Yuan et al., 1996), and (5) modeling the frequency dependence of the BSR (Chapman et al., 2002). Other regional mapping

methods used include seafloor electrical surveys, i.e., controlled-source electromagnetic (CSEM, Yuan and Edwards, 2000; Schwalenberg et al., 2005) and seafloor compliance studies (Willoughby and Edwards, 2000; Latychev and Edwards, 2003; Willoughby et al., 2006).

These regional surveys have been complemented by two drilling expeditions. ODP Leg 146 involved wireline (WL) logging and coring at one gas hydrate site (Site 889/890), in the accretionary prism, and at one reference site (Site 888), seaward of the deformation front. Most recently, a transect of four well sites across the accretionary prism was completed during IODP Expedition 311 (U1325, U1326, U1327 near Site 889/890, and U1329), in addition to an active cold vent site (U1328). An assessment of the scientific results is available in the Expedition 311 Report (Riedel et al., 2006). The primary objective of the expedition was to constrain gas hydrate formation models in subduction zone accretionary prisms. Specific goals related to the primary objective included (1) studying the mechanisms by which gas hydrate forms in marine sediments, (2) measuring gas hydrate distribution and defining the nature of the BSR, (3) examining the effect of gas hydrate occurrence on sediment physical properties, and (4) providing a ground truth for regional geophysical experiments. To meet these objectives, the general approach taken was to drill three holes at each site.

The first hole employed logging-while-drilling (LWD) methods to provide downhole geophysical data and to identify gas hydrate zones in order to develop an optimal coring strategy for subsequent holes. The LWD logging recorded formation resistivity, porosity, density, and natural gamma radiation along the entire depth of the hole. Since the logging tools were attached directly above the drill bit, measurements at

near in situ conditions were recorded. However, no reliable velocity or nuclear magnetic resonance (NMR) logs were recorded during LWD operations. Formation washout causing enlarged borehole diameter is much less serious for LWD, compared to conventional WL logs. As is generally the case, logs in intervals with degraded hole conditions (washouts) must be disregarded in the interpretation, or at least used with caution, as many of the tools require close proximity to the borehole wall for accurate measurements. The caliper tool measures borehole diameter, and provides a qualitative indication of hole conditions.

The second hole was usually cored in its entirety. The suite of shipboard core measurements included infrared images of core liner temperature, porosity, and wet and dry density from moisture and density (MAD) analysis, detailed geochemical analyses of interstitial water, gas geochemisty (from headspace and void gas), and detailed lithostratigraphic description of the core.

The third hole was generally dedicated to the deployment of special pressure coring tools, followed by conventional WL logging. The pressure coring allowed for laboratory measurements to be done on core samples under in situ pressure conditions. Furthermore, methane gas released by gas hydrate dissociation during core recovery was captured in the core barrel, and measured onboard the ship. The WL logging recorded compressional (P-) and shear (S-) wave velocity, resistivity and natural gamma radiation. WL logging is conducted after the drilling is completed, so a significant amount of time passes between drilling and logging; as a consequence, the recorded logs may not be representative of in situ conditions. Unfortunately, the caliper arm broke off the WL logging sonde, due to excessive ship heave, so hole conditions were not recorded in any

of the WL holes. Additionally, the porosity tool requires the instrument pad be pressed against the borehole wall for accurate measurements, which is achieved by pressing the caliper arm against the opposite side of the hole. Without a caliper, no useable log porosity measurements were obtained in the WL holes. Another limitation of open-hole (uncased) WL logging in unconsolidated marine sediments is that the drill pipe cannot be removed from the upper section of the hole at any point during the operations, so as to prevent extensive hole degradation. Many of the logs, including velocity and resistivity, cannot be recorded through the drill pipe, so the upper ~70 m of open-hole WL holes are generally not logged.

Concerning the relative quality of LWD vs. WL logs, LWD logs are prefereable, because they generally have less hole stability problems, and they measure formation properties at near in situ conditions. However, LWD logging is a relatively recent technology, and the logging tools have not benefited from the same technological evolution than have conventional WL logs. Notably, LWD sonic tools do not, as of yet, yield consistently reliable formation velocity information, and the variety of tools available to measure resistivity is much less. There is currently much new effort in industry to develop better LWD tools.

The IODP Expedition 311 well transect was drilled along MCS line 89-08 (Figures 1.3 and 1.4), acquired by Digicon Geophysical Corporation for the Geological Survey of Canada in 1989, prior to ODP Leg 146. The conventional MCS survey was acquired with a tuned airgun array with a total volume of 125 L (7820 $inch^3$), and shots were recorded by a 3600 m streamer with 144 hydrophones. The shot point interval was 50 m, giving CDPs with 36-fold multiplicity, and bin spacing of 12.5 m. In addition to

providing information about regional stratigraphy and structure, independent velocity information complementing downhole velocity logs can be obtained from MCS data with normal moveout (NMO) analysis (e.g., Yuan et al. (1996) obtained detailed NMO velocities across ODP Site 889/890). In this study, new NMO velocities from line 89-08 are obtained at the four sites of the IODP Expedition 311 well transect (Chapter 4). Additionally, the BSR observed in MCS line 89-08 is used in an AVO analysis near Site U1327, in an attempt to estimate gas hydrate and free gas concentrations immediately above and below the BSR.

The general approach taken in this study, for both log and seismic data, is to accompany all analyses with quantitative error estimates, in order to obtain realistic uncertainty bounds on reported gas hydrate and free gas concentrations.

Chapter 2

Physical Properties of Gas Hydrate-Bearing Sediments

The inclusion of gas hydrate in marine sediments usually changes the physical properties of the bulk sediment substantially. Gas hydrate can take on many forms, including small nodules, lenses, veins, fracture-filling, and pore-filling. In the simplest model, rising methane reacts with the sediment pore fluid to form gas hydrate, partially replacing the pore fluid (i.e., pore-filling), but with little change to the sediment structure or volume. More complex models involve gas hydrate crystal growth by displacement of the ambient sediment (microheave), in the form of veins, fracture-fill, small nodules or lenses.

Gas hydrate has different physical properties than the pore fluid it commonly replaces; notably, its electrical resistivity and seismic velocity are significantly greater. The presence of gas hydrate in the pore space of marine sediments can therefore significantly affect the bulk physical properties of the sediment. To a first approximation, the velocity of gas hydrate is similar to the sediment matrix, i.e., faster than the pore fluid it replaces. Gas hydrate is also electrically resistive, similar to the sediment matrix, and in contrast with the conductive, saline pore fluid it replaces. Therefore, as measured by velocity or resistivity, the effect of gas hydrate occurrence is, to first order, similar to that

of replacing the pore fluid with matrix-like material, i.e., reducing the porosity. In more complex models, gas hydrate occurrence can also cause seismic and electrical anisotropy in sediments, if they occur in sandier layers, fractures, or veins. One physical property that is not greatly affected by the occurrence of gas hydrate is density, since the density of gas hydrate is typically much closer to the pore fluid density than the matrix density. In a pore fluid replacement model, the density can therefore serve as a no-hydrate reference measurement.

The electrical resistivity, seismic velocity and bulk density of sediments can be measured geophysically (e.g., seismic data, seafloor electrical surveys, well logs), and can be used to estimate gas hydrate concentration. In this chapter, empirical relations and physical models relating gas hydrate concentration to bulk sediment physical properties are explored. These models are used in the following chapters (3, 4, and 5) to estimate gas hydrate concentration from geophysical measurements of these physical properties.

2.1 Gas Hydrate and Electrical Resistivity

In this section, empirical relations between sediment porosity, resistivity, and gas hydrate saturation are developed. These relations are used in Chapter 3 to estimate gas hydrate saturation from IODP Expedition 311 log resistivity data.

2.1.1 Archie's Relation

A basis for most rock resistivity studies was provided by Archie (1942), who examined sandstone cores from the U.S. Gulf Coast region. He empirically established that the resistivity of a fully water-saturated sediment R_o is closely proportional to R_w, the resistivity of the pore fluid:

$$R_o = FR_w, \tag{2.1}$$

where the proportionality constant F is called the formation factor. Furthermore, by examining core samples from different formations, Archie established an exponential empirical relationship between F and the porosity φ:

$$F = \frac{R_o}{R_w} = \varphi^{-m}, \tag{2.2}$$

where the exponent m was determined to be formation specific. The exponent m was found to vary between 1.8 and 2.0 in consolidated sandstones, and values near 1.3 were obtained for unconsolidated sands. Since m depends on the state of consolidation, it is called the cementation exponent.

Winsauer et al. (1952) modified Archie's original equation by including a coefficient a in the relation:

$$F = \frac{R_o}{R_w} = a\varphi^{-m}. \tag{2.3}$$

From a physical standpoint, a should be unity, since when $\varphi = 1$, $F = 1$; however, since Equations 2.2 and 2.3 are empirical relations, allowing a to vary generally improves the fit between F and φ, since it provides an additional degree of freedom. From a physical perspective, the values of parameters a and m depend on the inter-connectivity of the pore spaces, which in turn depends on lithology, cementation, and grain size distribution (Hearst et al., 2000). Smaller values of a and m are qualitatively indicative of well inter-connected pore spaces (i.e., lower R_o for a given φ and R_w).

Many subsequent studies using downhole log data, core data, and laboratory measurements have confirmed the exponential relation to be a good approximation for

relating resistivity to porosity (e.g., Jackson et al., 1978; Swanson, 1979; Hilfer, 1991; Ioannidis et al., 1997), and adequate for the purpose of this study.

2.1.2 Effect of Partial Gas Hydrate Saturation

When gas hydrate is formed from pore fluid, the salts in solution are largely excluded. The result is that the electrical resistivity of gas hydrate is much greater than that of saline pore fluid, and gas hydrate occurrence can significantly increase bulk sediment resistivity (e.g., Collett, 2001; Riedel et al., 2005). To first order, gas hydrate may be taken to be non-conductive, as compared to the pore fluid. An empirical relationship describes the effect of non-conductive material in the pore space on resistivity:

$$R_t = R_o S_w^{-n}, \tag{2.4}$$

where R_t is the true, or measured bulk resistivity, S_w is the water saturation (defined as the fraction of the pore space occupied by water), and n is the saturation exponent (Hearst et al., 2000). In the case of partial gas hydrate pore space saturation, the gas hydrate saturation is defined as $S_h = 1 - S_w$. The value of n in Equation 2.4 is a measure of how the occurrence of gas hydrate affects the fully water-saturated resistivity R_o, i.e., the grain-hydrate-fluid structure. If n is relatively large, gas hydrate forms in a way that strongly impedes current flow and increases bulk sediment resistivity (e.g., gas hydrate located in the spaces connecting adjacent pores), whereas if n is relatively small, gas hydrate forms in a way that has a lesser effect on sediment resistivity (e.g., gas hydrate occurrence in the pore space, making minimal contact with sediment grains). Pearson et al., (1983) calculated an estimate for n of 1.94; however, modeling by Spangenberg

(2001) has shown that n depends somewhat on grain size distribution and the gas hydrate saturation itself. Combining Equations 2.3 and 2.4, gives Archie's relation for gas hydrate-bearing sediments (e.g., Collett and Ladd, 2000):

$$R_t = aR_w\varphi^{-m}(1-S_h)^{-n}, \tag{2.5}$$

In practice, for many marine sediments, the pore fluid resistivity R_w usually can be adequately estimated from the equation of state of seawater (Fofonoff, 1985), if in situ pressure, temperature, and salinity are known. Parameters a and m can be estimated empirically by curve fitting F vs. φ data from fully water-saturated samples, using Equation 2.3. Gas hydrate saturation S_h can then be estimated for sediment with porosity φ, and resistivity R_t, if Equation 2.5 is rearranged as

$$S_h = 1-\left[a\frac{R_w}{R_t}\varphi^{-m}\right]^{1/n}. \tag{2.6}$$

Equation 2.6 provides a relationship between gas hydrate saturation and resistivity, which empirically accounts for the sediment porosity, the inter-connectivity of the pore space, and the effect of gas hydrate occurrence on the inter-connectivity of pore space.

2.1.3 Effects of Gas Hydrate Texture and Distribution in Sediment

Findings from IODP Expedition 311 have shown that gas hydrate forms preferentially in coarse-grained sediment, and often occurs in small nodules or fracture-filling veins, displacing the surrounding sediment (Riedel et al., 2006). The Archie analysis makes use of empirical parameters to describe the relationships between sediment resistivity, porosity, and gas hydrate saturation (a, m, and n). Since these

parameters are calibrated empirically, they should, on average, accurately characterize these relationships, but some uncertainty arises from the fact that gas hydrate does not occur homogeneously, throughout a homogeneous medium. For example, if gas hydrate occurred in sheeted fractures, perpendicular to the current direction used to measure sediment resistivity, the measured resistivity would be greater than if the same amount of gas hydrate occurred in sheeted fractures parallel to the current direction (i.e., electrical anisotropy). However, a proper empirical calibration of the saturation exponent n should, on average, adequately account for the mode of gas hydrate formation.

One aspect that is difficult to account for is the local accuracy of the porosity-resistivity relation described by parameters a and m, since it is determined empirically, generally as an average for the entire sediment section considered. If the sands and clays of the section exhibit different porosity-resistivity relations, using values for a and m representative of an "average sediment" might not be accurate, since gas hydrate appears to occur preferentially in sandier intervals. Also, if gas hydrate forms by displacing the surrounding sediment in veins, fractures, and nodules, the porosity-resistivity relation may no longer be entirely accurate, since a and m are estimated from fully water-saturated (undisplaced) sediment.

2.2 Gas Hydrate and Seismic Velocity

The presence of gas hydrate in marine sediments has a substantial effect on sediment P-wave (compressional) velocity. In the simplest approximation, gas hydrate replaces pore fluid, thereby increasing the sediment P-wave velocity. The magnitude of the velocity increase, relative to a no-hydrate reference velocity, provides a method to estimate gas hydrate concentration. Several approaches exist to estimate a no-hydrate

reference velocity profile and to determine the relation between the increase in seismic velocity and gas hydrate concentration. Examined here are (1) empirical porosity-velocity relations used in conjunction with an effective porosity reduction model (e.g., Hyndman et al., 1993; Yuan et al., 1996), (2) time-averaging equations (e.g., Pearson et al., 1983; Lee et al., 1993), and (3) rock-physics modeling (e.g., Dvorkin and Nur, 1993; Helgerud 2001). In Chapter 4, these approaches are applied to seismic velocity data collected at the sites of the IODP Expedition 311 well transect.

2.2.1 Porosity-Velocity Relations and Effective Porosity Reduction

Gas hydrate saturation can be estimated from empirical porosity-velocity relations if gas hydrate is modeled to occur by effective porosity reduction. The porosity reduction model assumes that gas hydrate in the sediment pore space has simply replaced the pore fluid, and reduced the sediment effective porosity (Hyndman et al., 1993; Yuan et al., 1996). The implicit assumption is that the P-wave velocity of pure gas hydrate is similar to that of the sediment matrix. Under this assumption, a bulk sediment velocity measurement can be used to calculate an effective, hydrate-excluding porosity, from an empirical porosity-velocity relation. The effective porosity is then simply subtracted from a hydrate-inclusive porosity measurement (or background porosity) to determine gas hydrate saturation:

$$S_h = \frac{\varphi - \varphi_e}{\varphi}, \tag{2.7}$$

where φ is the gas-hydrate-inclusive, or background porosity, and φ_e is the (hydrate-exclusive) effective porosity, calculated from the porosity-velocity relation. The porosity-

velocity relation can also be used to calculate a background no-hydrate velocity-depth trend from a porosity-depth trend.

Empirical porosity-velocity relations required to calculate φ_e are derived by curve-fitting velocity vs. porosity data (logs or core) in areas known not to contain gas hydrate or free gas (e.g., below the free gas layer, or in the deep basin). For example, Hyndman et al. (1993) derived an empirical porosity-velocity relation from measurements on core samples from ODP Leg 131, Site 808, in the Nankai accretionary prism, taken from well below the base of the GHSZ. Because of the empirical nature of this approach, it is crucial that the porosity-velocity relation used be estimated from sediments similar to those for which gas hydrate saturation is to be estimated.

2.2.2 Time-Averaging Equations

Wyllie et al. (1958) first introduced the idea of time-averaging to estimate sediment porosity from bulk sediment velocity and the velocities of the fluid and matrix components:

$$\frac{1}{V_{wyllie}} = \frac{\varphi}{V_w} + \frac{(1-\varphi)}{V_m}, \tag{2.8}$$

where V_{wyllie} is the bulk sediment velocity, V_w is the velocity of the pore fluid, and V_m is the sediment matrix velocity. The physical basis for time-averaging is that the total traveltime through the bulk sediment is equal to the average traveltime through each component, weighted by the volume fraction of the component. Pearson et al. (1983) extended the two-phase Wyllie equation to a three-phase system containing gas hydrate:

$$\frac{1}{V_1} = \frac{\varphi(1-S_h)}{V_w} + \frac{\varphi S_h}{V_h} + \frac{(1-\varphi)}{V_m}, \tag{2.9}$$

where V_h is the velocity of pure gas hydrate. Wyllie et al. (1958) noted that under certain conditions, time-averaging estimates are inaccurate, notably in the case where sediments are unconsolidated, bulk sediment velocities are overestimated (i.e., porosity underestimated).

Wood (1941) proposed an equation on the other hand that is approximately valid for particles in suspension, i.e., for very high porosity sediments:

$$\frac{1}{\rho_b V_{wood}^2} = \frac{\varphi}{\rho_w V_w^2} + \frac{(1-\varphi)}{\rho_m V_m^2}, \tag{2.10}$$

where ρ_b, ρ_w, and ρ_m are the bulk, fluid, and matrix densities. Like the Wyllie time-average equation, the Wood equation can be extended to a three-phase system with gas hydrate (Lee et al., 1993):

$$\frac{1}{\rho_b V_2^2} = \frac{\varphi(1-S_h)}{\rho_w V_w^2} + \frac{\varphi S_h}{\rho_h V_h^2} + \frac{(1-\varphi)}{\rho_m V_m^2}, \tag{2.11}$$

where ρ_h is the density of pure gas hydrate.

Since the time-average equation (Equation 2.9) applies for consolidated sediments, and the Wood equation (Equation 2.11) applies for particles in suspension, a weighted average of these two solutions (Wyllie dominates at low porosity, Wood dominates at high porosity) should yield reasonable bulk sediment velocities for unconsolidated marine sediments containing gas hydrate (Lee et al., 1993):

$$\frac{1}{V_{Lee}} = \frac{W\varphi(1-S_h)}{V_2} + \frac{1-W\varphi(1-S_h)}{V_1}, \tag{2.12}$$

where W is an arbitrary weighting factor that allows the freedom to bias the result towards either the Wood or Wyllie velocity (i.e., depending on the state of consolidation of the sediments in question). For areas without gas hydrate, Lee et al. (1993) found that

their equation (with S_h set to zero, and W to unity) accurately predicted the measured bulk sediment porosity-velocity relationship for a suite of Deep Sea Drilling Program (DSDP) holes, drilled through unconsolidated sediments on the US Atlantic continental rise.

With knowledge of the velocity and density of the formation constituents, as well as a measurement of sediment porosity, the approach of Lee et al. (1993) provides a means to calculate the expected velocity for sediments with various amounts of gas hydrate. With a porosity-depth trend, a background no-hydrate velocity-depth trend and velocity-depth trends for various gas hydrate saturations can be calculated. However, the introduction of an arbitrary weighting factor adds considerable uncertainty to the results.

2.2.3 Rock-Physics Modeling

An alternative approach to empirical porosity-velocity relations and time-averaging is to derive bulk sediment elastic properties from a rock-physics model (e.g., Dvorkin and Nur, 1993; Carcione and Tinivella, 2000; Helgerud 2001). A comparison of theoretical methods, including various rock-physics models is given by Chand et al. (2004). The rock-physics model used in this study is that of Helgerud (2001) developed for high porosity clay-rich marine sediments.

The approach of Helgerud (2001) was to build a first-principles-based effective medium model for the elastic moduli of high porosity marine sediments containing gas hydrate or free gas. A detailed description of the model is provided in the Appendix. The model requires knowledge of the porosity and of the elastic moduli of the sediment constituents, including gas hydrate, free gas, the pore water, and the sediment grains. A baseline model for fully water-saturated sediments developed by Dvorkin et al. (1999) is used as a starting point. The sediment matrix is modeled as packed spheres, each with 8

grain contacts. The elastic properties of the effective medium composed of the fully water saturated sphere pack is then calculated from first principles. Applied to a porosity-depth profile, this model gives a baseline no-hydrate velocity-depth profile; however, it is relatively sensitive to the mineral assemblage chosen in the modeling.

Elastic properties of effective media containing various amounts of gas hydrate or free gas can then be calculated, according to different assumptions concerning their formation mechanisms. Gas hydrate is modeled either as part of the pore fluid (gas hydrate in-pore), or as part of the load-bearing sediment matrix (gas hydrate in-frame). The gas hydrate in-pore model assumes that the gas hydrate occurs in the sediment pore space, without adding stiffness to the sediment frame. As a consequence, the sediment S-(shear) wave velocity is nearly unaffected by the occurrence of gas hydrate. For the gas hydrate in-frame model, elastic properties of the sediment frame are recalculated, with grains of gas hydrate included as part of the sediment frame. Under this mode of occurrence, gas hydrate adds some stiffness to the sediment frame, and the sediment S-wave velocity is slightly increased by gas hydrate but much less so than for a model in which gas hydrate cements the grain contacts (e.g., Dvorkin and Nur, 1993). Both the gas hydrate in-pore and in-frame models predict an increase in P-wave velocity with increased gas hydrate concentration (slightly more for the gas hydrate in-frame model). Free gas occurrence is modeled to occur in-pore, so its presence in the pore space does not affect the sediment rigidity (Gassmann, 1951), and the S-wave velocity therefore remains nearly unchanged. P-wave velocities, on the other hand, are significantly reduced by the presence of gas (e.g., Gregory, 1976).

Application of this effective medium model to downhole VSP data from ODP Leg 164 Hole 995 at the Blake-Bahama Ridge gas hydrate site indicated that the gas hydrate in-frame model is most accurate in high porosity clay-rich marine sediments (Helgerud, 2001).

2.2.4 Effects of Gas Hydrate Texture and Distribution in Sediment

Just as in the resistivity analysis, the findings of IODP Expedition 311 concerning the heterogeneous nature of gas hydrate occurrence puts into question some of the assumptions inherent in the three methods used to estimate gas hydrate saturation from seismic velocity. The most important source of uncertainty in all three approaches is the notion of a background no-hydrate velocity-depth trend. Such a trend only truly applies in homogeneous sediment (constant matrix composition), where changes in velocity are caused only by changes in porosity. In a case with interbedded sands and clays, the use of this trend could be inadequate if the true no-hydrate velocity of a sandy unit is significantly different from that of a finer-grained clay interval. For example, if the no-hydrate velocity is greater in the sand than the clay, the use of a background no-hydrate velocity trend will underestimate the true background velocity in the sand, thereby overestimating gas hydrate saturation in that sand.

The inherent assumption in the effective porosity reduction approach is that gas hydrate occurs by replacing pore fluid and reducing sediment porosity. This assumption holds to first order, even under circumstances where gas hydrate displaces the ambient sediment, since the velocity of gas hydrate is much closer to that of the sediment constituents than that of the pore water. Additional uncertainty arises from the use of a porosity-velocity relation empirically derived from an average of gas hydrate-free

sediments, since gas hydrate appears to occur preferentially in sandier sediments, rather than clays. The effective porosity reduction approach is therefore only accurate if the sands and clays in question have similar porosity-velocity relations.

Uncertainty in the time-averaging approach arises from the use of the arbitrary weighting factor W, which biases the results towards either the Wyllie or Wood velocity. At high porosity, the Wood velocity should be favoured, since it applies to particles in suspension. However, a high porosity zone containing large amounts of gas hydrate has a low effective porosity, and the Wyllie velocity should be favoured, since the bulk sediment probably behaves more like a consolidated formation. This implies that W depends on the gas hydrate saturation itself, so taking it to be a constant could be a significant source of error.

In all approaches, uncertainty related to the mode of formation of gas hydrate can be significant. At high gas hydrate saturations, where gas hydrate is observed to occur as fracture-filling veins or small nodules that displace the ambient sediment, effective porosity reduction, time-averaging, and gas hydrate modeled in-pore or in-frame may no longer be entirely applicable. The gas hydrate in-pore model is certainly put into doubt, since it assumes that gas hydrate occurs in the pore space without affecting the sediment frame. The gas hydrate in-frame model may also not be applicable in cases where massive gas hydrate occurs and ambient sediment is displaced, since it assumes gas hydrate occurrence as individual grains, equally distributed throughout the sediment frame.

The implications of gas hydrate texture and distribution in sediments on concentration estimates is to some extent also dependent on the scale of the velocity

measurements. Sonic log and MCS velocity measurements have resolutions of ~1 m and ~70 m respectively, whereas gas hydrate nodule, vein or fracture filling textures occur on the order of a few centimetres. The consequence of this scale difference is that the velocity measurements in gas hydrate zones are representative of a weighted average between the velocity in the gas hydrate nodules, veins, or fractures, and the velocity in adjacent sediments.

Chapter 3

Gas Hydrate Concentration from Electrical Resistivity

Downhole electrical resistivity logs can be used to estimate gas hydrate concentration (e.g., Collett and Ladd, 2000; Riedel et al., 2005), since the presence of gas hydrate in sediment pore space significantly increases the bulk sediment resistivity. Equation 2.6, developed in Chapter 2, provides a basis for the calculation of resistivity-based gas hydrate saturation S_h. It requires measurements of electrical resistivity R_t, porosity φ and pore fluid resistivity R_w, as well as the estimation of empirical Archie parameters a, m, and n. The most important difficulty is estimating the in situ pore fluid salinity (i.e., pore fluid resistivity). The salinity measured in recovered cores could include an unknown amount of pore fluid freshening if in situ gas hydrate dissociates upon core recovery. One method, proposed by Hyndman et al. (1999), allows for in situ salinity and gas hydrate concentration to be calculated simultaneously.

IODP Expedition 311 provided a suite of LWD logs, including resistivity, density, and neutron porosity, in addition to several types of core measurements, including porosity, grain density, and interstitial water salinity (Riedel et al., 2006), along a transect of sites across the Northern Cascadia accretionary prism. These data can be used jointly to solve Equation 2.6 for gas hydrate saturation S_h. The use of LWD logs recorded by

tools immediately behind the drill bit provides measurements as close as possible to in situ conditions. This is paramount in gas hydrate studies, since changes in pressure and temperature due to drilling can affect gas hydrate stability. Figure 3.1 is a contour map of seafloor depth, showing the well site locations, and Figure 3.2 is a seismic cross section through the sites.

The approach in this chapter is to solve Archie's equation (Equation 2.6) to determine a gas hydrate saturation profile at each site, while quantifying the uncertainties in (1) the empirical Archie parameters, (2) the in situ salinity, and (3) the appropriate choice of porosity measurement, and their effect on gas hydrate saturation estimates.

3.1 Log and Core Data

3.1.1 Log Resistivity

Downhole formation electrical resistivity data have been obtained from both IODP Expedition 311 and ODP Leg 146, using both conventional and LWD logging tools. For this low-resistivity section of unconsolidated marine sediments, resistivity tools are favoured over induction conductivity tools. The most reliable downhole log resistivity measurement is obtained from the LWD GeoVISION resistivity-at-bit (RAB) tool. The RAB tool is connected directly above the drill bit, and uses two transmitter coils and several electrodes to obtain different measurements of resistivity. Resistivity is measured using a focusing technique: the upper and lower transmitter coils produce currents in the drill collar that meet at the ring electrode. In a homogeneous medium, a net current flow perpendicular to the tool would occur at the ring electrode. This radial current flow becomes distorted in heterogeneous formations, and the current required through the ring

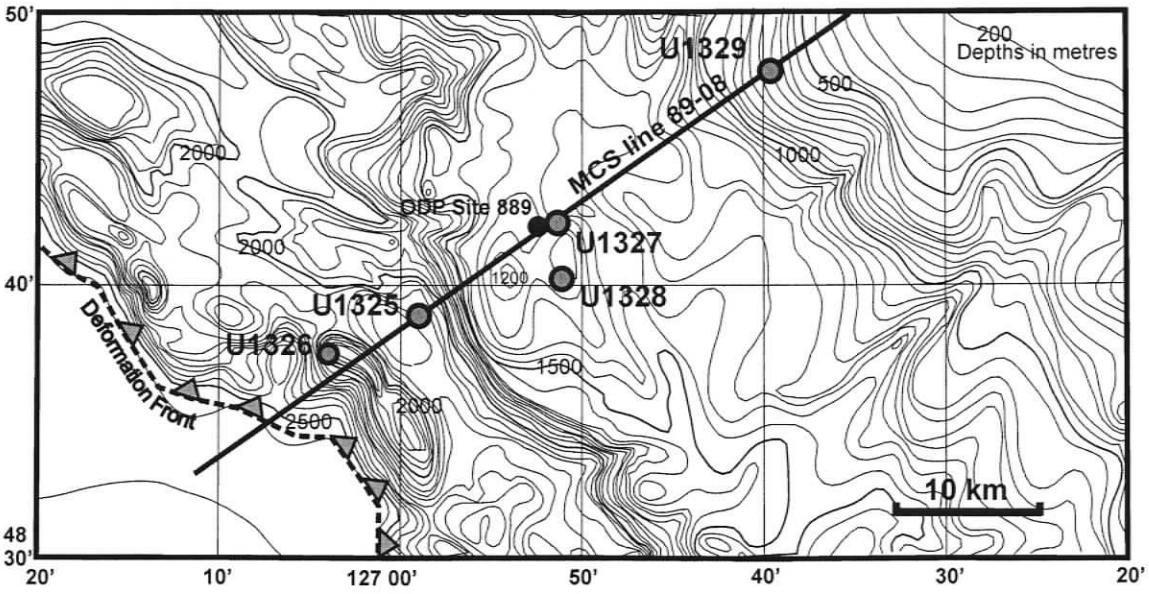

Figure 3.1 Bathymetry map of the Northern Cascadia accretionary prism, showing the locations of IODP Expedition 311 wells and MCS line 89-08, through the well transect. Modified from the IODP Expedition 311 Prospectus (2005).

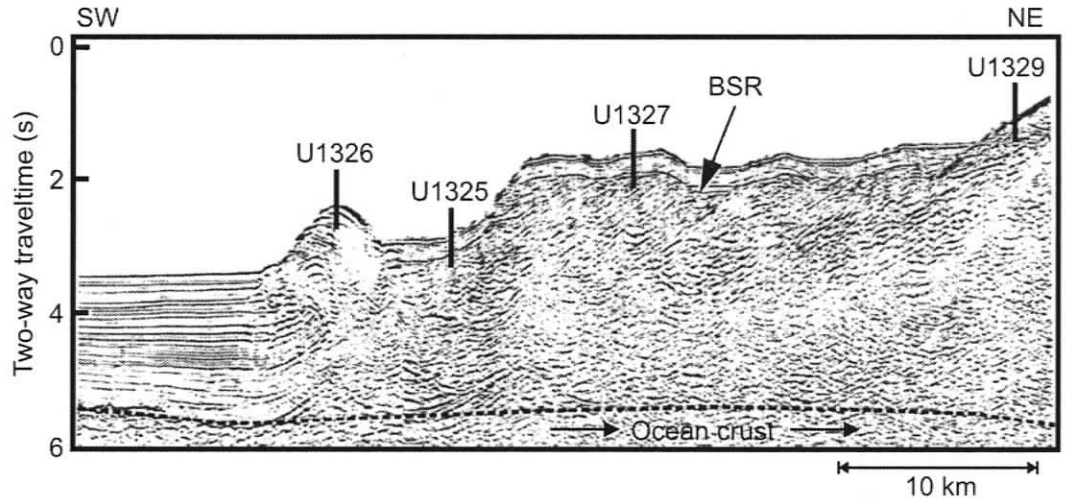

Figure 3.2 Seismic cross section of the Northern Cascadia accretionary prism (line 89-08), showing the location of IODP Expedition 311 well sites U1325, U1326, U1327, and U1329. After Hyndman et al. (2001).

electrode to focus current flow into the formation is related to the formation resistivity (Riedel et al., 2006). This focusing technique is also used to measure resistivity at three button electrodes (corresponding to three depths of investigation: shallow, ~0.3-0.4 m; medium ~0.4-0.5 m; and deep, ~0.4-0.6 m). As the tool rotates in the borehole, the button resistivity is measured about every 6 degrees. The button deep average (BDAV) resistivity, used here as R_t in the Archie analysis, is obtained by averaging the deep button resistivity at a given vertical depth, over the range of azimuthally varying measurements. The BDAV resistivity has a vertical resolution of 5-8 cm, and provides the most accurate measurement of in situ resistivity.

Figure 3.3 shows the BDAV resistivity profiles at the four sites of the IODP Expedition 311 well transect. At each site, the seismically and log inferred BSR depth is shown. Used alone, these resistivity logs qualitatively indicate certain zones of gas hydrate occurrence. High porosity, unconsolidated marine sediments generally have resistivities on the order of 1 Ω-m. Certain zones above the inferred BSR exhibit much higher resistivities, and are therefore interpreted to be gas hydrate bearing, notably at U1326, 73-94 meters below seafloor (mbsf) and 252-261 mbsf; at U1325, in thin layers between 195-240 mbsf; and at U1327, 120-138 mbsf. The presence of gas hydrate near the BSR is inferred by a slight decrease in resistivity from 1.6 to 1.3 Ω-m at U1325, and from 2.4 to 2.0 Ω-m at U1327. Free gas immediately beneath the BSR might slightly increase the resistivity, explaining why no obvious decrease in resistivity at the BSR is observed at U1326 and U1329. However, these two sites both exhibit thin high-resistivity zones immediately above the BSR (255-261 mbsf at U1326, and 120-124 at U1329), probably also related to gas hydrate occurrence. All four sites therefore probably exhibit

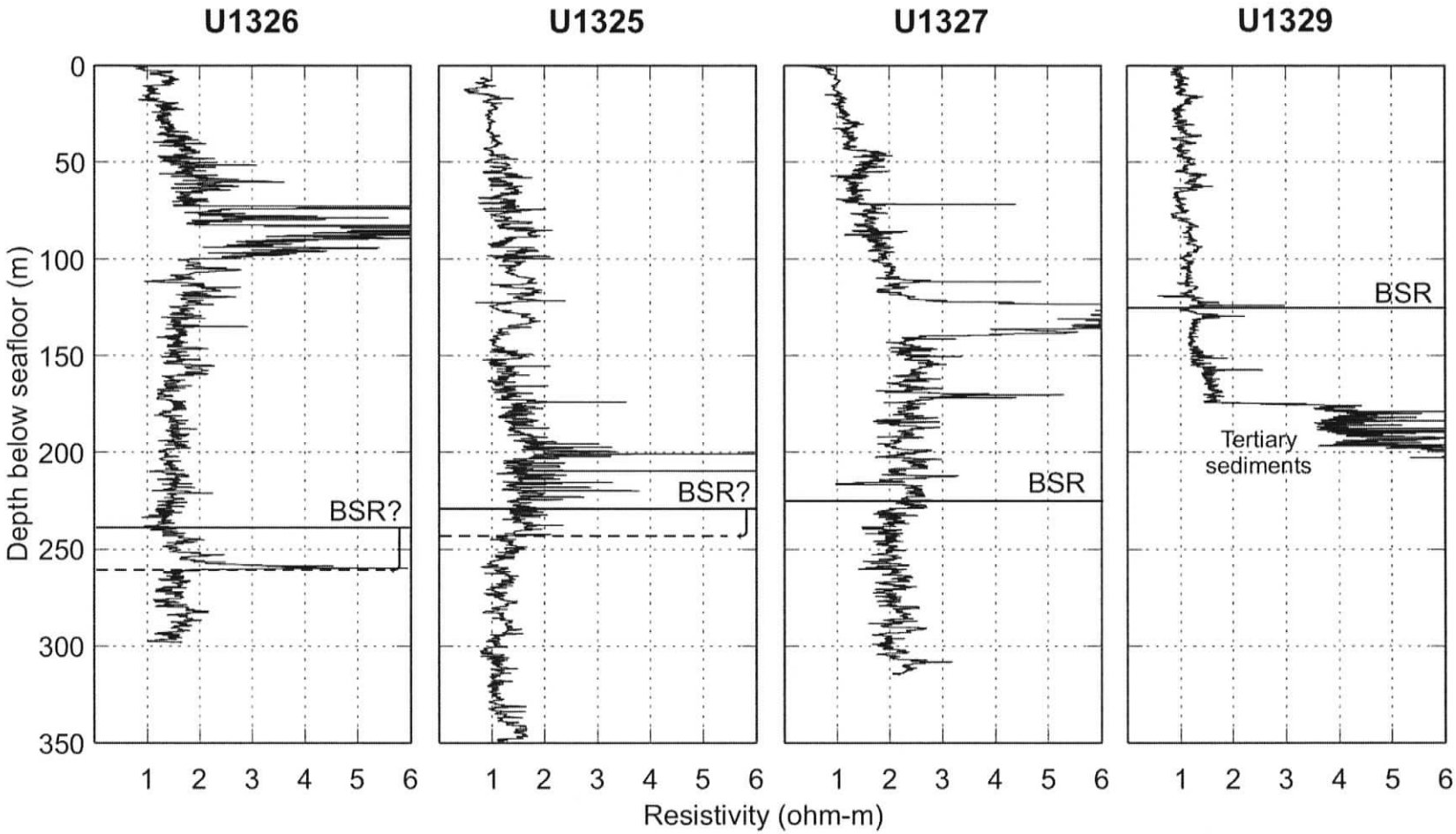

Figure 3.3 Downhole LWD resistivity logs from IODP Expedition 311, at the four sites of the well transect. The seismically inferred BSR is indicated by the solid line. When different, the log-interpreted BSR is shown as a dashed line.

at least a small amount of gas hydrate immediately above the BSR. The high resistivity zone below 176 mbsf at Site U1329 is interpreted to be an unconformity, below which much older, low porosity, lithified Miocene (>6.7 Ma) sediments occur (Riedel et al., 2006).

Figure 3.4 shows the suite of downhole resistivity data collected at Site 889/U1327. Holes 889A, 889B and U1327E were logged with wireline induction tools, whereas hole U1327A used LWD, with the BDAV resistivity shown here. The distance between holes 889A, 889B, and Site U1327 is on the order of 500 m, whereas the distance between holes U1327A and U1327E is only approximately 70 m. The general trend observed at all holes of this site is an increase in resistivity from ~1 Ω-m at the seafloor to ~2 Ω-m at ~120 mbsf; background resistivities of ~2 Ω-m are observed below that depth, with thin higher resistivity zones at different depths in each site. The most dramatic variability between holes is actually between the two most spatially proximal holes (U1327A and U1327E), where consistently higher resistivities (by ~ 0.3 Ω-m) were measured below ~120 m at U1327A, and a high resistivity interval (greater than 5 Ω-m, between 120 and 138 mbsf) was measured only in U1327A. The slight resistivity bias can possibly be explained by the use of different tools to log the hole, or the different time lags between drilling and logging in LWD versus WL. However, the observation of the high resistivity zone (120-138 mbsf) only in U1327A can only be explained by lateral geologic variations.

3.1.2 Core Porosity

To first order, log and core porosity measurements generally respond to gas hydrate as part of the pore space, because the properties that are measured to determine

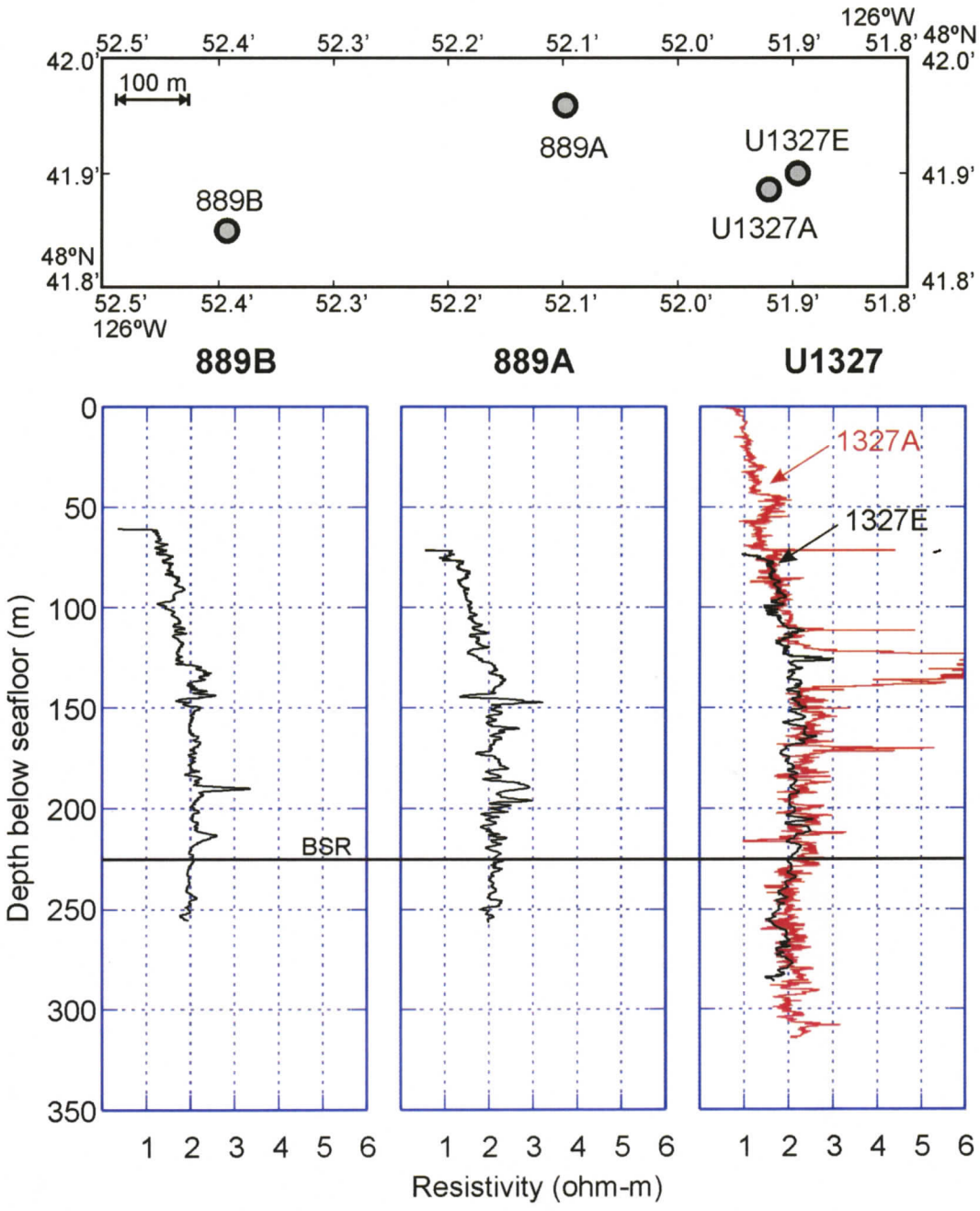

Figure 3.4 Compilation of log resistivity data (WL and LWD) from Sites 889 and U1327. WL resistivity logs were recorded at 889A, 889B, and U1327E, whereas U1327A was recorded by LWD. With the exception of hole 1327A, the resistivities measured are similar between holes.

the porosity are usually similar for gas hydrate and pore water. The available porosity measurements are from the density and neutron logs and from IODP shipboard core moisture and density (MAD) analyses (Figure 3.5).

The MAD-based core porosity was measured as one of the "index" properties on retrieved sediment cores by the IODP Expedition 311 Scientists (Riedel et al., 2006). Wet mass, dry mass and dry volume were measured on push-core samples of ~10 cm^3, to calculate porosity, as described in Blum (1997) and Riedel et al. (2006). Wet mass was measured immediately after the sample was collected, whereas dry mass and volume were measured after the sample was heated at 105 ± 5°C (without vacuum) for 24 hours and allowed to cool in a desiccator. Several biases in free water core porosity measurements must be corrected. There is a bias towards higher porosities, because dry mass and volume were measured on sediments that had been heated to 105°C, a temperature high enough to release some of the bound water in smectite clay (Winters, 2000). Although clays may be somewhat less resistive than the granular component of the sediment matrix, they are usually sufficiently resistive relative to the pore fluid to be included as part of the matrix in electrical resistivity analyses. Other corrections applied were for porosity rebound (Hamilton, 1976; Goldberg et al., 1986) and for residual salt left behind by the evaporated pore water (Blum, 1997). There is also a potential sampling bias, towards lower porosities because porosity could be measured more frequently from more competent (generally less porous) core samples, which have a higher probability of recovery. Since gas hydrate dissociates into water and gas upon core recovery, porosity measurements from core MAD analysis measure in situ gas hydrate as part of the subsequent core pore volume.

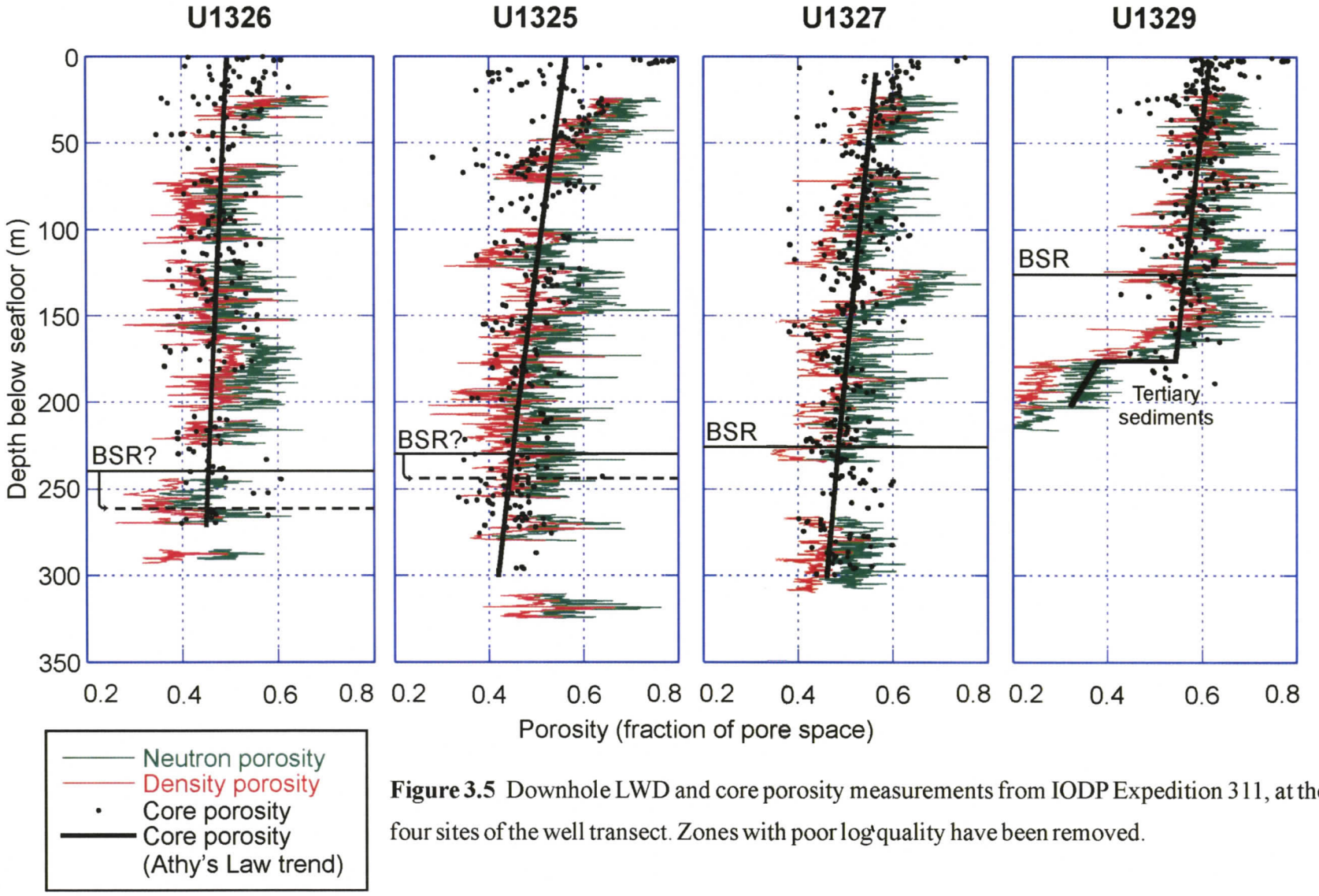

Figure 3.5 Downhole LWD and core porosity measurements from IODP Expedition 311, at the four sites of the well transect. Zones with poor log quality have been removed.

3.1.3 Log Density Porosity

Log density-derived porosities are obtained from the LWD density log by linear interpolation of the formation bulk density ρ_b between the density of water ρ_w, taken to be 1.03 g/cm^3, and the average grain density ρ_g measured in the core MAD analysis:

$$\varphi = \frac{\rho_g - \rho_b}{\rho_g - \rho_w}. \tag{3.1}$$

An average grain density trend was estimated from core at each site, and values ranged from 2680 to 2780 kg/m^3. The variance in grain density measurements gave standard deviation estimates of 30 to100 kg/m^3 that varied from site to site. Note that for the porosity estimate to exclude bound water, the average grain density must include the clay component of the sediment matrix. A log measurement of formation electron density is obtained, based on the reduction in gamma ray flux between a source and a detector on the sonde. The source (^{127}Cs) emits gamma rays into the formation, which are then Compton-scattered by electrons in the formation. A fraction of the emitted gamma-rays are scattered towards a gamma ray counter on the logging tool. The ratio of received to emitted gamma-rays depends on the formation electron density, which is closely proportional to the formation bulk density, because of the well known relation between atomic number and atomic mass. High concentration of certain elements with unusual electron density responses can result in error (Hearst et al., 2000); however, this is not expected to be a problem for the sediments studied. The measurements are calibrated by empirically relating gamma-ray count (i.e., formation bulk density) to core bulk density in a known reference.

The vertical resolution of the density tool used on IODP Expedition 311 was ~15 cm, and the depth of investigation ~10 cm. Even for LWD measurements, the density log must be excluded or used with caution in zones with poor hole conditions, especially where the hole radius is greater than the depth of investigation of the tool. These washout zones can be identified with the caliper tool, which measures hole diameter. The main sources of uncertainty in a high quality density porosity measurement are the statistical uncertainty in the gamma-ray count used to calculate the density, and the uncertainty in the grain density (discussed above). This combined uncertainty is estimated as ± 0.03 porosity units (A. Malinverno, pers. comm. 2006). Since the density of pure gas-hydrate (ρ_h = 0.92) is similar to that of pore water (ρ_w = 1.03) with near seawater salinity, the density porosity calculated from Equation 3.1 measures gas hydrate nearly as part of the pore volume. Even at high gas hydrate concentrations, the assumption that water (instead of gas hydrate) fills the pore space has only a small effect on the calculated porosity (e.g., Riedel et al., 2006).

3.1.4 Log Neutron Porosity

The neutron porosity tool functions by emitting a high energy neutron beam into the formation. As the neutrons pass through the formation, they interact with the ambient atoms, slow down, and are eventually captured. A lower energy neutron detector on the tool detects neutrons that have been slowed by the formation (epithermal neutrons). Neutrons lose the most energy when they collide with atoms of the same mass, so the neutron tool is most sensitive to formation hydrogen concentration (Hearst et al., 2000), and therefore to a first order, water content. The ratio of emitted to detected neutrons is empirically related to porosity through calibration to a known reference, ideally with

similar response to that of the formation studied. Two factors known to cause errors in the neutron porosity measurement are fluid chlorinity and hydrocarbon content. The chlorine atom has an unusually large (neutron) capture cross section, but its effect can be accounted for if the chlorinity is known. In high enough concentrations, the presence of hydrocarbons can cause a positive bias in neutron porosity: since hydrocarbons represent a large amount of hydrogen, they can significantly increase the formation bulk hydrogen concentration if the other main hydrogen component is from the formation water content.

Clay minerals, when present in large enough concentration, can contain a significant amount of bound water that is measured by the neutron porosity tool as pore space, rather than sediment matrix. For this reason, in clay-rich sediments, porosity estimates from neutron logs are generally greater than those from density porosity (given a choice of average grain density in Equation 3.1 that includes clay). With knowledge of the clay content from cores, a correction for bound water content can be applied to the neutron log. The neutron porosity logs shown in Figure 3.5 have been corrected for bound water content by the Expedition 311 Scientists (Riedel et al., 2006), but still have a bias of ~0.06-0.08 greater porosity than the density porosity, probably due to an incomplete correction for bound water content, or other biases that were not adequately accounted for (e.g., chlorinity, hydrocarbon content).

Core porosities seem to generally be greater than log density porosities and less than log neutron porosities, but much closer to the density porosity than to the neutron. However, both the density and neutron porosity logs show similar structure, with more scatter in the neutron porosity. Since gas hydrate is mainly composed of (solid) water, it has a similar hydrogen concentration to that of water, so, to first order, the neutron

porosity measures gas hydrate as part of the pore volume. However, both the methane in gas hydrate and the free gas below the BSR act to slightly increase the measured neutron porosity, because methane has a greater hydrogen concentration than the pore water.

The vertical resolution of the neutron porosity tool used on IODP Expedition 311 was ~30 cm. The depth of investigation is highly dependent on the hydrogen concentration, and is probably less than 20 cm, given the high porosity sediments studied here. For both WL and LWD measurements, the neutron porosity is very sensitive to hole conditions.

The Archie analysis is first undertaken using the log density porosity in Sections 3.2 and 3.3. The density porosity is generally more reliable than the neutron porosity, since the calibration of the neutron porosity contains additional uncertainties related to the effect of unknown amounts of hydrocarbon (including gas hydrate and free gas) on hydrogen concentration, and the high sensitivity of the neutron porosity measurement to hole conditions. The log density porosity is preferred to the core porosities, since the former is measured in the same hole as the LWD resistivity, and because log measurements have more concentrated vertical sampling than core measurements. Section 3.4 considers the sensitivity of results to the different porosity measurements available.

3.2 Determination of Archie Parameters

Archie's law for purely (saline) water saturated sediments is given in Equation 2.3, where R_w can be calculated from the equation of state of seawater (Fofonoff, 1985) or other saline fluid compositions, if the in situ pressure, temperature, and salinity are known. The pressure is taken to be nearly hydrostatic, and the temperature is estimated

from the seafloor temperature and the thermal gradient, and the salinity taken from a smoothed fit through core salinity measurements at the same site (Figure 3.6). In zones inferred to be gas-hydrate-free (i.e., fully water-saturated), the measured core salinity can be assumed to be equal to the in situ salinity. Empirical Archie parameters a and m can then be estimated from a cross-plot of F and φ (Pickett plot) for sediments containing no gas hydrate, in areas with good log quality. Gas-hydrate-free zones are chosen from the undeformed slope basin sediments of holes U1327A and U1329A, where little or no gas hydrate was interpreted (no large spikes in resistivity are observed; as well, slope basin sediments have less time to accumulate gas hydrate in the pore space since they were deposited more recently than the accreted sediments), and from sediments below the inferred BSR in holes U1325A, U1326A, and U1327A (Figure 3.7). Although the sub-BSR zones probably contain a small amount of free gas, which could affect R_t and φ, these zones plot along the same trend in the Pickett plot as the assumed gas-hydrate-free slope basin sediments, so the effect of free gas (in small concentrations) on Archie parameter estimates is small. Also, Hyndman et al. (1999) showed that the porosity-resistivity relation in slope basin and accreted sediments are not significantly different. Here, Archie parameter estimates are obtained by fixing the cementation exponent m to 1.76, a value representative of deep sea sediments (Westbrook et al., 1994). A best fit to the F versus φ data from the gas hydrate-free zones (Figure 3.7) gives an estimate for a of 1.39 ± 0.18 (one-standard-deviation), which is similar to the value obtained by Hyndman et al. (1999) from core porosity and resistivity at ODP Site 889/890. Others (e.g., Riedel et al., 2006) have estimated Archie parameters by fixing a to unity, so that at 100% porosity, $R_w = R_t$. Although this approach has a valid physical basis, fixing $m = 1.76$ and

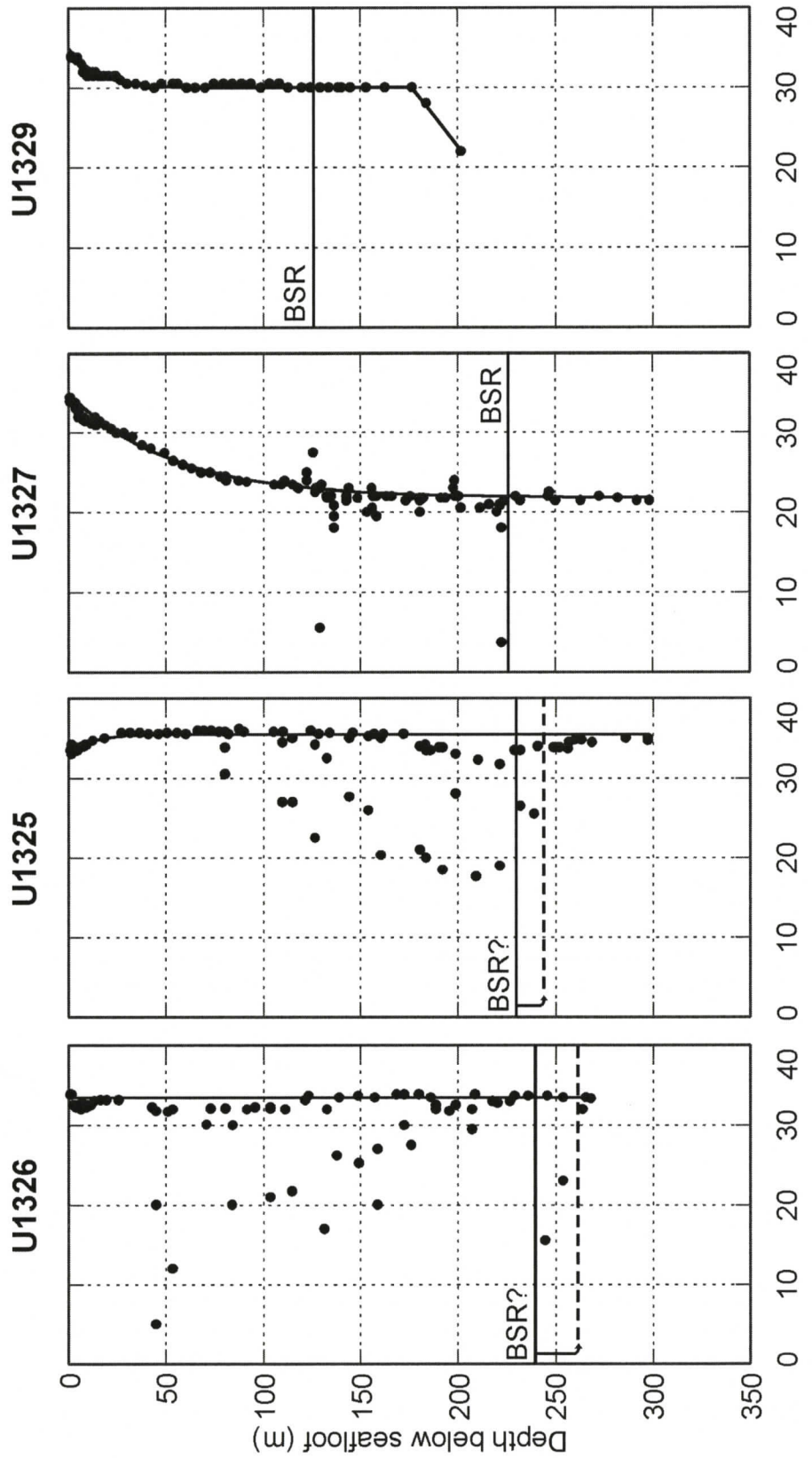

Figure 3.6 Core salinity measurements from IODP Expedition 311, at the four sites of the well transect. The bold trend line is the estimated core salinity baseline.

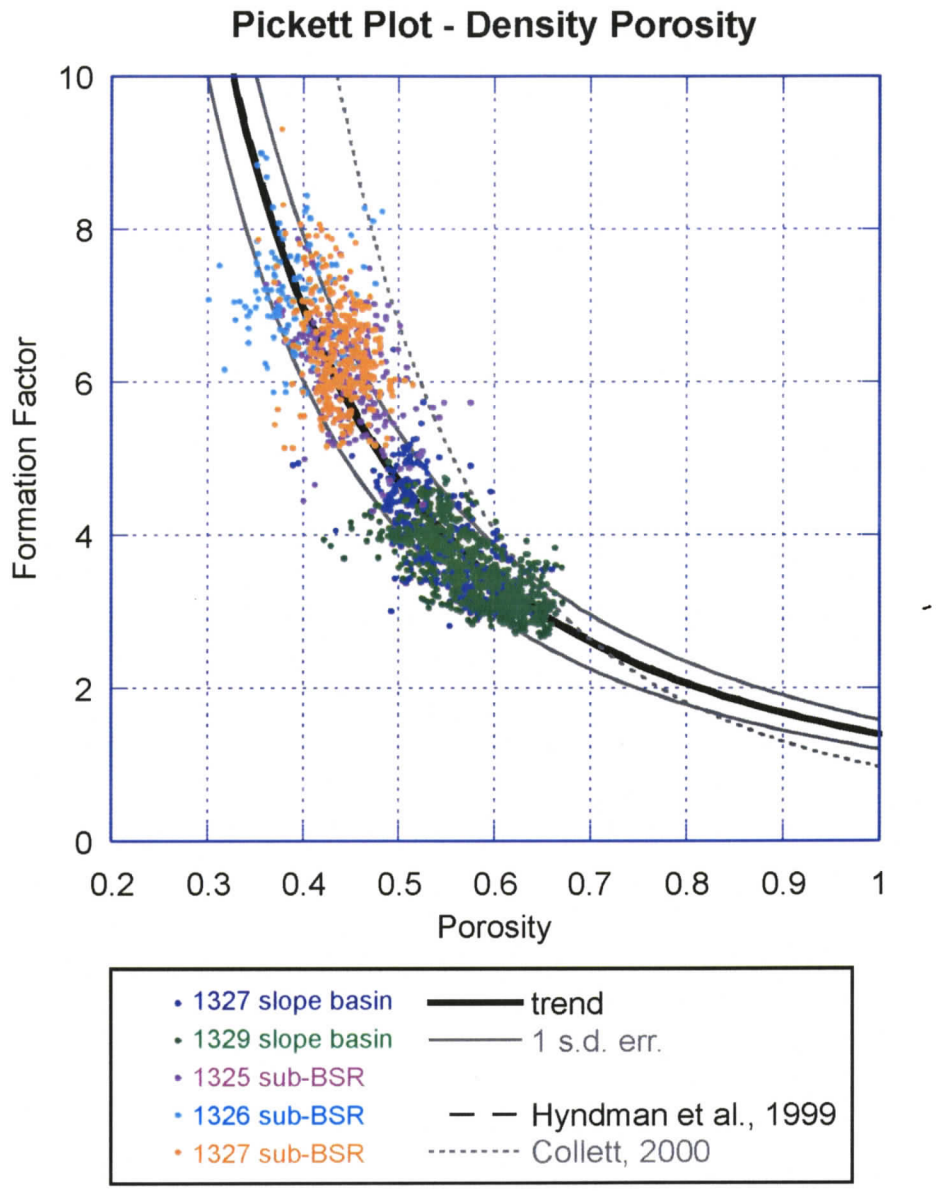

Figure 3.7 Formation factor versus density porosity for no-hydrate intervals of the IODP Expedition 311 well transect. The data points are taken from no-hydrate slope basin sediments and sub-BSR zones. The bold solid line is the best fit, giving $a = 1.38$ and $m = 1.76$. The uncertainty in a is ± 0.18, shown by the grey lines. For comparison, Hyndman et al. (1999) and Collett (2000) calculated Archie parameters of $a = 1.41$, $m = 1.76$, and $a = 0.97$, $m = 2.81$. The Hyndman et al. (1999) trend lies almost directly along the trend for these data.

searching for the best a gives a better fit for these data. The uncertainty in the Archie relation, arises mainly from the uncertainty in the Archie coefficient a; this uncertainty reflects the effect of data noise on the correlation between the porosity and resistivity measurements. Here, this includes random scatter (measurement error) in both the density and resistivity logs, as well as error related to the average grain density in the porosity calculation (Equation 3.1). An estimate of $n = 1.94$, calculated by Pearson et al. (1983) is used here for the Archie saturation exponent. A sensitivity analysis of the saturation exponent shows that varying n by ± 0.20 changes the gas hydrate saturation estimate by only ± 0.01, on average. However, inspection of Equation 2.5 or 2.6 shows that gas hydrate saturation estimates themselves are more sensitive to n at higher gas hydrate saturations. From a physical perspective, choosing a value for n similar to that of m implies the assumption that the effect of gas hydrate formation on the electrical resistivity is similar to that of simple effective porosity reduction.

3.3 Gas Hydrate Saturation from Resistivity

With estimated empirical Archie parameters a, m, and n, Equation 2.6 can be solved for S_h. The critical unknown parameter in Archie's relation is the in situ pore fluid resistivity R_w, which can be calculated from the equation of state of seawater (Fofonoff, 1985), if the in situ pore water salinity is known, assuming that the pore fluid composition is similar to that of seawater. In gas hydrate-free zones, the in situ salinity can be taken as the measured core salinity. However, if gas hydrate was initially present in the core, it would have dissociated upon recovery, thereby freshening the pore water and contaminating the in situ salinity (Kastner et al., 1995; Hesse, 2003), which is the key parameter in determining R_w. A lower estimated in situ salinity would result in a higher

R_w, which in turn would erroneously reduce gas hydrate saturation estimates. The main difficulty is in estimating the in situ salinity, before gas hydrate dissociation upon core recovery. In this thesis, two methods are proposed to solve this problem.

3.3.1 Core Baseline Salinity Method

A first solution is to assume a reference no-hydrate salinity profile at each site, corresponding to the highest salinity measurements smoothed over depth (Figure 3.6). This trend is referred to as the core baseline salinity C_{cb}. In this case, lower-than-baseline core salinity measurements are assumed to be due to freshening by gas hydrate dissociation upon core recovery, and C_{cb} is used in the calculation of R_w from the equation of state of seawater (Fofonoff, 1985). This approach assumes that there is no pervasive gas hydrate present in the pore space, only local concentrations such as in sandier horizons; i.e., core salinity measurements can sample pore fluid that has not been freshened by gas hydrate dissociation.

Once R_w has been calculated from C_{cb}, a qualitative approach to identify gas hydrate zones is to compare the measured resistivity R_t to the resistivity R_o that would have been measured if the sediment were fully water saturated (Figure 3.8). R_o is calculated from Equation 2.5, solved for $S_h = 0$. In Figure 3.8, zones above the BSR with $R_t > R_o$ are interpreted to contain gas hydrate. To obtain quantitative estimates of gas hydrate saturation, S_h is calculated from Equation 2.6 (Figure 3.9), with upper and lower bounds on S_h determined from the primary uncertainty associated with the estimated Archie coefficient a. In Figure 3.9, these results are smoothed by taking a running average over a 10 m interval. The uncertainty in the Archie coefficient a accounts for an average estimated uncertainty in S_h of $\pm$ 0.07 (one-standard-deviation).

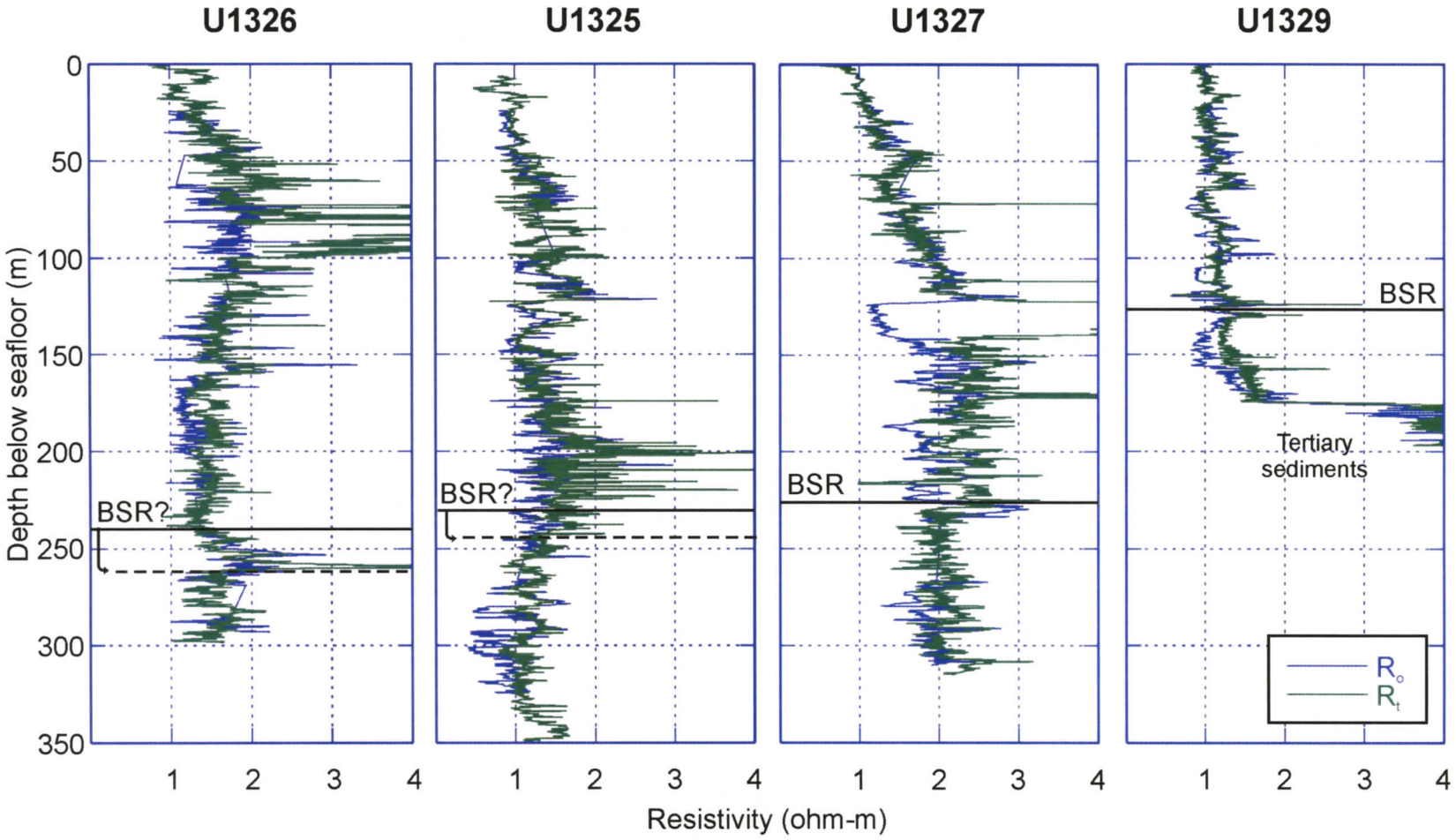

Figure 3.8 Measured LWD resistivity R_t, and 100% water-saturated resistivity R_o, determined from the Archie analysis of downhole data from IODP Expedition 311, at the four sites of the well transect. R_o is calculated from the log density porosity and the core baseline salinity.

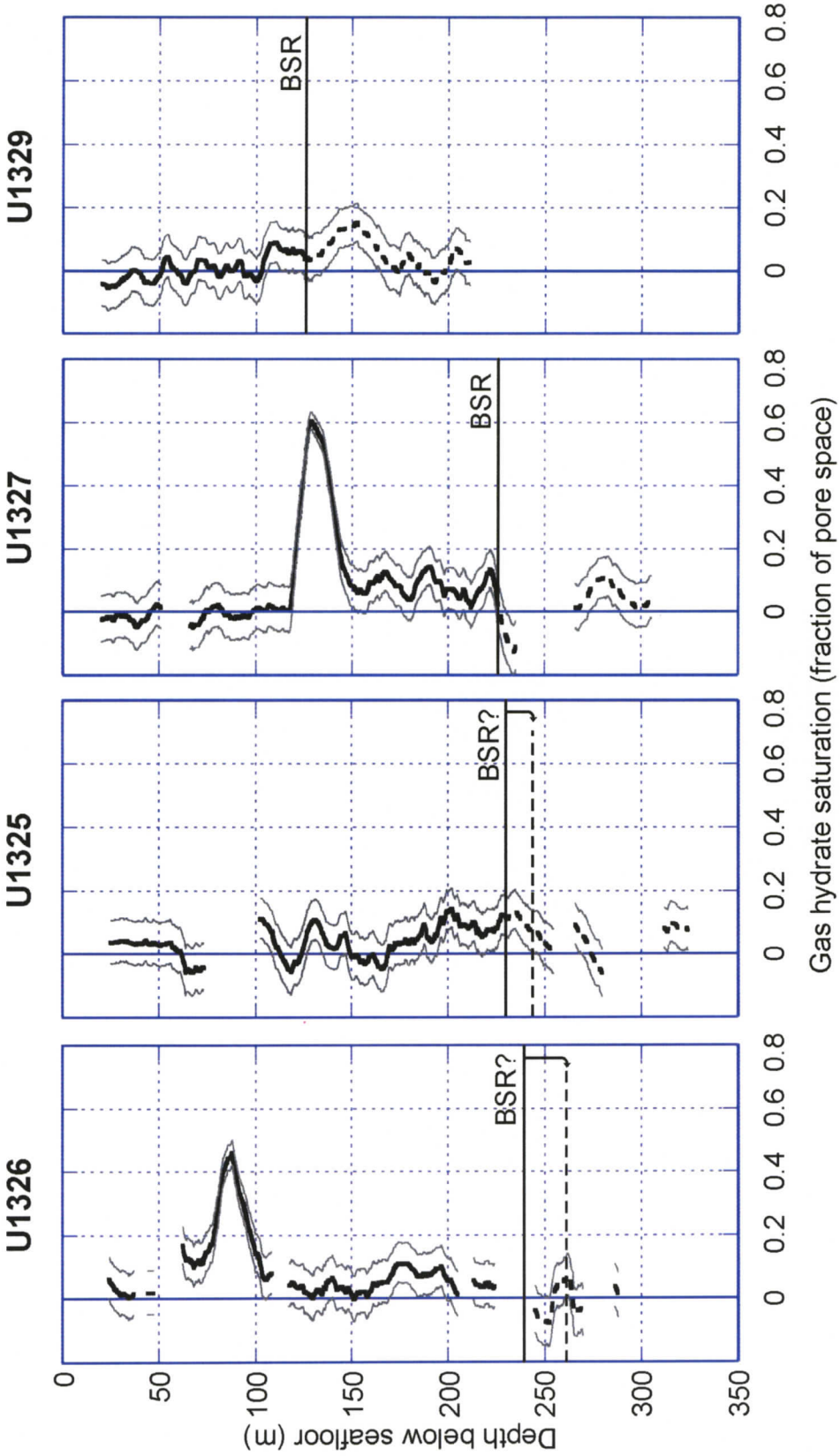

Figure 3.9 Gas hydrate saturation estimates for the sites of the IODP Expedition 311 well transect, calculated using the log density porosity, and the core baseline salinity method. The light grey lines indicate the one-standard-deviation error, from the uncertainty in Archie parameter estimation.

The important systematic uncertainty in this method is related to the implicit assumption that C_{cb} is an accurate estimate of the in situ salinity. At most sites, this assumption is probably valid, since the core baseline salinity is near that of seawater (Figure 3.6), i.e., assuming that a gas-hydrate-free core sample gives near-seawater salinity is generally reasonable. However, the core salinity measurements at Site U1327 exhibit an anomalous freshened baseline salinity trend, relative to the other sites (and nearby cold vent Site U1328, see Riedel et al., 2006). At U1327, the pervasive freshening can either be attributed to gas hydrate dissociation upon core recovery or some other source of fresh water, for example, clay dehydration from deep within the accrētionary prism. The core baseline salinity method attributes the regional freshening at U1327 (from seawater to baseline salinity) to sources other than gas hydrate dissociation. If all or most core samples were in fact freshened by pervasive gas hydrate, this regional gas hydrate would go undetected if the core baseline salinity method is used.

3.3.2 In Situ Salinity Method

An alternative approach that makes no assumptions about in situ salinity is that of Hyndman et al. (1999). With additional assumptions, both gas hydrate saturation and in situ salinity can be estimated: they solve Archie's equation (Equation 2.6) for S_h, simultaneously with

$$R_w = R_{sw}\left(\frac{C_{sw}}{C_w}\right), \tag{3.2}$$

and

$$1 - S_h = \frac{C_{core}}{C_w}. \tag{3.3}$$

where R_{sw} is the resistivity of seawater (dependent on pressure and temperature, but with fixed seawater salinity concentration C_{sw} taken to be 35), C_{core} is the core fluid salinity concentration (after dissociation of any in situ gas hydrate), and C_w, the in situ fluid salinity, which is unknown. The physical basis for Equation 3.3 is the salinity dilution due to gas hydrate dissociation upon core recovery. Hyndman et al. (1999) assumed the simplification $n = m$; their equation is modified here to allow for different values of n and m (Riedel et al., 2005):

$$S_h = 1 - \left(\frac{a C_{sw} R_{sw}}{\varphi^m C_{core} R_t} \right)^{1/(n-1)}, \qquad (3.4)$$

where R_t is the measured resistivity. For exactness, this calculation requires C_{core} to be measured from the same physical sample in which the resistivity was measured. However, the resistivity data is from nearby downlole logs (from a different hole, at the same site). The best approximation available is to take C_{core} as the core baseline salinity trend C_{cb} (this is somewhat different from the approach of Hyndman et al. (1999), discussed in Section 3.6). This yields the gas hydrate saturation profiles shown in Figure 3.10, averaged vertically, over a 10 m window. The in situ salinity method gives systematically higher gas hydrate saturation estimates than the core baseline salinity method. To understand the reason for the bias, the in situ salinity method is examined in more detail.

Having solved for S_h in Equation 3.4, Equation 3.3 provides a means to calculate the in situ salinity C_w, which can then be compared to C_{cb} to determine if there is regional salinity dilution, in the recovered core, due to pervasive gas hydrate occurrence, i.e., to determine whether or not the core baseline salinity trend is a good estimate of the in situ

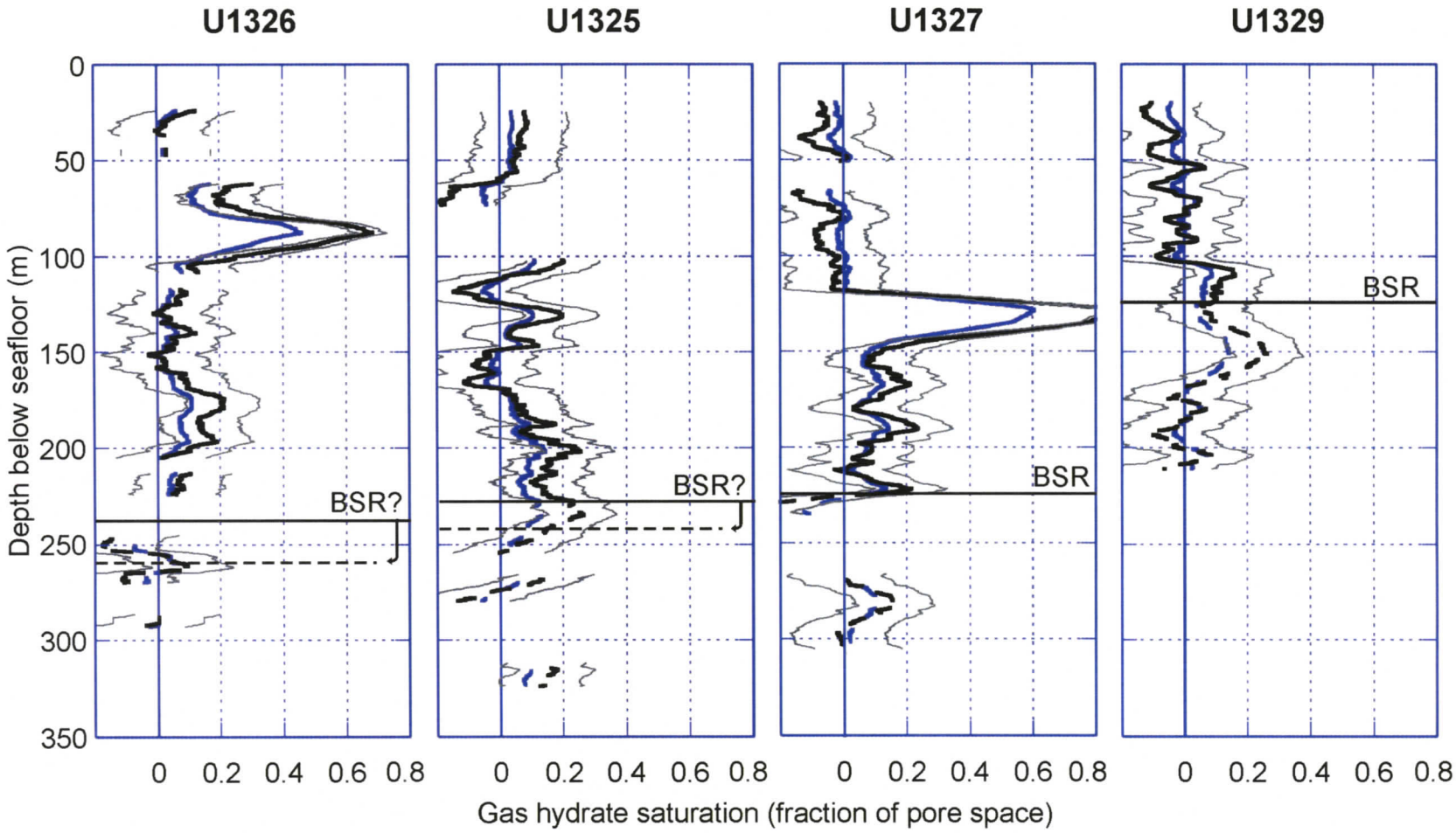

Figure 3.10 Gas hydrate saturation estimates (thick black line) calculated using the log density porosity, and the in situ salinity method. The light grey lines indicate the one-standard-deviation error, from the uncertainty in Archie parameter estimation, and the blue line is the saturation estimate from the core baseline salinity method.

salinity (Figure 3.11). It is first observed that in areas with high gas hydrate saturation, C_w calculated by the in situ salinity method, is much higher than C_{cb}, and even reaches unreasonable amounts in some places. This occurs because C_{core} is taken in Equation 3.4 to be the core baseline salinity trend C_{cb}, whereas, in reality, core salinity measurements C_{core} in these anomalous regions actually show fresher pore waters that do not lie on the background trend (Figure 3.11, e.g., U1327, 120-138 m below the seafloor (mbsf)). In other words, if the gas hydrate saturation was calculated at the depth of a freshened core sample, using the actual measured core salinity, rather than the higher core baseline salinity trend, by Equation 3.3, S_h and C_w would be less. The end result is an overestimation of S_h in areas with higher-than-background gas hydrate saturation, as observed in Figure 3.10. The method of Hyndman et al. (1999) is limited in areas with heterogeneous gas hydrate distributions, because it requires the actual core salinity measurement C_{core} from the same sediment in which the resistivity was measured. However, it does provide a basis for the estimation of an in situ baseline salinity trend C_{wb}: in areas with background levels of gas hydrate saturation S_h (whether or not they are zero), measurements of C_{core} lie on the core baseline salinity trend C_{cb}, and the approach provides an accurate estimate of both S_h and C_w, because C_{cb}, in this case, is approximately equal to the measured C_{core}. So, although the overall S_h and C_w profiles calculated from the in situ baseline approach have inaccurate zones, their baseline trends C_{wb} are representative of the true in situ salinity. The in situ baseline salinity trend C_{wb} can therefore be compared to the core baseline salinity trend C_{cb} to determine if there is regional core freshening from gas hydrate dissociation. At Sites U1325, U1326, and U1329, C_{wb} is well estimated by C_{cb}, to within the uncertainty of the Archie parameters

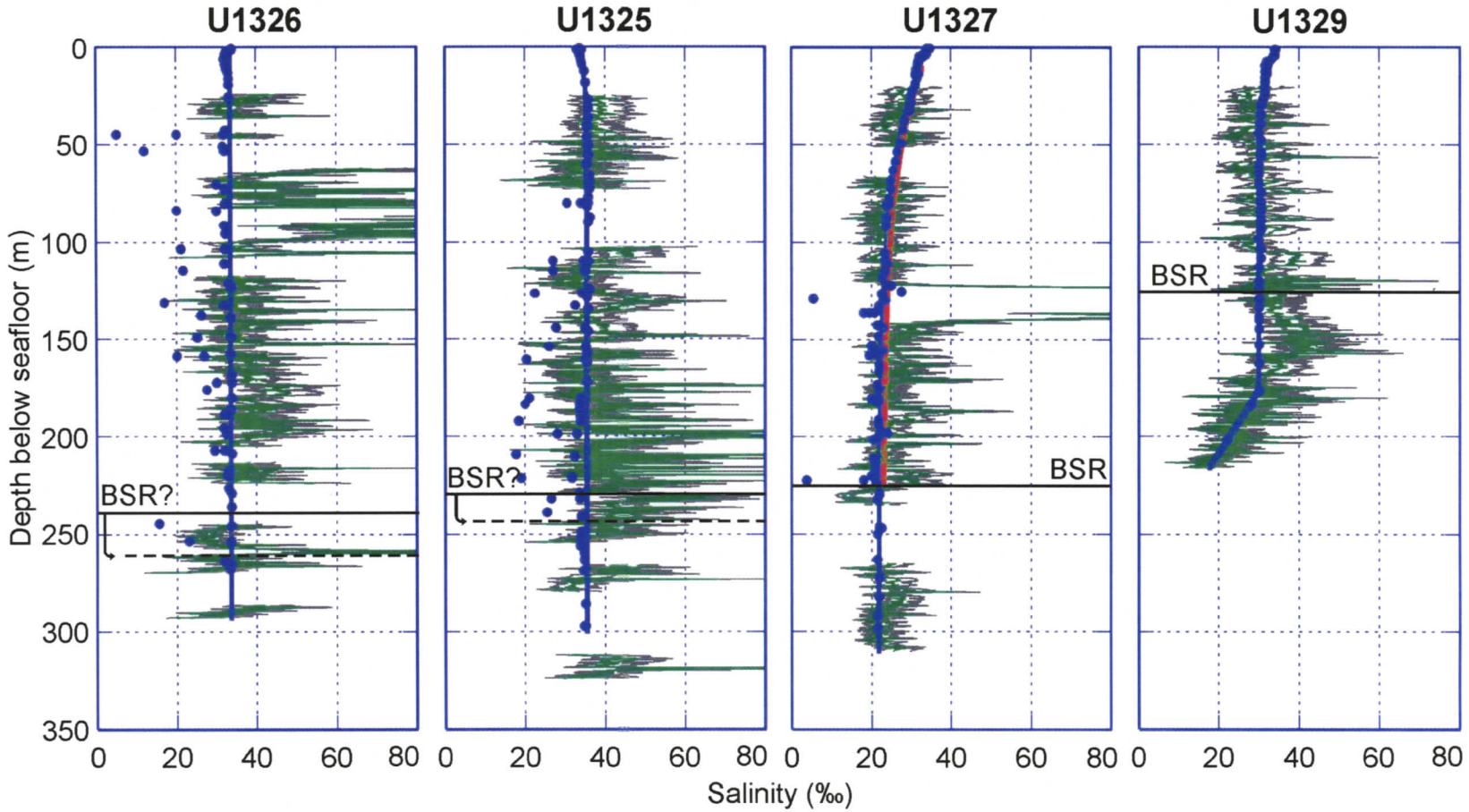

Figure 3.11 In situ pore water salinity concentration C_w calculated from the in situ salinity method, based on the log density porosity. The calculated in situ salinity is in green, with one-standard-deviation uncertainties in grey. The blue dots are core salinity measurements. The blue line is the core baseline salinity trend C_{cb}, and the red line at U1327 is the re-estimated in situ baseline salinity trend C_{wb}. At the other sites, C_{cb} is a good estimate of C_{wb}.

(Figure 3.11); i.e., taking C_{cb} as the in situ salinity is a good approximation at these sites. At U1327, C_{wb} is estimated to be slightly higher than C_{cb}, indicating a small amount of regional freshening from dissociation upon core recovery. At U1327, the gas hydrate saturation is therefore recalculated from the core baseline salinity method, but by using C_{wb} (a better estimate of in situ salinity) instead of C_{wb} (Figure 3.12). This gives slightly higher S_h estimates.

3.3.3 Procedure for Estimation of Gas Hydrate Saturation

Used together, the core baseline salinity method and the in situ salinity method provide a means to estimate gas hydrate saturation that uses justifiable assumptions about the in situ salinity. The flow chart in Figure 3.13 summarizes the proposed procedure, outlined below.

First, a salinity profile C_w should be calculated from the in situ salinity method, and plotted with the core baseline salinity trend (estimated from the core salinity measurements). If the core baseline salinity trend C_{cb} is a good estimate of the in situ baseline salinity trend C_{wb} (estimated as the baseline of the C_w profile), then the core baseline salinity method should be used to estimate gas hydrate saturation. If C_{cb} is not a good estimate of C_{wb}, then the core salinity baseline method should still be used to estimate gas hydrate saturation, but C_{wb} should be used instead of C_{cb} to calculate the pore fluid resistivity R_w.

In essence, the core baseline salinity method is accurate in estimating gas hydrate saturation if the in situ salinity used in the calculation is correct, and the in situ salinity method provides a means to estimate the true in situ salinity.

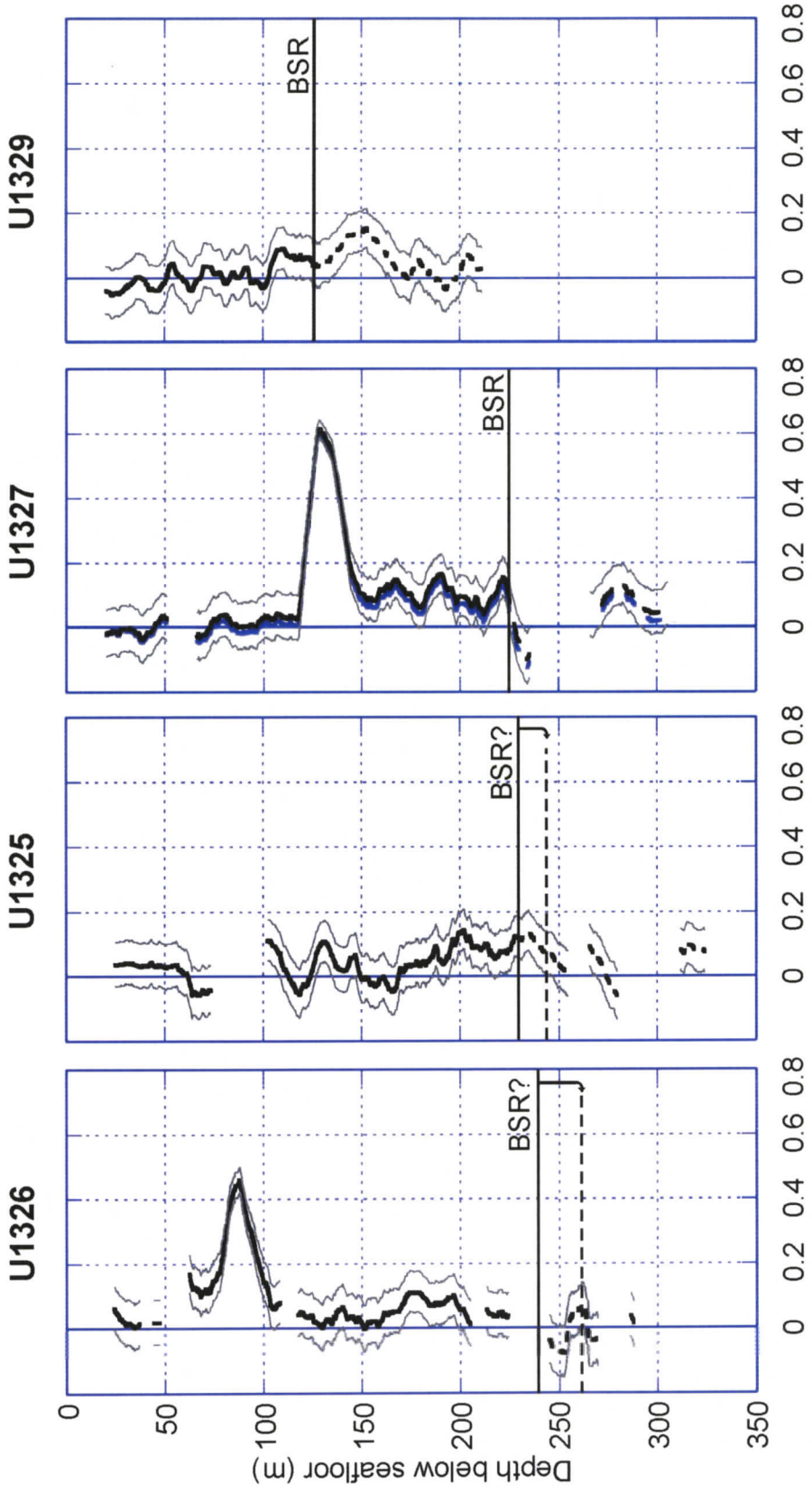

Figure 3.12 Gas hydrate saturation estimates (thick black line) calculated using the log density porosity, and the baseline salinity method (with a new baseline salinity profile for U1327). The light grey lines indicate the one-standard-deviation error, from the uncertainty in Archie parameter estimation. The blue line at U1327 is the estimate from the core baseline salinity.

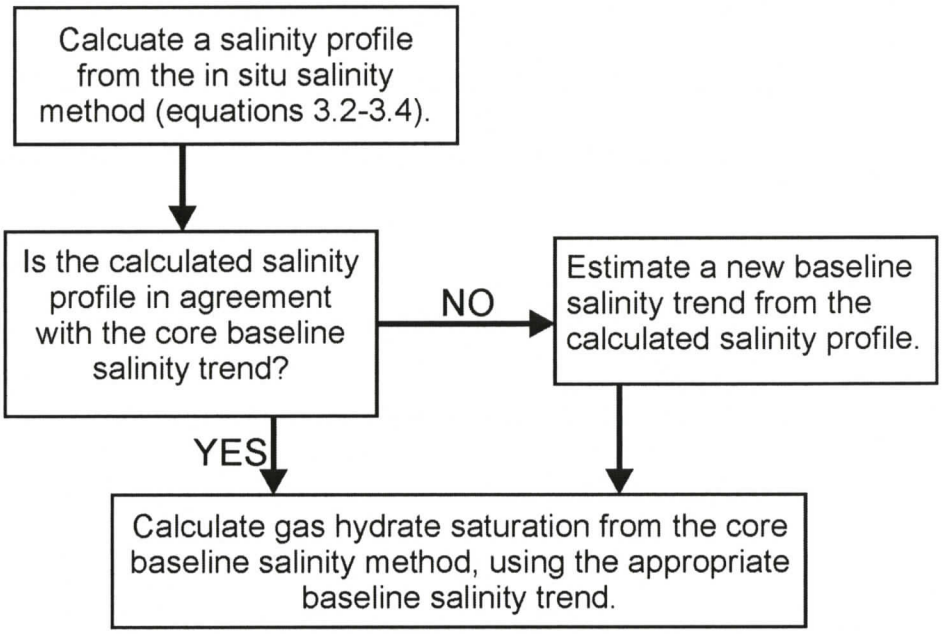

Figure 3.13 Flow chart for determination of gas hydrate saturation from Archie analysis of downhole resistivity data. This approach accounts for uncertainties in Archie parameters and uncertainties in the in situ salinity.

3.4 Uncertainty in Porosity

So far, gas hydrate saturation has been calculated by using the porosity determined from the LWD density log. The methods described in Sections 3.2-3.3 are applied here to neutron porosity and core porosity measurements, in order to determine the sensitivity of S_h estimates to the type of porosity measurement.

3.4.1 Neutron Porosity

New Archie parameters are calculated for the resistivity vs. neutron porosity relation from a cross plot of these measurements in gas hydrate-free zones (Figure 3.14), giving $a = 1.74 \pm 0.32$, for m fixed at 1.76. This unusually high value for a further suggests that the neutron porosity log values have a positive bias about the true porosity

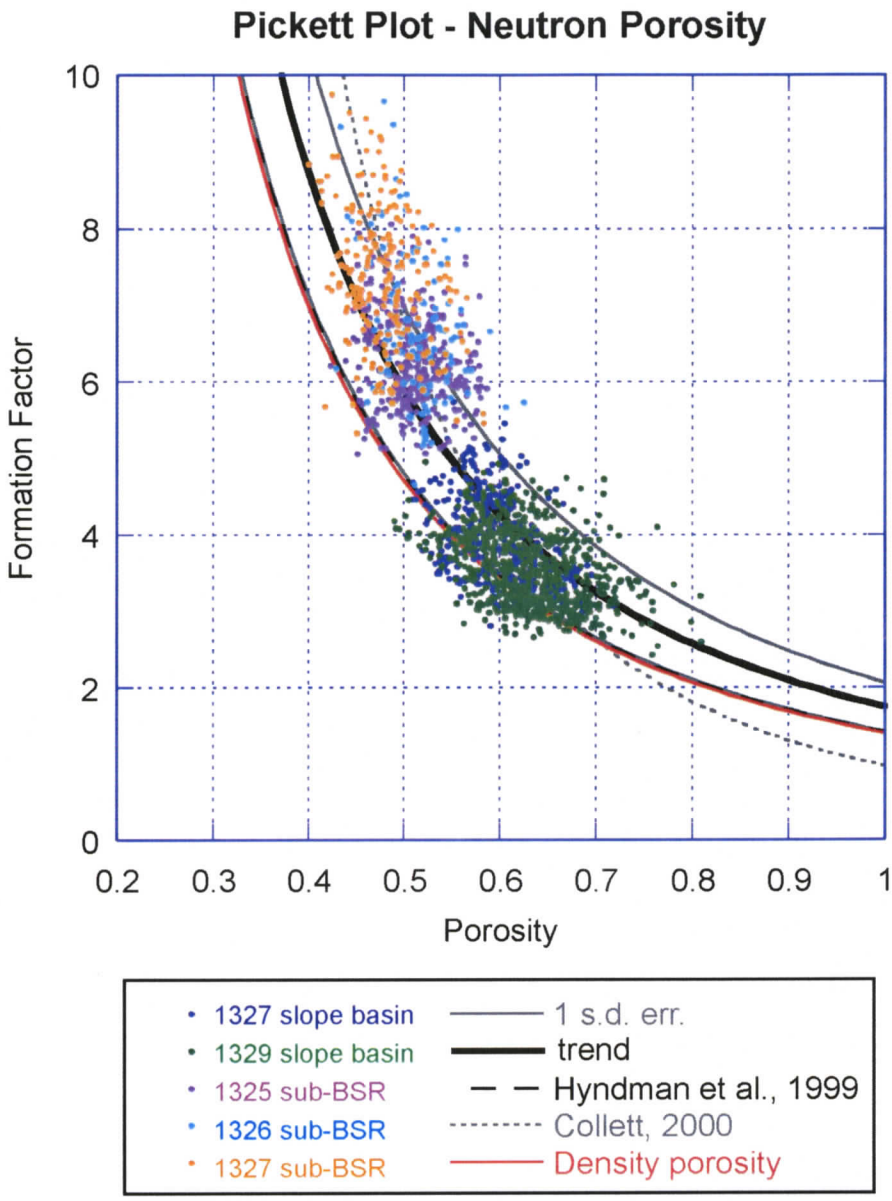

Figure 3.14 Formation factor versus neutron porosity for no-hydrate intervals of the IODP Expedition 311 well transect. The data points are taken from no-hydrate slope basin sediments and sub-BSR zones. The bold solid line is the best fit, giving $a = 1.74$ and $m = 1.76$. The uncertainty in a is ± 0.32, shown by the grey lines. For comparison, Hyndman et al. (1999), and Collett (2000) calculated Archie parameters of $a = 1.41$, $m = 1.76$, and $a = 0.97$, $m = 2.81$. The best fit using the density porosity gave $a = 1.39$, $m = 1.76$.

(possibly related to an incomplete correction for bound water content). Furthermore, the sub-BSR zones used in the Archie parameter estimation could potentially have anomalously high porosity values, due to the influence of free gas below the BSR on the hydrogen concentration. These zones are kept in the analysis because they significantly add to the range of porosities sampled in the empirical calibration.

Following the protocol outlined in Section 3.3.3, in situ salinity profiles C_w are calculated from the in situ salinity method at the four sites (Figure 3.15). At Sites U1325, U1326, and U1329, the core baseline salinity C_{cb} is interpreted to be a good estimate of the true in situ salinity, so the core baseline salinity method is used at these sites to calculate gas hydrate saturation (Figure 3.16). At U1327, C_{wb} is again estimated to be slightly higher than C_{cb}, therefore C_{wb} (the better estimate of in situ salinity) is used to calculate S_h from the core baseline salinity method. The uncertainty in a accounts for an average uncertainty in S_h of ± 0.09. Neutron porosity-based calculations of S_h generally agree with those obtained from the density porosity, to within the calculated uncertainty, because the bias in porosity is accommodated by the porosity-specific Archie parameters. This highlights the importance of using empirical Archie parameters calibrated to the specific type of measurement made.

As a check, the Archie analysis is repeated for the neutron porosity, using a neutron porosity profile that is shifted, so that its mean at each site is equal to the mean density porosity at that site. This approach eliminates some of the biases inherent in the neutron porosity measurement, while preserving structure in the log that might not be present in the density porosity profile. This test gives gas hydrate saturation profiles at all sites that are in agreement with both the density porosity-based estimates and the

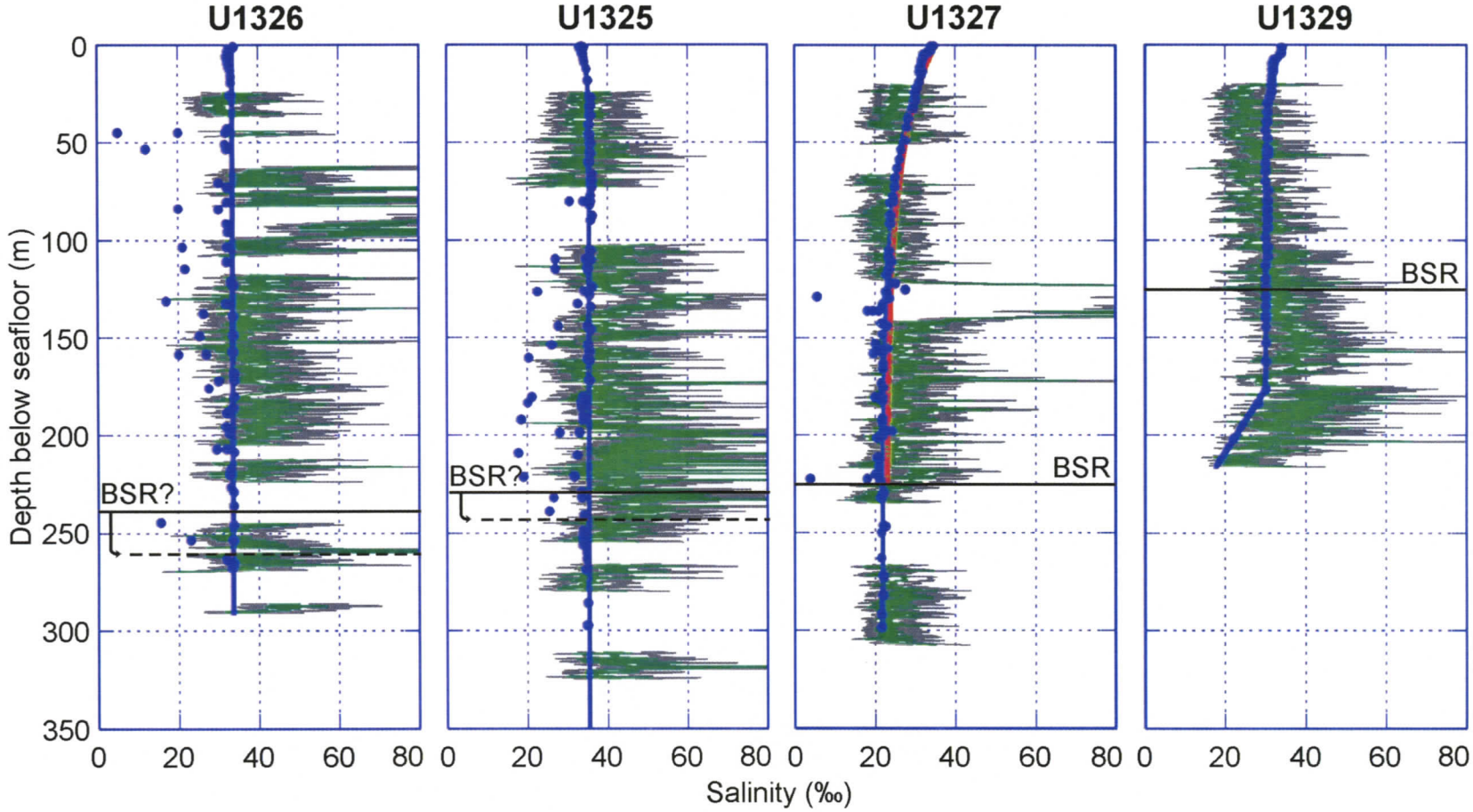

Figure 3.15 In situ pore water salinity concentration C_w calculated from the in situ salinity method, based on the log neutron porosity. The calculated C_w is in green, with one-standard-deviation uncertainties in grey. The blue dots are core salinity measurements. The blue line is the core baseline salinity trend C_{cb}, and the red line at U1327 is the re-estimated in situ baseline salinity trend C_{wb}. At the other Sites, C_{cb} is a good estimate of C_{wb}.

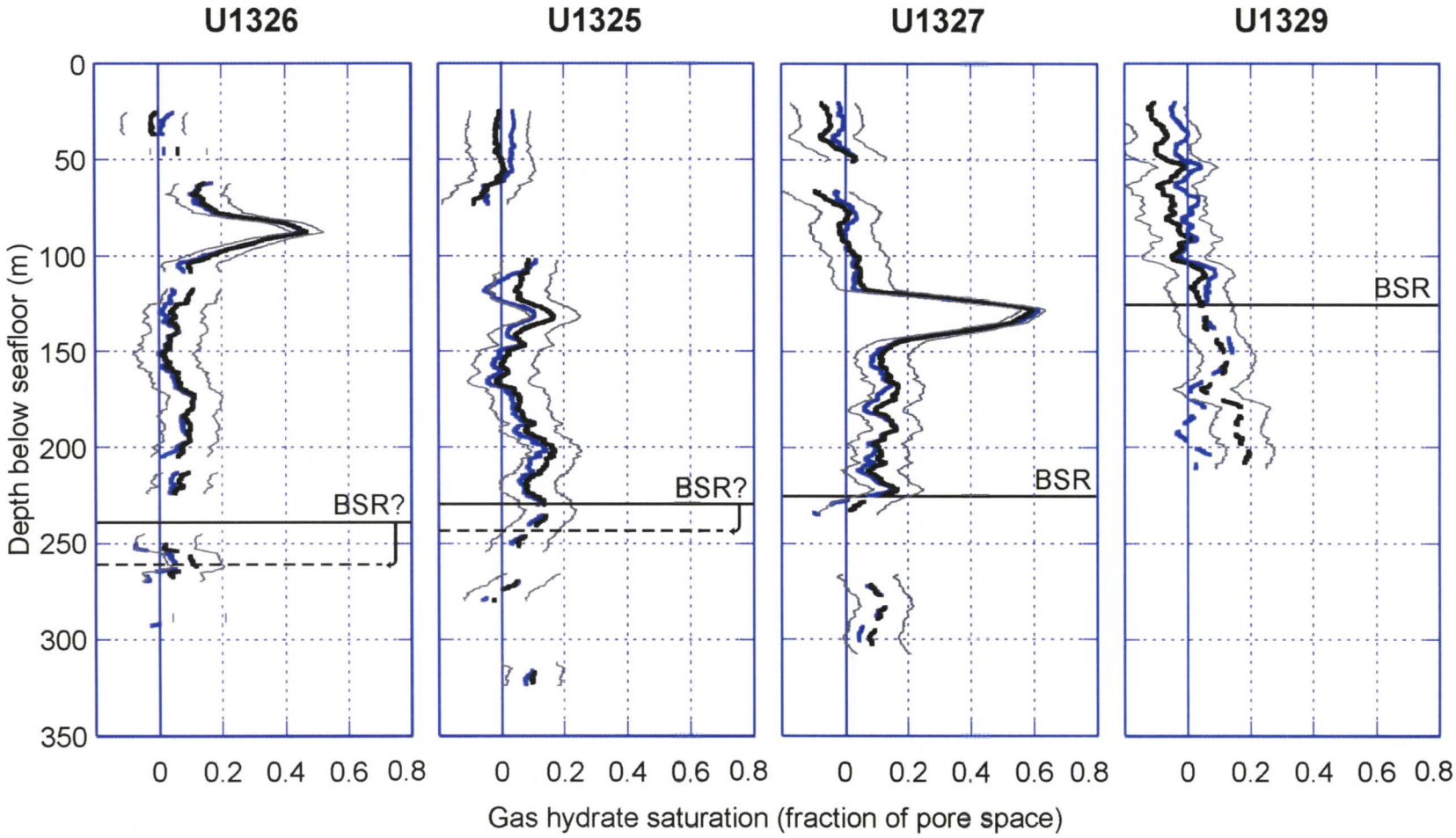

Figure 3.16 Gas hydrate saturation estimates (thick black line) calculated using the log neutron porosity, and the baseline salinity method (with a new baseline salinity profile for U1327). The light grey lines indicate the one-standard-deviation error, from the uncertainty in Archie parameter estimation, and the blue line is the density porosity based estimates.

previous estimate from the (non-shifted) neutron porosity, to within the uncertainties estimated from the Archie parameters.

The general conclusion from the neutron porosity analysis is that it yields gas hydrate saturation estimates that are similar to those obtained from the density porosity analysis, but with larger uncertainties. Gas hydrate saturation estimates using neutron porosity are not particularly sensitive to the bias towards higher porosities present in the neutron log, so long as the Archie parameters are also calibrated to those biased porosity measurements.

3.4.2 Core Porosity

To determine the Archie parameters for the log resistivity versus core porosity data, an average log resistivity value for the one meter interval corresponding to the core sample depth was calculated for each core sample in gas hydrate-free zones. The spatial correspondence is only approximate, since the core and log data are from different holes, ~50 m apart. The resistivity versus porosity data are shown in a Pickett plot (Figure 3.17). With m fixed to 1.76, the best fit to a is 1.43 ± 0.27, a value close to that obtained using the density porosity. Note that the statistical uncertainty in a is greater than for the log density porosity based relation, probably mainly reflecting the fact that the resistivity and core porosity are measured in different holes.

The log resistivity data and core porosity trend are used to calculate S_h, following the procedure outlined in Section 3.3.3. Because core porosity measurements are not available at each log sample, a core porosity trend is calculated at each site (Figure 3.5), as a smoothed profile (a least-squares fit) through the core porosity data, using Athy's law, emulating compaction and porosity loss with depth (Athy, 1930):

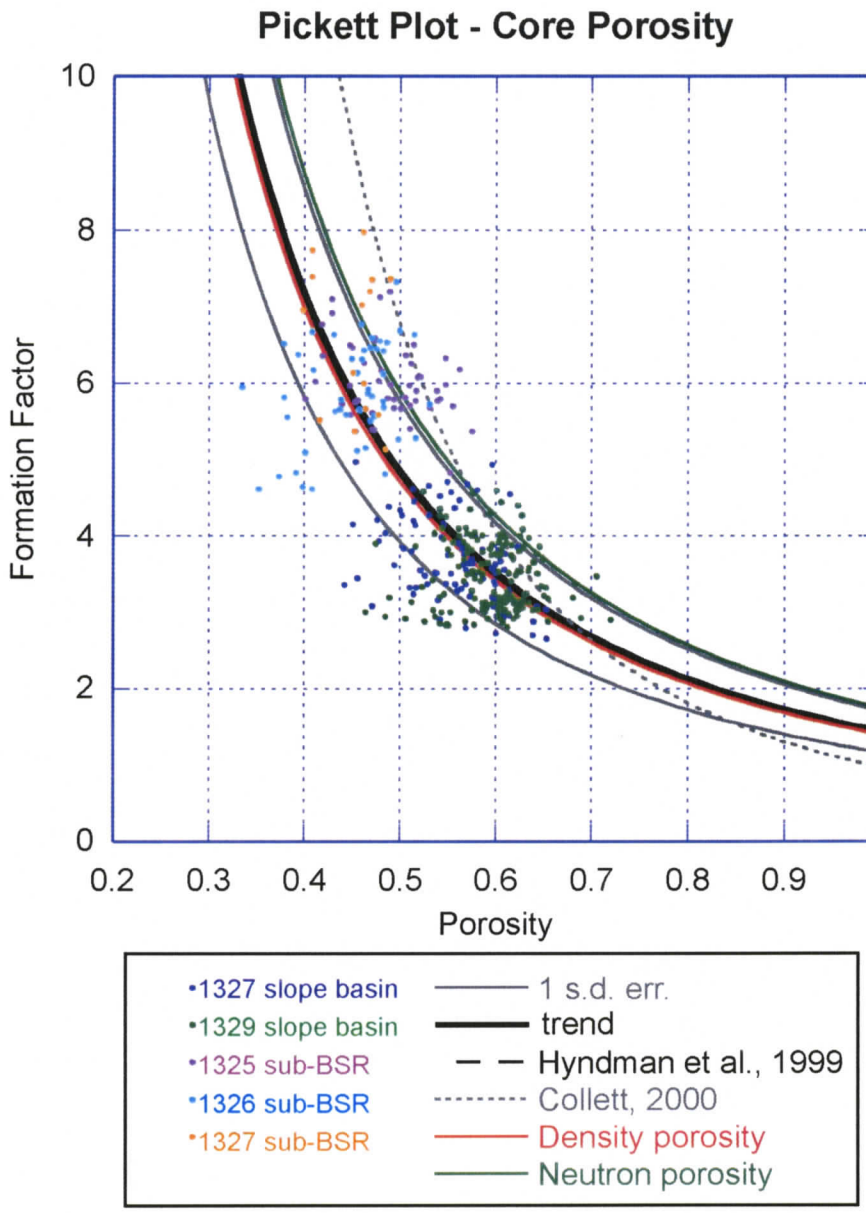

Figure 3.17 Formation factor versus core porosity for no-hydrate intervals of the IODP Expedition 311 well transect. The data points are taken from no-hydrate slope basin sediments and the sub-BSR zones. The bold solid line is the best fit, giving $a = 1.43$ and $m = 1.76$. The uncertainty in a is ± 0.27, shown by the grey lines. For comparison, Hyndman et al. (1999), and Collett (2000) calculated Archie parameters of $a = 1.41$, m = 1.76, and $a = 0.97$, $m = 2.81$. The best fit using the density and neutron porosity gave $a = 1.39$, $m = 1.76$, and $a = 1.74$, $m = 1.76$, respectively. The Hyndman et al. (1999) trend lies almost directly along the trend for these data.

$$\varphi(z) = \varphi_o e^{-z/L}, \tag{3.5}$$

where z is the depth below seafloor, φ_0 is the porosity at the seafloor, and L is a characteristic decay constant. Equation 3.3 is then used to calculate the in situ salinity profile C_w, from which the in situ baseline salinity trend C_{wb} is estimated. C_{wb} is compared to the core baseline salinity trend C_{cb}, to assess whether or not C_{cb} is a good estimate of the true in situ salinity (Figure 3.18). C_{wb} profiles calculated for Sites U1326 and U1327 give trends with slightly greater in situ salinity than C_{cb}. The gas hydrate saturation S_h is then calculated from the core baseline salinity method, using C_{wb} at Sites U1326 and U1327 and C_{cb} at Sites U1325 and U1329 (Figure 3.19). Uncertainties in Archie parameters account for an average uncertainty in S_h of ± 0.08.

Gas hydrate saturation calculated from core porosity and log density porosity are generally in good agreement, since S_h profiles calculated from these two porosity measurements have uncertainty bounds that overlap in most areas (Figure 3.19). One exception is at Site U1327, where S_h calculated from the core porosity is on average 0.09 greater in the interval of accreted sediments above the BSR (90-225 mbsf). The difference at this site occurs because the porosity profile observed in the log is not well represented by the smoothed Athy-type porosity-depth relation applied to the core data. While there is no significant overall bias between the log density porosity and the core porosity trend, there are local biases at certain depths (Figure 3.5): in the accreted section above the BSR (90-225 mbsf), with the exception of the high porosity unit at 120-138 mbsf, the log density porosity is almost exclusively lower than the core porosity trend. Since the Archie parameters (calculated for an average porosity-resistivity relation) are

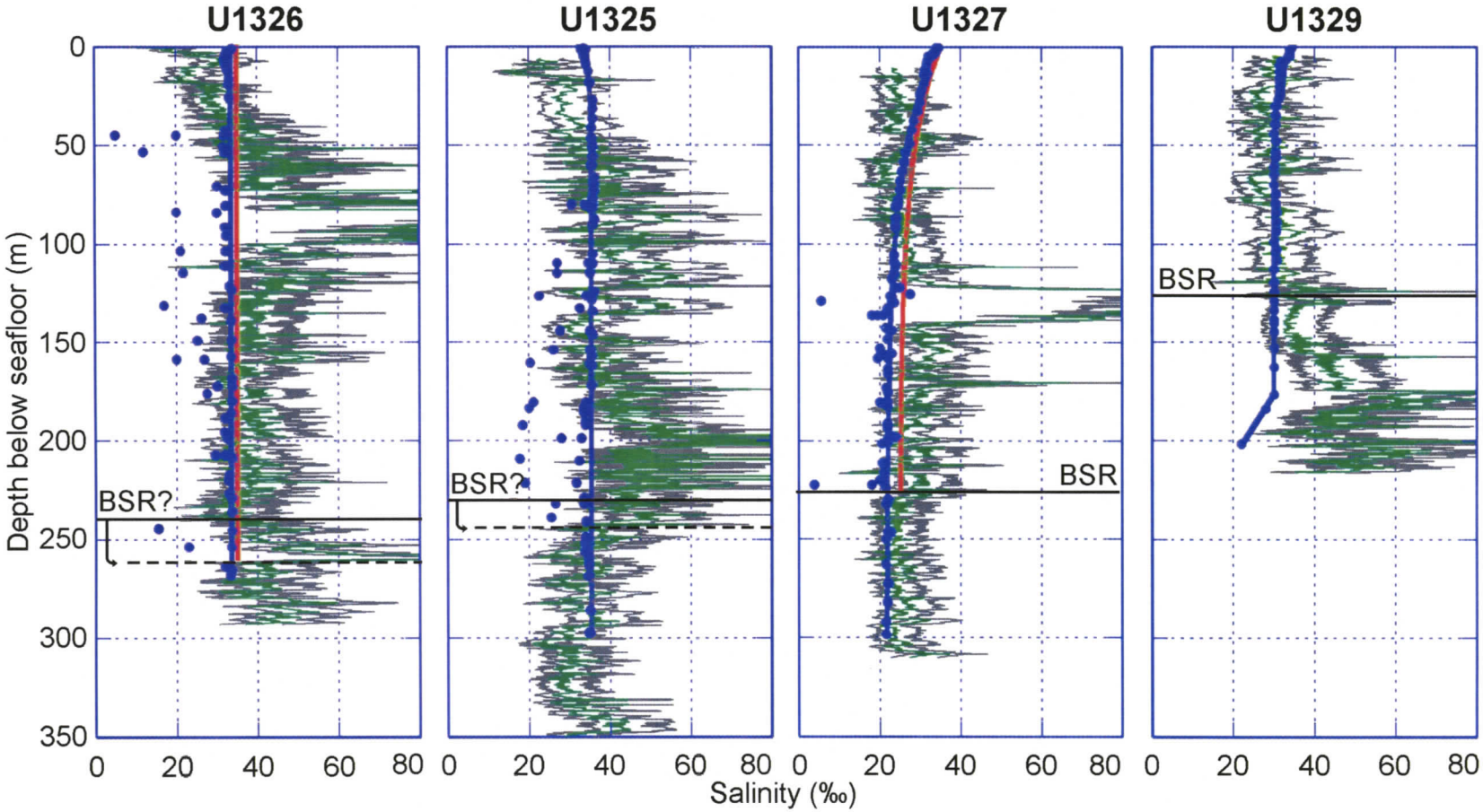

Figure 3.18 In situ pore water salinity concentration C_w calculated from the in situ salinity method, based on core porosities. The calculated C_w is in green, with one-standard-deviation uncertainties in grey. The blue dots are core salinity measurements. The blue and red lines are the core baseline salinity trend C_{cb} and the re-estimated in situ baseline salinity trend C_{wb}. At U1325 and U1329, C_{cb} is a good estimate of C_{wb}.

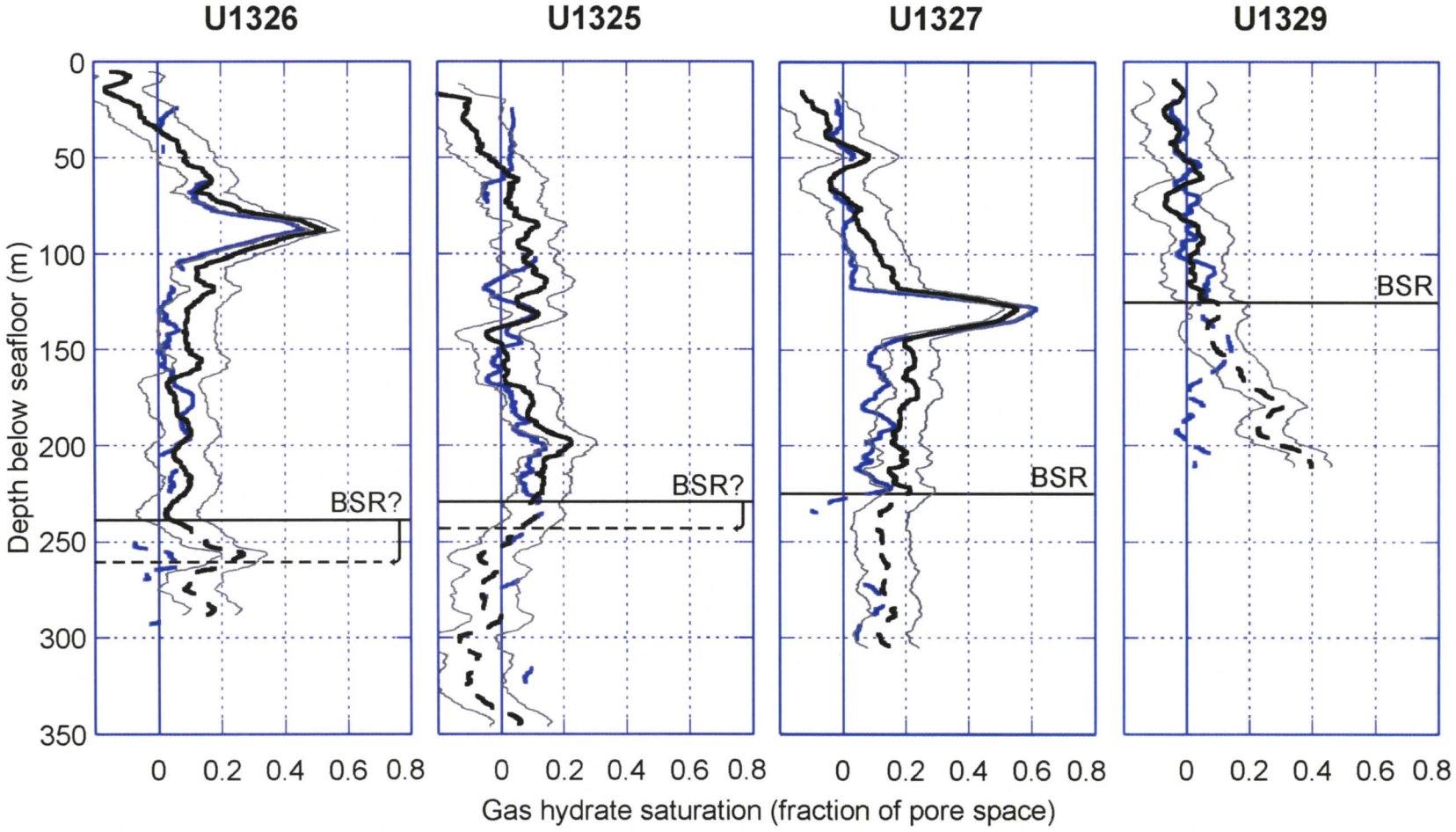

Figure 3.19 Gas hydrate saturation estimates (thick black line) calculated using the core porosity trend, and the baseline salinity method (with new baseline salinity profiles for U1326 and U1327). The light grey lines indicate the one-standard-deviation error, from the uncertainty in Archie parameter estimation, and the blue line is the density porosity based estimates.

similar for the core and log density porosity, S_h and C_w are biased towards higher values in this interval, because of the local porosity bias.

Although the results from the core porosity analysis are reasonable, gas hydrate saturation estimates based on log density porosity measurements are preferred, for the following reasons. Core porosities are disadvantaged, because (1) they need to use a trend that is smoothed over depth to match the sampling of the resistivity log, (2) they have been measured in samples from different holes than the resistivity data, leading to additional uncertainty caused by inter-hole variability, and (3) because the porosity is measured onboard the ship, after core recovery, rather than in situ.

The log density porosities have the disadvantage that the porosity is not measured directly. Porosity is estimated from log density, assuming first that the formation bulk density is well related to the measured electron density, and second that the average grain density used in an adequate approximation.

3.5 Summary

The goal of the resistivity study was to estimate gas hydrate saturation from the electrical logs and porosity estimators, using Archie analysis, while rigorously addressing uncertainties in (1) Archie parameters, (2) in situ salinity, and (3) in situ porosity. In the resistivity analysis, a method was developed to obtain (as accurate as possible) estimates of in situ salinity, and gas hydrate saturation estimates were reported with uncertainties related primarily to Archie parameter estimation. The analysis of the different available porosity measurements showed that a bias in porosity does not significantly affect the gas hydrate saturation estimate, so long as the Archie parameters have been properly estimated. The most reliable porosity measurement was concluded to be the log density

porosity, because it is well calibrated to the core porosities, and was measured in the same hole as was the resistivity. Uncertainties in the density porosity measurement arise mainly from the statistical uncertainty in the gamma-ray count used to calculate the density, and the error induced by using an average grain density in mapping bulk density to porosity. However, assuming that these sources of error produce random, unbiased, noise in the data, they are inherently included in the Archie parameter uncertainties, and have therefore been accounted for.

Considering the estimates from density porosity to be the most accurate, gas hydrate saturations averaged over a 10 m window (Figure 3.12) show distributed gas hydrate occurrence in many intervals (S_h ~0.09 ± 0.07 at U1326, 170-200 mbsf; S_h ~0.10 ± 0.07 at U1325, 190-230 mbsf; S_h ~0.11 ± 0.07 at U1327, 140-225 mbsf), with average concentrations of 5-15% of the pore space, over depth intervals of 20 to 100 m. However, despite the interpreted distributed gas hydrate occurrences, the general agreement between the salinity baselines C_{cb} and C_{wb} indicate that core salinity measurements can sample pore water that has not been freshened by gas hydrate dissociation upon core recovery. This finding suggests that on the scale of individual log or core measurements, it is possible to sample gas-hydrate-free zones, but at 10 m scale, gas hydrate occurrence is distributed. One possible exception is at Site U1327, where the estimated C_{wb} is slightly higher than C_{cb}, indicating a minor amount of regional freshening of core salinities from gas hydrate dissociation upon core recovery. C_{wb} is greater than C_{cb} by less than ~1.5‰ salinity units, corresponding to a background gas hydrate pore space saturation of less than 3%. Based on the estimate of C_{wb} at the BSR, the difference between the background freshening measured in core (~22‰ salinity) and the salinity of

seawater (35‰ salinity) is attributed mostly to regional freshening form deeper sources of fresh water (~90%), with the rest of the freshening (~10%) attributed to gas hydrate dissociation upon core recovery.

Additionally, intervals of very high gas hydrate saturation of over 40% of the pore space are observed at Sites U1326 (73-94 mbsf) and U1327 (120-138 mbsf). These were documented during IODP Expedition 311 (Riedel et al., 2006), and were interpreted to be high porosity sandy turbidite units, in which large amounts of gas hydrate has formed. The correlation between these coarser-grained turbidite units and high gas hydrate saturation is the principal observation supporting the hypothesis that gas hydrate occurrence is largely controlled by sediment grain size and associated formation parameters, such as permeability (Riedel et al., 2006).

3.6 Comparison with Previous Interpretation

The gas hydrate saturation estimates from this study at U1327 differ significantly from the previous downhole resistivity study at nearby ODP Site 889 of Hyndman et al. (1999). They estimated 25-30% gas hydrate pore space saturation in the 100 m interval above the BSR (compared to the 5-15% estimated in this study). This discrepancy is mainly attributed the porosity measurement used in the analysis, and the formulation of Archie's equation used to estimate gas hydrate saturation.

Hyndman et al. (1999) used a smoothed fit to core porosities in their analysis, whereas here, the best results are taken to be those obtained from the log density porosity. In this analysis, using a smoothed core porosity trend yielded 15-25% gas hydrate pore space saturation in the 100 m interval above the BSR at U1327. The difference is that in the 100 m above the BSR, the core porosity is (locally) biased relative to the log density

porosity (discussed in Section 3.4.2). Since the resistivity is the same, the porosity bias must, to first order, be compensated for by an equivalent volume of gas hydrate (since the Archie parameters are very similar), resulting in higher gas hydrate saturation estimates.

The second reason for the discrepancy is that Hyndman et al. (1999) estimated S_h directly from the in situ salinity method, whereas in this study, C_{wb} is estimated from the in situ salinity method and used as the salinity profile in the core baseline salinity method, to calculate S_h. As discussed in Section 3.3.2, the in situ salinity method, used on its own, overestimates S_h in areas where core salinities are freshened relative to C_{cb}. This occurs because the in situ salinity method is only truly accurate if the resistivity and core salinity are measured on the same physical sample. This difference accounts for a difference in S_h of 0-0.08 in the 100 m interval above the BSR.

Finally, a minor contribution to the difference in the results is that the simplification $n = m$ adopted in the Archie analysis of Hyndman et al. (1999) accounts for and increase in gas hydrate saturation of ~4% (Riedel et al., 2005). All these factors combined account for a difference of 14-22% gas hydrate saturation, which is approximately the difference between the reported estimates at U1327/889.

Gas hydrate saturation estimates from a field resistivity experiment (CSEM) near Site U1327 (Yuan and Edwards, 2000) indicate that gas hydrate saturation in this area are 17-26% of the pore space. This result is also moderately different from the concentrations reported in this study, at Site U1327.

Chapter 4

Gas Hydrate Concentration from Seismic Velocity

Seismic velocity information can be used to estimate gas hydrate concentration (e.g., Yuan et al., 1996; Helgerud, 2001), since the presence of gas hydrate significantly increases the bulk sediment velocity. Section 2.2 outlined three approaches to estimating gas hydrate concentration from velocity data: (1) porosity-velocity relations and effective porosity reduction, (2) time-averaging equations, and (3) rock-physics modeling. In this chapter, these methods are applied to velocity data at the locations of the IODP Expedition 311 transect across the Northern Cascadia gas hydrate area.

4.1 Downhole and Seismic Data

A large amount of velocity information has been collected over the Northern Cascadia gas hydrate area, including WL sonic logs at Sites U1325, U1326, U1327 (and ODP Site 889), and U1329, Vertical Seismic Profiles (VSPs) at Sites U1327 and 889, and normal moveout (NMO) velocities from MCS line 89-08, along the transect of wells drilled during IODP Expedition 311.

4.1.1 Sonic Log Measurements

IODP Expedition 311 downhole velocity data were measured by WL logging with the dipole sonic imager (DSI) tool. The DSI measures P- and S-wave transit times between a sonic transmitter and an array of eight receiver groups at 15 cm spacing (Riedel et al., 2006). P- and S-wave transit times (slowness) are used to compute P- and S-wave velocity, with the data processing done in real time. The vertical resolution of the tool is 107 cm, and the depth of investigation is ~10 cm.

The quality of the sonic log is highly dependent on borehole conditions, and requires good contact between the tool and the borehole wall. Unfortunately, the caliper arm broke off during the expedition (due to excessive ship heave), and borehole radius information was not recorded in the wireline holes. The quality of the sonic logs is therefore somewhat unknown, although the logs seem to generally be of good quality (Riedel et al., 2006), and in agreement with VSP and MCS velocities. A further setback caused by the loss of the caliper arm was that log porosity measurements were not made in the wireline holes (as they require a caliper arm). P-wave velocities from IODP Expedition 311 sonic logs are shown in Figure 4.1.

4.1.2 VSP Measurements

The well seismic tool (WST) was used at Site U1327 to produce a VSP. A geophone on the WST recorded the full waveform generated by a seismic source (a 1.68 L (105 in^3) Generator-Injector air gun) just below the sea surface. The WST was pressed against the borehole wall at 5 m intervals, and the air gun was fired between 7 and 15 times at each geophone depth (station). The measured VSP had 16 stations between 181 and 276 m below the seafloor. The VSP data were used to compute a velocity-depth

profile by the Expedition 311 scientists (Riedel et al., 2006), using the following procedure. (1) The recorded waveforms at each station were stacked to improve the signal-to-noise ratio, and the one-way traveltime was taken as the median of the first break arrival time of the P-wave at each station. (2) Corrections to one-way traveltime picks were applied for source depth (~2 m below the sea surface) and offset (~50 m). (3) The one-way traveltime vs. depth data were then inverted to obtain interval velocities, using a Bayesian technique that included a smoothness constraint (Malinverno and Briggs, 2004). The interval velocity vs. depth profile from the VSP at Site U1327 is shown in Figure 4.1.

4.1.3 MCS Velocity Measurements

Prior to IODP Expedition 311, a detailed velocity analysis was conducted at the proposed drilling locations, on MCS lines 89-08 and 89-10, which transect the four studied well sites. The lines were shot by Digicon Geophysical Corporation in 1989. The survey was collected using a DSS-240 recording system. The airgun array source was a tuned array with a total volume of 125 L (7820 in^3). Shots were recorded by a 3600 m streamer with 144 hydrophones, towed 183 m behind the vessel. The shot point interval was 50 m, for a bin spacing of 12.5 m, and 36-fold multiplicity. The record length was 14 s at a 4 ms sampling interval. The seismic sections are presented by Spence et al. (1991a), and a general discussion of the data is found in Spence et al. (1991b).

The processing flow applied before the velocity analysis was: (1) true amplitude recovery by spherical divergence corrections, (2) minimum phase Butterworth filtering to suppress high and low frequency noise, (3) gapped deconvolution to improve temporal resolution, and (4) dip moveout (DMO) correction in common-offset space (Hale, 1984).

The DMO correction allows for a NMO velocity analysis that accounts for non-horizontal reflectors.

Semblance NMO analysis accompanied by examination of constant velocity gathers was used for root mean square (RMS) velocity picking. RMS velocity picks were converted to interval velocities using the Dix equation (Dix, 1955), and two-way-traveltimes were converted to depth using the computed interval velocities. Calculated NMO interval velocities at the four sites of the well transect are shown in Figure 4.1. Common-depth points (CDPs) used in the analysis were within ~2.5 km of the drill sites. Interval velocities computed by Yuan et al. (1996) at ODP Site 889 are shown at Site U1327 for comparison.

There is generally good agreement between log, VSP and MCS velocity measurements at the well sites (Figure 4.1), with the exception of (1) a high velocity unit seen in the U1326 sonic log at 60-90 mbsf, not observed in the MCS velocities (explained by the location of Site U1326 being offset from MCS line 89-08), and (2) Site U1325, where log velocities are consistently lower than MCS velocities. However, the poor quality of the waveform measurements below 140 mbsf at U1325 suggests that velocity measurements below this depth may be affected by borehole enlargement (Riedel et al., 2006). For this site, MCS velocities are therefore preferred over log velocities. Higher log velocities compared to MCS velocities in U1326, below the BSR (~240 mbsf) can possibly be explained by the formation of a gas hydrate annulus around the borehole in the gas zone (Hyndman et al., 2001; Riedel et al., 2005). This might occur because cold drilling fluid (seawater) lowers the sediment temperature back into the stability field of gas hydrate. Alternatively, the base of the GHSZ might be lower than the seismically

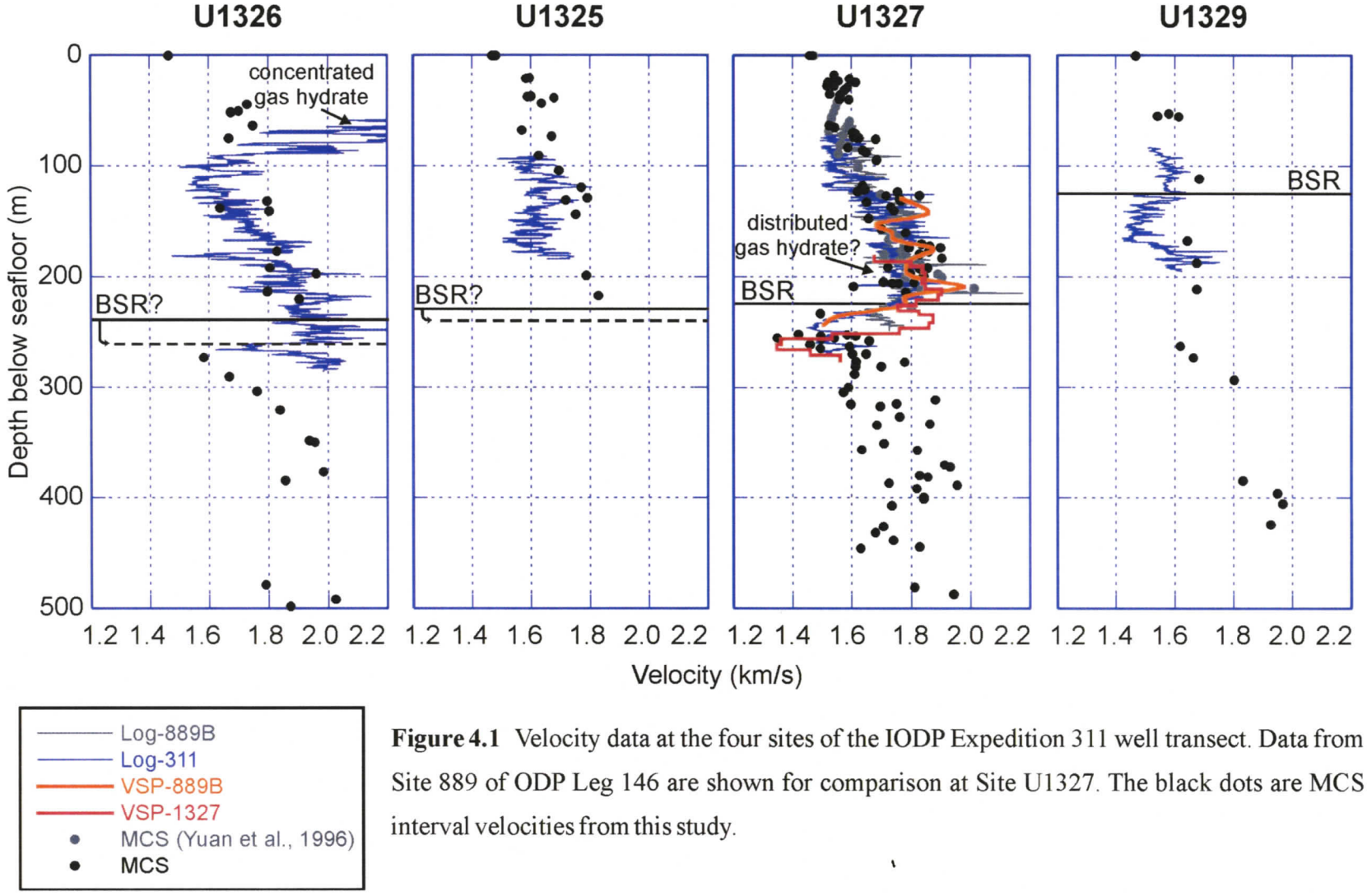

Figure 4.1 Velocity data at the four sites of the IODP Expedition 311 well transect. Data from Site 889 of ODP Leg 146 are shown for comparison at Site U1327. The black dots are MCS interval velocities from this study.

inferred BSR depth, as low salinity anomalies are also observed beneath 240 mbsf (Riedel et al., 2006, see Figure 3.4). The generally good agreement between the different (and independent) measurements of sediment velocity adds confidence to the accuracy of the measurements.

Figure 4.2 shows the different velocity data (log, VSP, and MCS) collected at Site 889/U1327. Sonic log measurements were made in holes 889A, 889B, and U1327E, and VSPs were shot in 889B and U1327D. The MCS velocity picks are those shown in Figure 4.1 (Site U1327), and were made on lines 89-08 and 89-10, within ~2.5 km of Site U1327. The general trend observed in all the WL sonic logs and from the MCS velocities is an increase in velocity from ~1500 m/s near the seafloor to ~1750 m/s at 150 mbsf, below which the velocity remains approximately constant until the BSR (~225 mbsf). A sub-BSR velocity decrease is observed in the sonic logs of 889B and U1327E, as well as in the MCS velocities. The VSP profile from holes 889B is taken from Hobro et al. (2005), who inverted the first break traveltime data to obtain velocities. Both VSPs are in reasonably good agreement with MCS and sonic log velocities, with the exception of the observed sub-BSR velocities in the U1327 VSP. The low velocity zone at ~260 mbsf can either be explained by a separate free gas zone well below the BSR at ~225 mbsf, or a deeper BSR at ~255 mbsf at this particular site.

4.1.4 Porosity Measurements

As discussed in Section 2.2, the use of sediment velocities to determine gas hydrate saturation requires knowledge of the formation porosity. For the velocity log analysis, it is preferable if the porosity is measured in the same hole as the velocity, so as to avoid discrepancies from inter-hole variability. Unfortunately, since the caliper arm

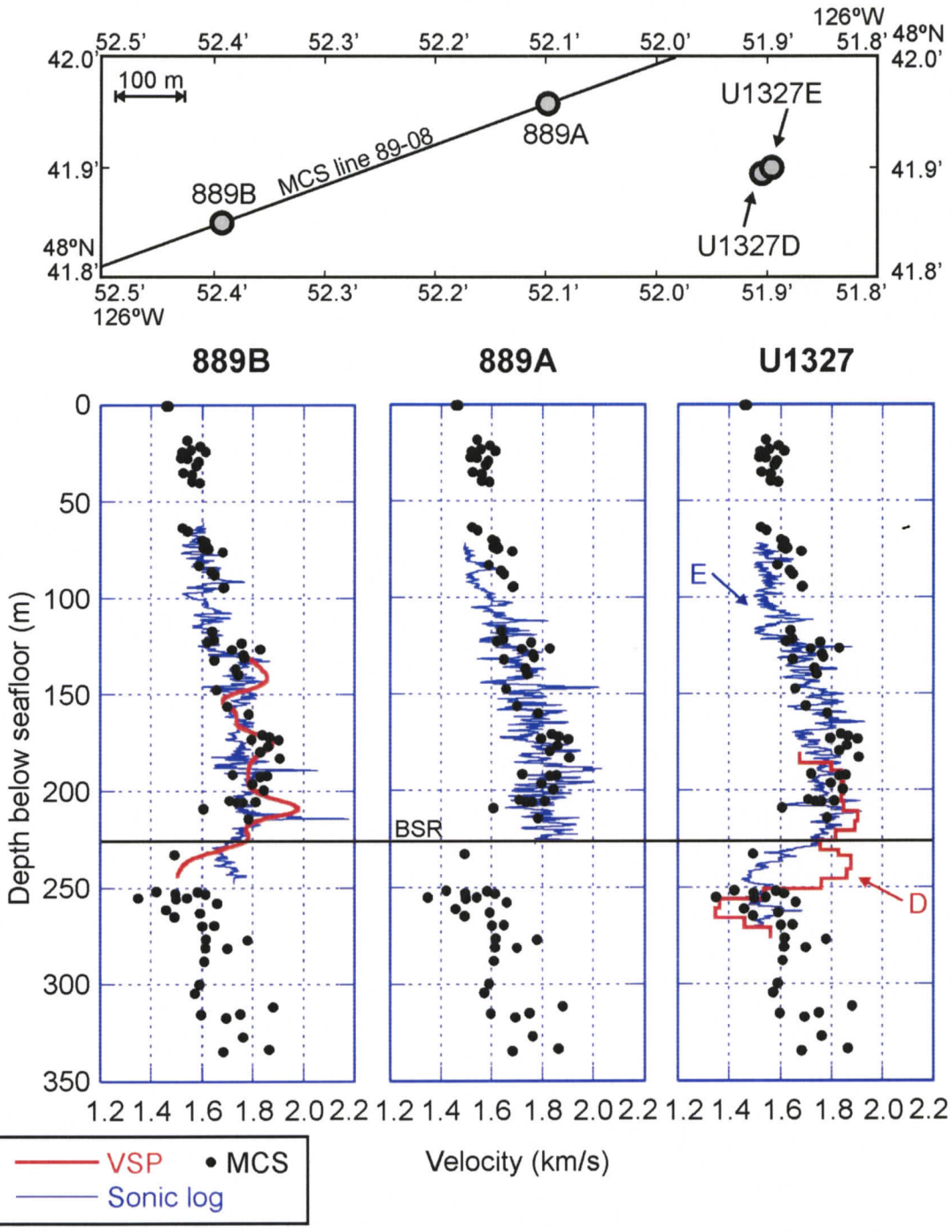

Figure 4.2 Compilation of log, VSP, and MCS velocity data at Sites 889 and U1327. WL sonic logs were recorded at 889A, 889B, and U1327E, and VSPs were taken at 889B and U1327D. The MCS velocities shown are NMO picks for this general area, taken from line 89-08 and line 89-10 (just SW of the map area shown). The sonic logs show minimal inter-hole variability, whereas the two VSPs differ significantly.

broke off the wireline tool string (Riedel et al., 2006), log porosity measurements were not made in the same holes where log velocities were measured. The approach taken here is to fit (in a least-squares sense) a smoothed porosity-depth profile to the LWD log density porosity at each site (Figure 4.3), using an Athy's Law type exponential decrease in porosity with depth (Athy, 1930, Equation 3.5). The use of the smoothed profile causes a loss in vertical resolution, but reduces uncertainties from inter-hole variability. The choice of a density porosity trend over a core porosity trend is justified by consistency in methods between the resistivity and velocity analyses.

4.2 Porosity-Velocity Relations and Effective Porosity Reduction

As discussed in Section 2.2.1, gas hydrate saturation S_h can be estimated using an effective porosity reduction model (Equation 2.7), if an empirical relation between porosity and velocity can be established in sediments containing no gas hydrate. Furthermore, because of the empirical nature of the approach, it is crucial that the porosity-velocity relation used be estimated from sediments similar to those for which gas hydrate saturation is to be estimated. In that respect, it is preferable if the porosity-velocity relation be derived from sediments in the same region. The two areas that respect the aforementioned criteria, and that could provide a reference porosity-velocity relation are (1) the Cascadia Basin, seaward of the deformation front, and (2) the Northern Cascadia accretionary prism, in areas far beneath the base of the GHSZ and the underlying free gas zone (Figures 1.3 and 1.4). Unfortunately, most wells drilled in Northern Cascadia have been in areas where no reliable reference velocities could be measured: drilling has generally been in areas where a BSR is observed seismically, and seldom deeper than the gas zone. The only candidate well site, where no-hydrate/no-gas

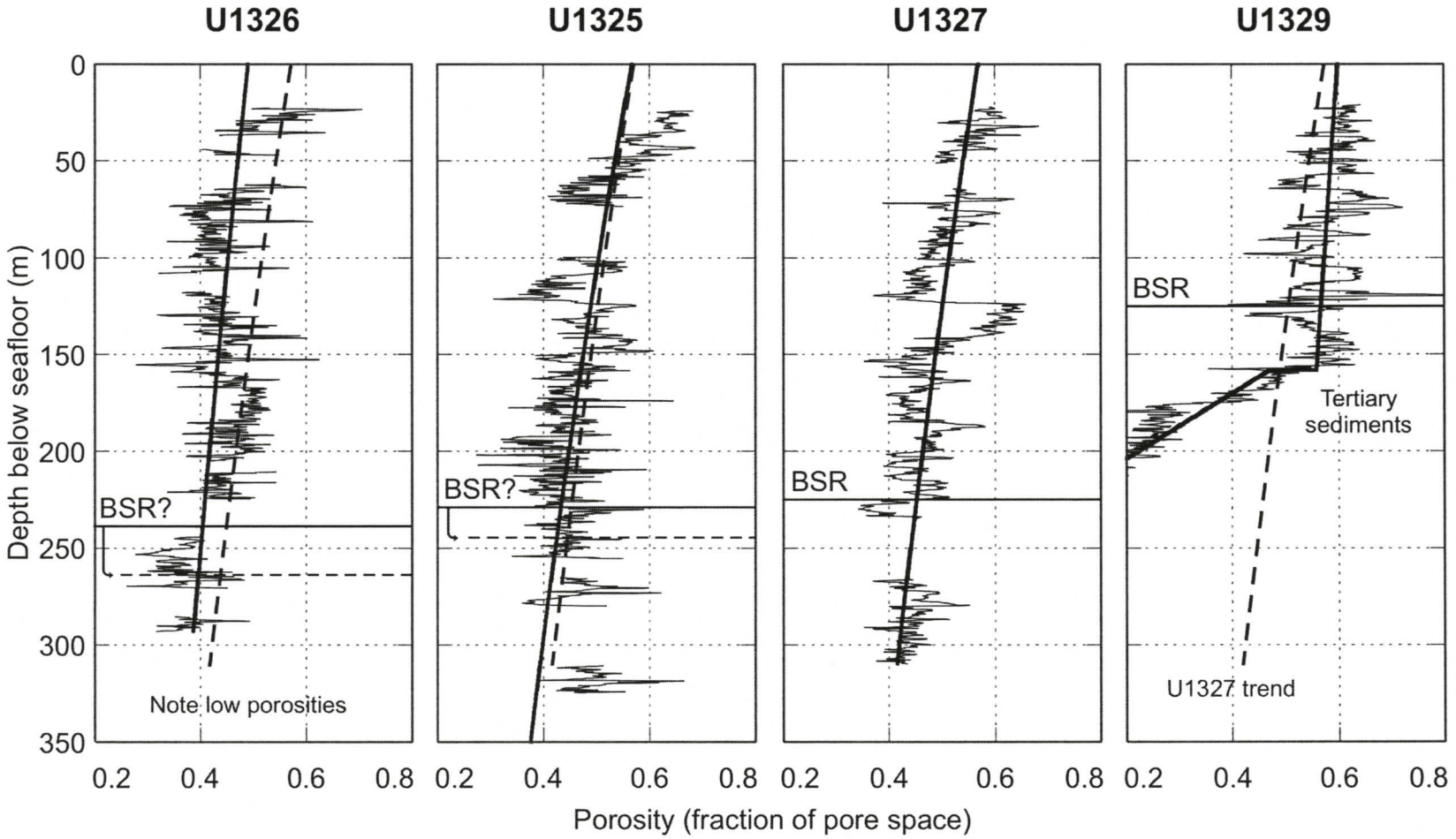

Figure 4.3 Downhole LWD density porosity measurements from IODP Expedition 311, at the four sites of the well transect. Zones with poor log quality have been removed. The bold line is a smoothed fit to the data, and the dashed line is the smoothed fit to U1327 porosities, shown at the other sites for comparison.

velocities and porosities have been measured, is Cascadia Basin Site 888, drilled during ODP Leg 146.

4.2.1 Cascadia Basin Site 888 Reference

The sediments of the Cascadia Basin are nearly undeformed because they have not yet entered the accretionary prism. They could provide a reference porosity-velocity relation, because gas hydrate is not thought to occur seaward of accretionary prism deformation fronts: according to the fluid expulsion model, it is the deformation-related fluid expulsion process occurring in accretionary prisms that provides the methane source for gas hydrate occurrence (Hyndman and Davis, 1992). From a mineralogical perspective, Cascadia Basin sediments should have the same composition as those in the accretionary prism that contain gas hydrate, since the accretionary prism sediments originate from the Cascadia Basin. However, there is concern that a reference porosity-velocity relation derived from undeformed sediments may not be applicable in the deformed sediments of the accretionary prism.

Figure 4.4 shows log velocity versus porosity data from Site 888, drilled seaward of the deformation front, in the Cascadia Basin, during ODP Leg 146. The data are too scattered to establish a trend, but are in good agreement with the porosity-velocity relation established by Hyndman et al. (1993) from core porosity and velocity data collected at the Nankai accretionary prism, at Site 808, during ODP Leg 131:

$$\varphi = -1.180 + \frac{8.607}{V} - \frac{17.89}{V^2} + \frac{13.94}{V^3}, \tag{4.1}$$

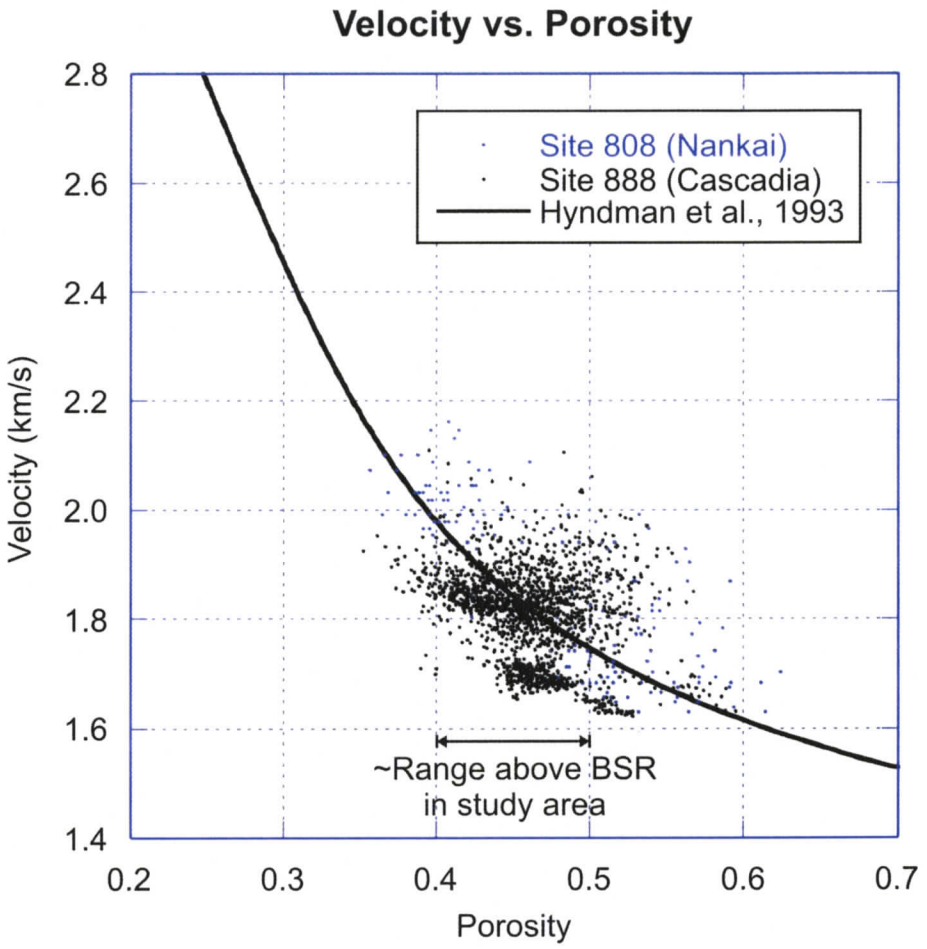

Figure 4.4 Log velocity vs. porosity from ODP Site 888 in the Cascadia Basin, with data from ODP Site 808 at the Nankai Trough, for comparison. The bold line is the porosity-velocity relationship of Hyndman et al. (1993), established from Nankai Trough core data.

where the velocity V is in km/s. The Hyndman et al. (1993) relation is also in agreement with Nankai LWD log data (ODP Leg 196) from the same site (Figure 4.4). The Nankai data are from clastic accretionary prism sediments similar to those of Cascadia.

To determine a reference velocity-depth profile at each site of the Expedition 311 transect, the Hyndman et al. (1993) relation is applied to the smoothed log density porosity profiles of each site (shown later in Figure 4.7).

4.2.2 Accretionary Prism Deep MCS Reference

An alternative reference porosity-velocity relationship for accreted sediments can be derived from MCS NMO velocities, obtained from intervals deep beneath the base of the GHSZ and the underlying free gas zone. Unfortunately, no direct porosity measurements have been made in that area (no deep drilling), but the deep MCS velocity-depth trend can be extrapolated to near-seafloor depths, where log porosity measurements exist.

NMO interval velocities from depths greater than 400 m below seafloor are used to calculate a velocity-depth trend in the deformed (accreted) sediments (Figure 4.5a). This trend is extrapolated to the seafloor, and used as a reference velocity profile for accreted sediments. NMO velocities in the Cascadia Basin, seaward of the deformation front, are also used to calculate a reference velocity-depth profile for undeformed (slope basin) sediments (Figure 4.5b). The accreted velocity-depth trend is used for Sites U1325, U1326, and U1327 at depths greater than 90 mbsf, and the slope basin trend is used for the upper 90 mbsf of Site U1327, and all of Site U1329 (shown later in Figure 4.7).

The smoothed porosity-depth profile at each site of the well transect is merged with the accreted and/or slope basin velocity-depth profile to obtain a site-specific porosity-velocity relation (Figure 4.6). The gas hydrate saturation is then calculated from Equation 2.7, by applying the appropriate porosity-velocity relation to the velocity data at that site (shown later in Figure 4.8).

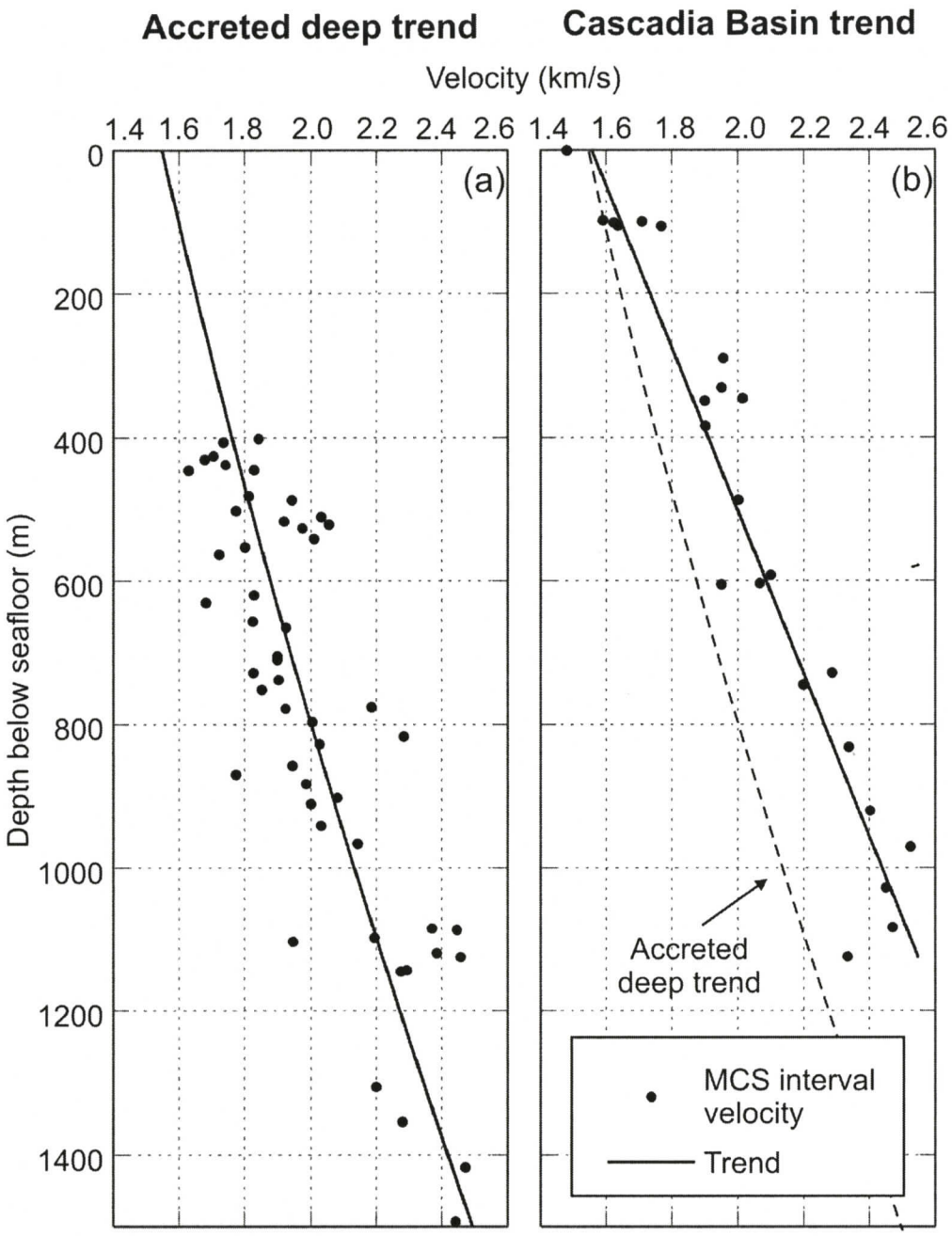

Figure 4.5 MCS interval velocities from (a) the deep accretionary prism and (b) the Cascadia Basin.

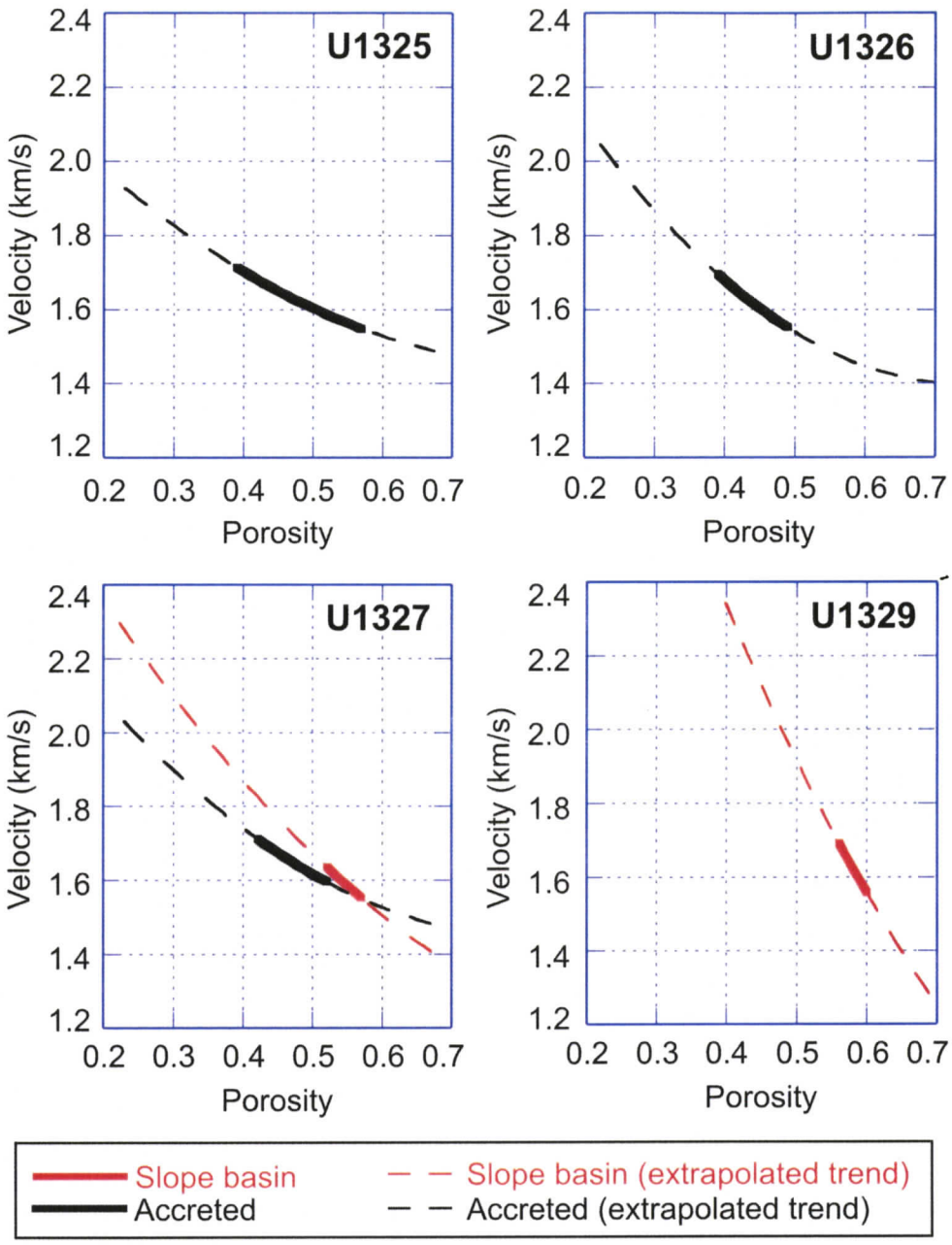

Figure 4.6 Porosity-velocity relationships established at each site, by merging the MCS velocity-depth trend with the site-specific porosity-depth trend. The red and black lines are for the slope basin and accreted sediments. The bold section of the curve represents the range of porosities measured at that site, and the dashed section indicates the range over which the relationship is extrapolated.

4.3 Time-Averaging Equations

The time-averaging approach of Lee et al. (1993), described in Section 2.2.2, is applied here to the smoothed porosity-depth profiles of each site. The arbitrary weighting factor W in Equation 2.12 is taken to be unity.

Application of the time-averaging method (Equations 2.9, 2.11 and 2.12) requires knowledge of the P-wave velocities and densities of the sediment constituents. Following Riedel (2001), an average mineralogy of 85% clay and 15% quartz is used, representative of results from petrophysical smear slide analyses from ODP Leg 146 (Westbrook et al., 1994) and IODP Expedition 311 (Riedel et al., 2006). P-wave velocities of the sediment constituents can be calculated from their elastic parameters. Table 4.1 summarizes the values used in this study, which are those reported by Helgerud (2001). Reference velocity-depth profiles for each site of the well transect are calculated from the Lee et al. (1993) time-averaging approach by taking $S_h = 0$ in Equations 2.9, 2.11 and 2.12 (shown later in Figure 4.7).

4.4 Rock-Physics Modeling

At each well site, a reference velocity-depth profile is calculated from the Helgerud (2001) rock-physics model (shown later in Figure 4.7), using the equations outlined in Section A.1 of the Appendix. Similarly to the Lee et al. (1993) time-averaging approach, the porosity is taken as the smoothed porosity-depth profile, and the average mineralogy is taken to be 85% clay and 15% quartz, with elastic parameters of the sediment constituents summarized in Table 4.1.

To estimate gas hydrate saturation, P-wave velocity vs. depth profiles for various gas hydrate saturations are computed, using both the gas hydrate in-pore (Appendix, A.2)

Sediment constituent	Bulk Modulus (GPa)	Shear Modulus (GPa)	Density (g/cm^3)	P-wave Velocity (km/s)	S-wave Velocity (km/s)
Clay	20.9	6.85	2.58	3.41	1.63
Quartz	36.6	45.0	2.65	6.04	4.12
Pore Water	2.4	0	1.03	1.5	0
Methane Hydrate	8.7	3.5	0.92	3.8	2.0
Methane Gas	0.1245	0	0.25	0.71	0

Table 4.1 Elastic properties of sediment constituents (After Helgerud, 2001).

and in-frame (Appendix, A.3) models. These constant gas hydrate saturation profiles are plotted with measured P-wave velocity data to provide an estimate of gas hydrate concentration based on both gas hydrate formation models (shown later in Figures 4.9 and 4.10). Free gas saturation below the base of the GHSZ is estimated in the same way, using the free gas in-pore model outlined in Section A.4 of the Appendix.

The effective medium rock-physics model of Helgerud (2001) also allows gas hydrate saturation to be estimated from S-wave velocity data. The gas hydrate in-pore model predicts S-wave velocities to be insensitive to gas hydrate occurrence. The gas hydrate in-frame model, however, predicts an increase in S-wave velocity with gas hydrate occurrence (because of added stiffness to the overall sediment frame), so S-wave velocity profiles for different gas hydrate saturations can be plotted with log S-wave velocity data from IODP Expedition 311 (shown later in Figure 4.11) to estimate gas hydrate saturation.

4.5 Comparison

4.5.1 Reference Velocity Profiles

Figure 4.7 provides a comparison of the reference (no-hydrate) velocity-depth profiles calculated using the methods outlined in this chapter. The reference profile calculated from MCS velocities is probably the most reliable, because it is the only one based entirely on measured data from the study area, and is therefore the best calibrated. However, there is still significant uncertainty in the MCS-based reference velocity profile for accreted sediments, since the MCS deep velocity trend must be extrapolated to shallow depths. Reference velocity profiles calculated from both the time-averaging and rock-physics modeling approaches are considered relatively poorly calibrated, since the velocity profiles are quite sensitive to the mineral assemblage chosen. The reference velocity profile obtained from the porosity-velocity relation of Hyndman et al. (1993) also has substantial uncertainty: even though the relation fits the log data from Cascadia Basin Site 888 (Figure 4.4), the scatter in the log data indicate a poorly constrained relation between velocity and porosity.

A general observation is that the reference velocities calculated from the Hyndman et al. (1993) empirical porosity-velocity relation and the Lee et al. (1993) time-averaging approach are significantly greater than those calculated from the MCS velocity trend and the Helgerud (2001) rock-physics model (Figure 4.7). In fact, at all four sites, velocity measurements (log, VSP, and MCS) lower than both the Hyndman and Lee references are observed in several areas above the BSR. Therefore to validate either of these two reference profiles, an explanation for lower-than-reference velocities above the

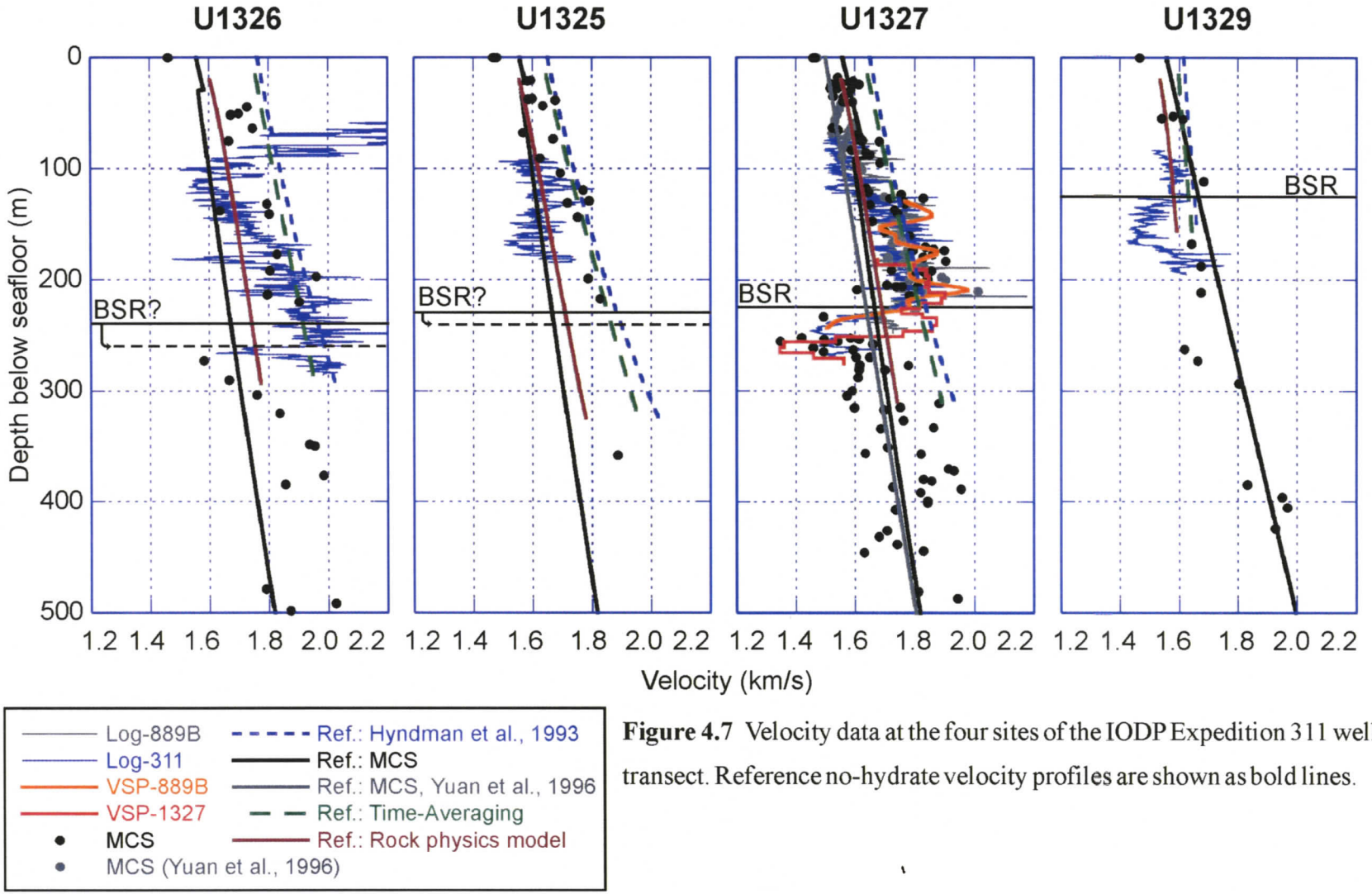

Figure 4.7 Velocity data at the four sites of the IODP Expedition 311 well transect. Reference no-hydrate velocity profiles are shown as bold lines.

BSR is required. Since free gas should not occur above the BSR, it would seem more likely that the Hyndman and Lee references are not appropriate for these sediments.

A possible explanation for the unusually high reference velocities obtained is that the Hyndman et al. (1993) relation is calibrated to log velocity and porosity data from undeformed sediments of the Cascadia Basin, which could exhibit a different porosity-velocity relationship than the deformed accretionary prism sediments. Although the exact reason for the unusually high reference velocities predicted by this method is uncertain, it can be attributed in general to an unreliable empirical calibration. A further uncertainty in applying this relationship to Expedition 311 data is that the porosities at Site 888 were measured using a different logging tool. The resistivity analysis of Chapter 3 has shown that the use of empirical relations requires calibration to an appropriate reference, so uncertainty arises when the empirical relationship used is calibrated to measurements from a different tool than the one used in calculating gas hydrate saturation.

The unusually high reference velocities predicted by time-averaging approach of Lee et al. (1993) can be explained by the need to use an arbitrary weight W (Equation 2.12) that biases the result towards either the Wyllie et al. (1958) velocity (valid for consolidated sediments) or Wood (1941) velocity (valid for particles in suspension). In a sense, the unusually high velocities are obtained because the weight chosen ($W = 1$) is too large, given the actual degree of sediment consolidation. More reasonable reference velocities would therefore be obtained if a smaller value of W was chosen, but the choice of W is somewhat arbitrary in that its value does not represent a measurable degree of sediment consolidation.

The reference velocity-depth profiles obtained from the rock-physics modeling approach of Helgerud (2001) are preferred to those obtained from the Lee et al. (1993) time-averaging approach, because they are calculated from first-principles, and do not require the use of an empirical weighting factor. Although a substantial degree of uncertainty related to the choice of mineral constituents and their elastic parameters is inherent, results are generally in reasonable agreement with the no-hydrate MCS velocity trend. One exception is at Site U1326, where a substantially higher reference velocity profile is obtained from rock-physics than from MCS. This is well explained by the observation that the porosity at Site U1326 is lower than at the other sites (Figure 4.3), indicating to first order that the reference velocity at this site should be greater than at the other sites. This feature is well captured by the rock-physics model, since it incorporates sediment porosity in the velocity calculation. However, the (regional) MCS velocity trend does not account for local variations in porosity (which would affect the no-hydrate velocity), and is therefore clearly less applicable at Site U1326.

4.5.2 Gas Hydrate Saturation

Following the discussion on relative reliability of the tested approaches to obtain reference velocity-depth profiles and calculate gas hydrate saturation, the porosity reduction approach using the Hyndman et al. (1993) porosity-velocity relation, and the Lee et al. (1993) time-averaging approach are discarded. Gas hydrate saturation is calculated from (1) porosity reduction applied to the porosity-velocity relation obtained by merging the no-hydrate MCS velocity trend with the site-specific smoothed log porosity trend (Figure 4.8), and from (2) the Helgerud (2001) rock-physics modeling approach (Figures 4.9, 4.10, and 4.11).

Gas hydrate saturation from the effective porosity reduction approach (Figure 4.8) gives highest gas hydrate saturations at Site U1326, where the interval at the top of the sonic log (60-90 mbsf) yields gas hydrate saturations of > 0.50. In the interval 185-240 mbsf an average gas hydrate saturation of ~0.30 is calculated. However, as discussed in Section 4.5.1, rock-physics modeling probably gives more accurate estimates at U1326, because it accounts for site-specific variations in porosity. The MCS velocity data from Site U1325 indicate a gradual increase in gas hydrate saturation from near zero at the seafloor to ~0.30 at the BSR. Velocity data from Site U1327 show no gas hydrate in the slope basin portion of the sediment section (0-90 mbsf), and gas hydrate saturation of ~0.22, on average, in the interval 150-225 mbsf, just above the BSR. This is in reasonably good agreement with the estimates of Yuan et al. (1996) at ODP Site 889. Site U1329 shows no indication of gas hydrate occurrence from the velocity data.

The main sources of error in gas hydrate saturation estimates from the effective porosity reduction method are related to (1) the uncertainty in the reference velocity profile, and (2) the uncertainty in the site-specific porosity-velocity relation; uncertainties in the actual velocity measurements are significantly less important. Uncertainty in the Cascadia Basin reference profile is relatively low, as the MCS velocities show a well established trend (Figure 4.5b). The uncertainty in the near-seafloor accreted trend is greater, because of the need to extrapolate the deeper velocity trend to the seafloor (Figure 4.5a). The main source of uncertainty in the site-specific porosity-velocity relationships arises from the need to extrapolate outside the range of observed porosities. In Figure 4.6, the solid segments of the lines indicate the range of porosity and velocity values from which the relationship was established, and the dashed segments indicate the

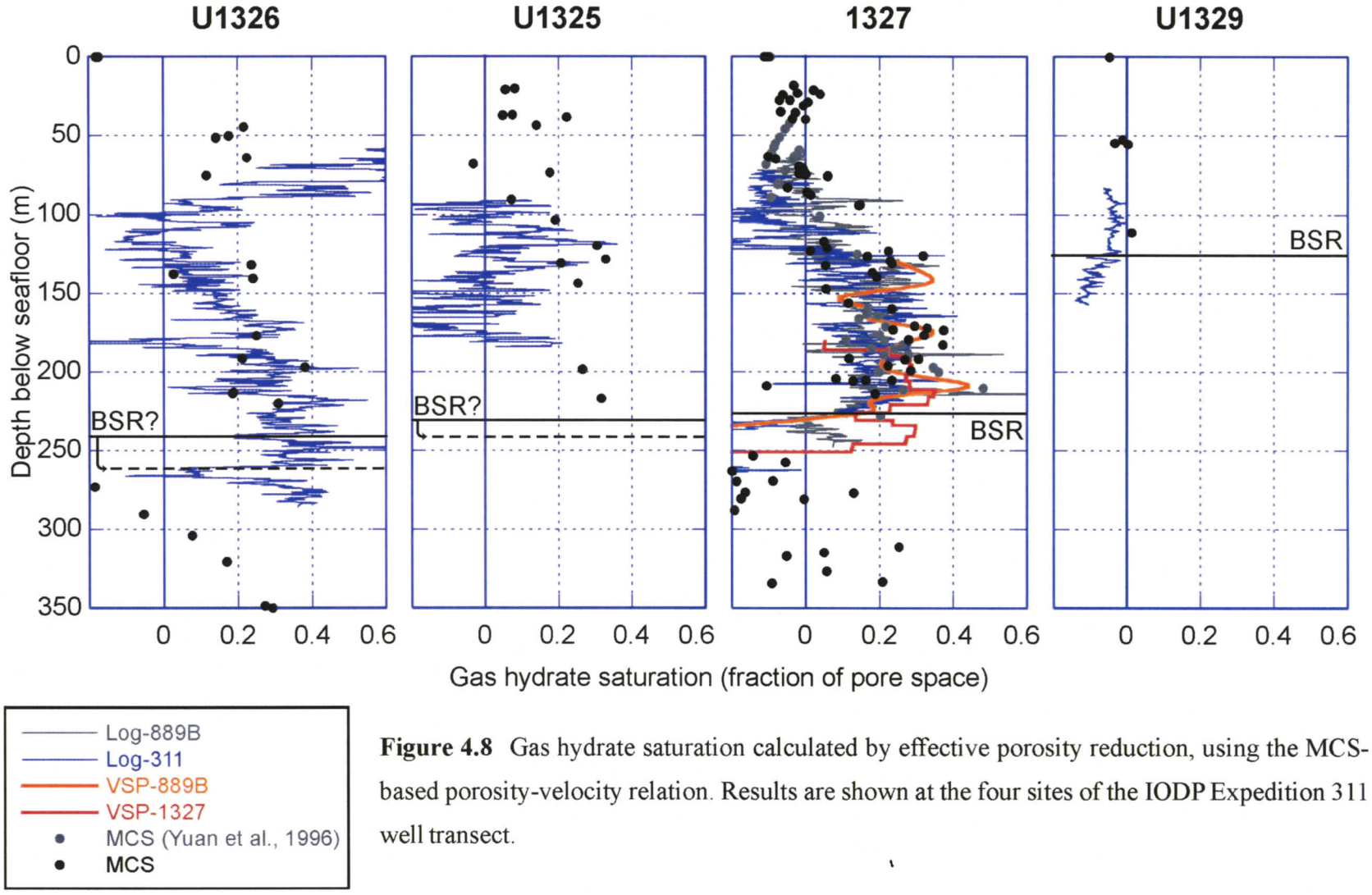

Figure 4.8 Gas hydrate saturation calculated by effective porosity reduction, using the MCS-based porosity-velocity relation. Results are shown at the four sites of the IODP Expedition 311 well transect.

values over which the relationship was extrapolated. In the effective porosity reduction approach, zones with high gas hydrate saturation exhibit higher velocities, so the porosity-velocity relation yields a lower (hydrate-excluding) effective porosity φ_e, and Equation 2.7 then gives the appropriate gas hydrate saturation, since $\varphi_e < \varphi$. However, additional uncertainty arises in the estimate of φ_e if its value is estimated by extrapolating outside the range of observed porosities. This problem is one of common occurrence in the use of empirical methods: empirical relations are best applied over the range of values from which they are calibrated. Confidence in the porosity-velocity relations used could be greatly increased if the relation was further calibrated in sediments with lower porosities (and higher velocities), e.g., from deep within the accretionary prism.

The relative importance of the uncertainty in the reference velocity profile and in the site-specific porosity-velocity relation probably depends on the gas hydrate saturation itself. At relatively low gas hydrate saturations, the uncertainty in the reference velocity profile should dominate, since a small change in the reference velocity will strongly influence the estimated magnitude of the velocity increase due to gas hydrate occurrence. At relatively high gas hydrate saturations, the uncertainty in the site-specific porosity-velocity relation is probably dominant, since the (high) velocities measured in these areas coincide with (low) effective porosity estimates, outside the range of measured porosities, and are therefore poorly calibrated due to the need for substantial extrapolation.

Figures 4.9 and 4.10 show gas hydrate saturation estimates from the gas hydrate in-pore and in-frame rock-physics models, estimated from P-wave velocity data. The gas hydrate in-frame model predicts slightly lower gas hydrate saturations, but the differences between the model predictions are small (< 0.10), and within the uncertainty of the S_h

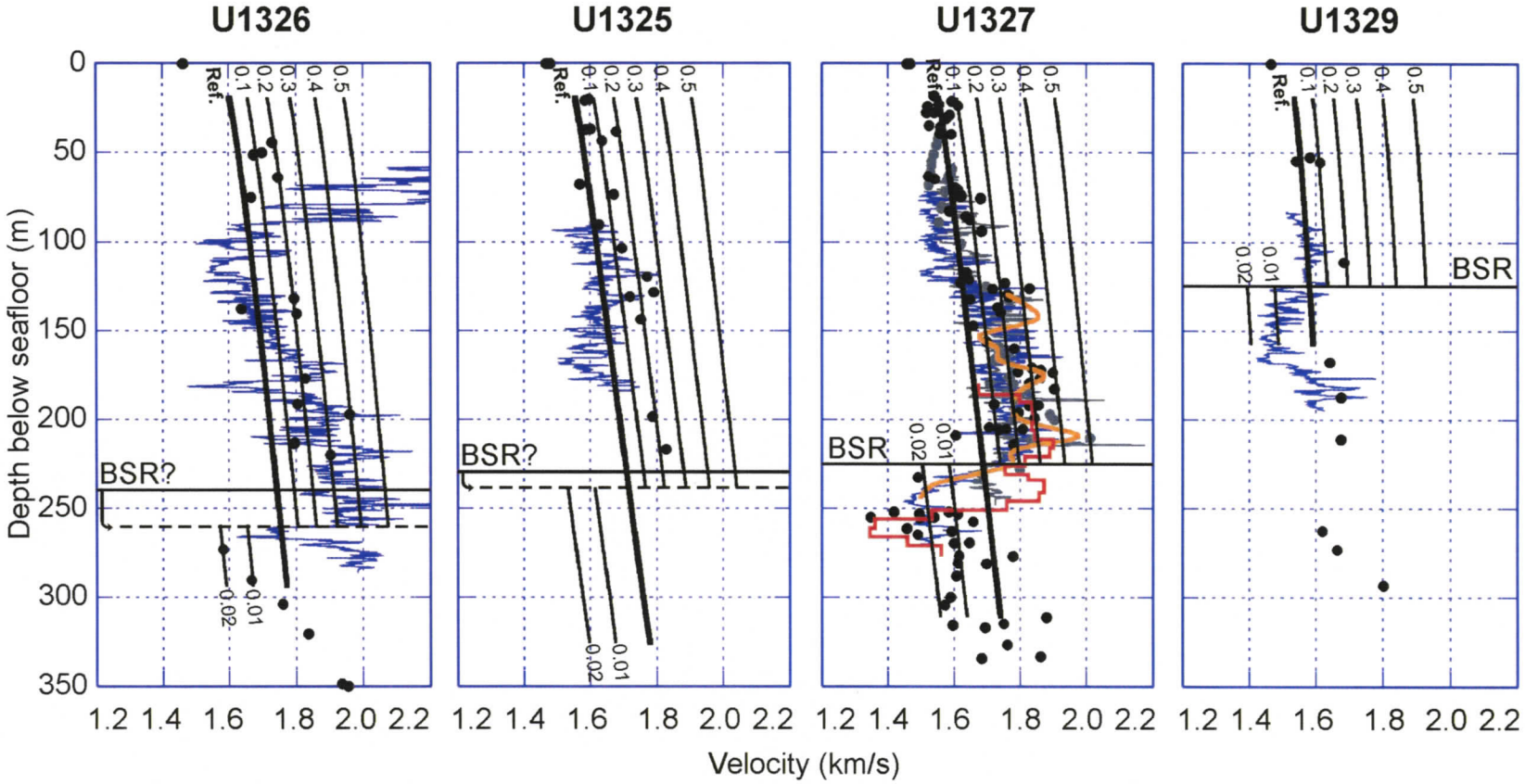

Figure 4.9 Gas hydrate and free gas saturation from P-wave velocity measurements, based on the gas hydrate in-pore rock physics model. The bold black line is the no-hydrate reference. Sub-parallel lines to the left are lines of constant free gas saturation (0.01 increments) and to the right are lines of constant gas hydrate saturation (0.10 increments).

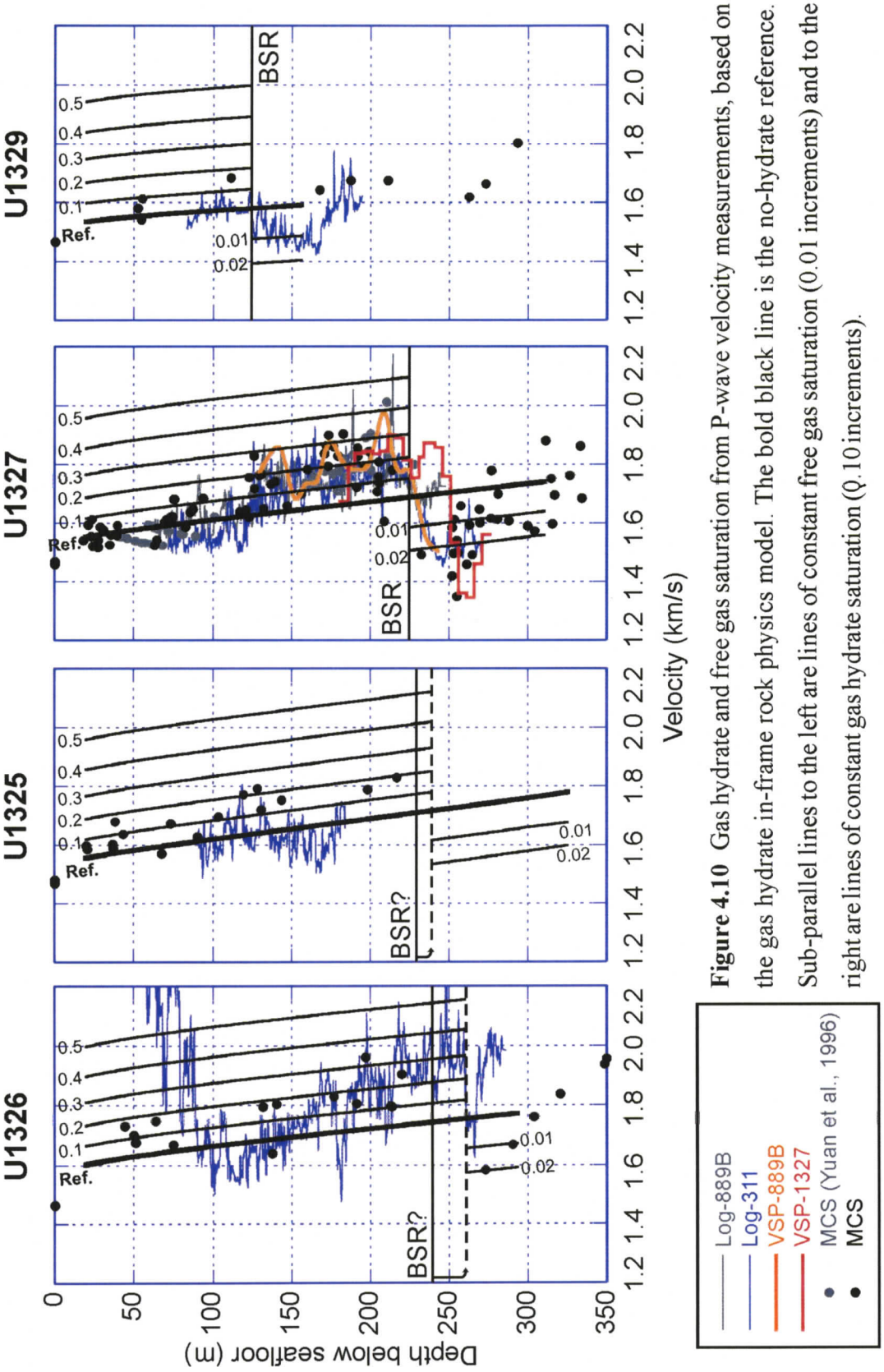

Figure 4.10 Gas hydrate and free gas saturation from P-wave velocity measurements, based on the gas hydrate in-frame rock physics model. The bold black line is the no-hydrate reference. Sub-parallel lines to the left are lines of constant free gas saturation (0.01 increments) and to the right are lines of constant gas hydrate saturation (0.10 increments).

estimates themselves. Gas hydrate saturation estimates from both models are generally in good agreement with results from the porosity reduction approach. Studies by Helgerud (2001) and Riedel (2001) however, preferred the gas hydrate in-frame model for marine gas hydrate. The effective medium modeling also allows for the estimation of free gas saturation in the sediments immediately below the BSR. P-wave velocity data at Site U1327 predict a free gas saturation of 0.01-0.03, MCS velocities at Site U1326 show saturations of 0.01-0.02, and log velocities from U1329 show saturations of 0.01. Finally, the gas hydrate in-frame formation model can also be used to estimate gas hydrate saturation from S-wave velocity data (Figure 4.11). In this case, the quality of the log S-wave velocity data from IODP Expedition 311 is not of good enough quality to provide reliable estimates of S_h. However, the data do provide good evidence refuting the gas hydrate in-pore model, which predicts background S-wave velocities to be unaffected by the presence of gas hydrate. In the high S_h area in U1326, in the interval 60-90 mbsf, both P- and S-wave velocities appear to be enhanced by the occurrence of gas hydrate, supporting the gas hydrate in-frame formation model, where the presence of gas hydrate adds some rigidity to the sediment frame.

The main source of uncertainty in gas hydrate saturation estimates from the rock-physics modeling approach is related to the choice of the mineral assemblage used to build the model, and the elastic properties of those minerals. Also, the extent to which the gas hydrate in-pore and in-frame formation models accurately depict physical processes by which gas hydrate forms is potentially a further source of error.

At Site U1326, in the interval ~60-90 mbsf, a zone with very high velocities, up to 3000 m/s, was measured by the sonic log. Figure 4.12 shows gas hydrate saturation

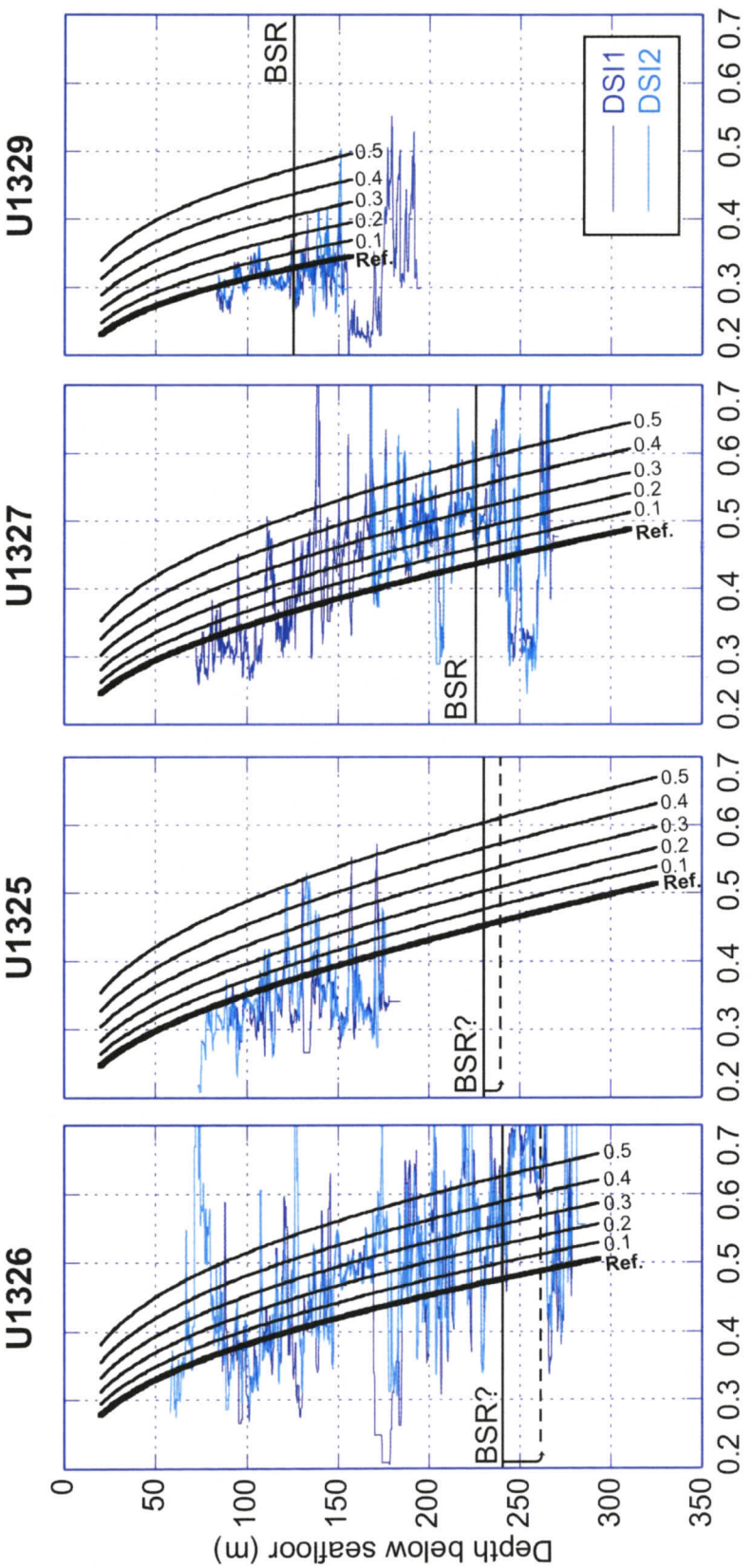

Figure 4.11 Gas hydrate saturation from log shear-wave velocity, based on the gas hydrate in-frame rock physics model. The bold black line is the no-hydrate reference. Sub-parallel lines to the right are lines of constant gas hydrate saturation (0.10 increments).

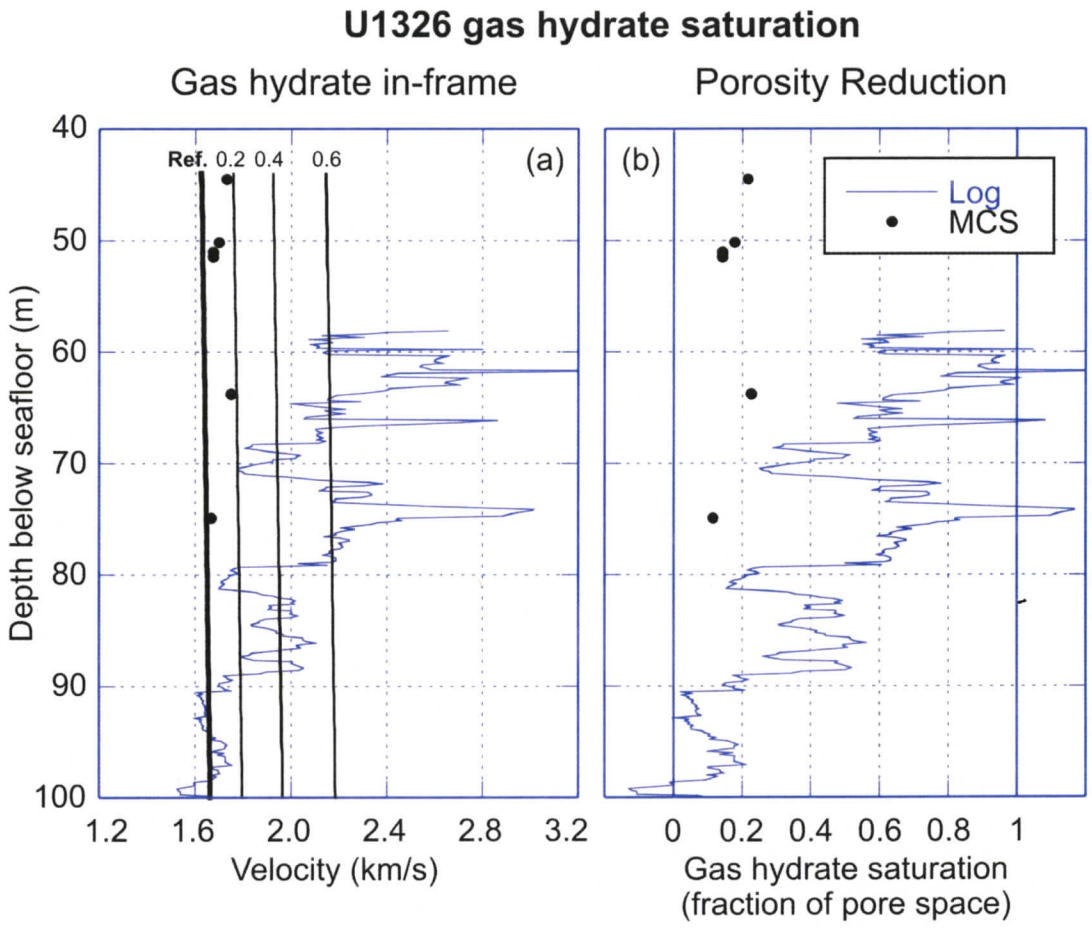

Figure 4.12 Log and MCS based gas hydrate saturation estimates for the upper section of Site U1326 from (a) the gas hydrate in-frame rock physics model, and (b) effective porosity reduction. In (a), the bold black line is the no-hydrate reference. Sub-parallel lines to the right are lines of constant gas hydrate saturation (0.2 increments).

estimates in this zone, using both the gas hydrate in-frame rock-physics model and effective porosity reduction. Both methods suggest that some areas contain well over 60% gas hydrate pore space saturation. However, both methods have much larger uncertainties when used in cases of higher gas hydrate saturations. As discussed for the effective porosity reduction approach, the porosity-velocity relation is less well constrained at higher velocities (lower porosities). In the case of the gas hydrate in-frame

rock-physics model, at high gas hydrate saturations, it is unlikely that gas hydrate occurs simply as part of the load-bearing sediment frame; at least some cementation probably occurs. If this is the case, the results based on the gas hydrate in-frame rock-physics model are likely overestimates. However, observed velocities up to 3000 m/s in this interval do qualitatively indicate that a substantial amount of gas hydrate is present.

Chapter 5

AVO Inversion of Gas Hydrate BSRs

This chapter examines the usefulness of AVO analysis of BSRs in estimating associated marine gas hydrate and free gas concentrations. A nonlinear Bayesian inversion is applied to BSR AVO data from MCS line 89-08, near IODP Site U1327. The Bayesian approach allows results to be accompanied with quantitative error estimates.

5.1 AVO Studies of Gas Hydrate BSRs

The successful use of seismic AVO studies as hydrocarbon indicators in the oil and gas industry has prompted the scientific community to use AVO as a tool in gas hydrate-related BSR studies (e.g., Hyndman and Spence, 1992; Andreassen et al., 1997; Ecker et al., 1998; Yuan et al., 1999). AVO data can be gathered from multichannel streamer data, and provide information about the sediment density and both its compressional- (P-) wave and shear- (S-) wave velocity. The occurrence of gas hydrate in sediment pore space should increase both P- and S-wave velocities above the BSR (e.g., Helgerud, 2001). Below the BSR, the occurrence of free gas should significantly reduce P-wave velocities (e.g., Gregory, 1976), while not greatly influencing S-wave velocities (relative to a no-gas reference). Changes in both P- and S-wave velocities should

therefore occur across the BSR, making gas hydrate studies a potential candidate for AVO analysis.

The common approach in gas hydrate AVO studies has previously been to estimate gas hydrate and free gas concentrations immediately above and below the BSR, by matching the measured AVO response of the BSR to synthetic AVO curves representative of different gas hydrate/free gas concentration scenarios and rock-physics models (Andreassen et al., 1997; Ecker et al., 1998; Yuan et al., 1999). However, forward modeling schemes do not rigorously consider the uncertainties of the AVO problem, related to both the non-unique nature of the solution and the uncertainty in the AVO data. The large uncertainties caused by non-uniqueness of AVO solutions were recognized by Yuan et al. (1999), who studied the AVO response of BSRs in Northern Cascadia through forward modeling, and found that scenarios with high gas hydrate concentration above the BSR and low free gas concentration below could not be distinguished from scenarios with low gas hydrate concentration above the BSR and high free gas concentration below. This finding highlights the need to include quantitative uncertainty analysis in AVO studies. To achieve this, an amplitude-preserving data processing scheme must be implemented, data uncertainties (such as measurement of reflection coefficients and incidence angles) need to be estimated quantitatively, and the inversion approach must fully explore the solution space of the problem.

The objective of this study is to determine to what extent AVO data from BSRs can be used to estimate associated gas hydrate and free gas concentrations. To this end, a nonlinear Bayesian inversion is applied to BSR AVO data to obtain estimates and uncertainties of formation physical parameters (P- and S-wave velocities and densities),

which are then used to estimate gas hydrate and free gas concentrations. The Bayesian approach treats model parameters as random variables, giving their estimates in terms of probability distributions (e.g., Sen and Stoffa, 1996; Riedel et al., 2003), thus quantifying model uncertainties. Gas hydrate and free gas concentration estimates apply to the sediments immediately above and below the BSR. The vertical resolution of the estimates depends on the seismic wavelength, which is ~50 m at BSR depths, for the MCS data used here.

This chapter examines a set of synthetic test cases emulating MCS data with a strong BSR to assess the potential for successful AVO inversion of BSR data. Constraints based on prior knowledge of physical parameters, including theoretical or empirical relationships between parameters are implemented in an attempt to further constrain the problem. The inversion is then applied to BSR AVO data collected near IODP Site U1327, and provides quantitative constraints on the range of gas hydrate and free gas concentrations immediately above and below the BSR. Finally, as a reference test, the inversion is applied to synthetic data from the now classic Ostrander (1984) gas sand model, and the results are compared to those of the BSR study.

5.2 Theory

5.2.1 Zoeppritz Equations

AVO theory is based on the Zoeppritz (1919) equations, expressing the reflection and transmission coefficients of a plane wave incident on a planar interface between two homogeneous media as a function of the angle of incidence and the elastic properties of

the media (Figure 5.1). Of interest in MCS studies are P-to-P reflections, described in terms of the reflection coefficient R

$$R = \left[\left(b\frac{\cos\theta}{Vp_1} - c\frac{\cos\omega}{Vp_2} \right) F - \left(a + d\frac{\cos\theta}{Vp_1}\frac{\cos\psi}{Vs_2} \right) Hp^2 \right] \Big/ D, \tag{5.1}$$

with

$$a = \rho_2\left(1 - 2Vs_2^2 p^2\right) - \rho_1\left(1 - 2Vs_1^2 p^2\right), \qquad b = \rho_2\left(1 - 2Vs_2^2 p^2\right) + 2\rho_1 Vs_1^2 p^2,$$

$$c = \rho_1\left(1 - 2Vs_1^2 p^2\right) + 2\rho_2 Vs_2^2 p^2, \qquad d = 2\left(\rho_2 Vs_2^2 - \rho_1 Vs_1^2\right),$$

$$E = b\frac{\cos\theta}{Vp_1} + c\frac{\cos\omega}{Vp_2}, \qquad F = b\frac{\cos\zeta}{Vs_1} + c\frac{\cos\psi}{Vs_2},$$

$$G = a - d\frac{\cos\theta}{Vp_1}\frac{\cos\psi}{Vs_2}, \qquad H = a - d\frac{\cos\omega}{Vp_2}\frac{\cos\zeta}{Vs_1},$$

$$D = EF + GHp^2,$$

where Vp, Vs, and ρ are respectively, P-wave velocity, S-wave velocity, and bulk density (with subscripts *1* and *2* indicating the upper and lower media). The incidence angle is θ, ω and ψ are the P-wave and converted S-wave transmission angles, and ξ is the S-wave reflection angle related by Snell's law:

$$p = \frac{\sin\theta}{Vp_1} = \frac{\sin\omega}{Vp_2} = \frac{\sin\zeta}{Vs_1} = \frac{\sin\psi}{Vs_2}, \tag{5.2}$$

where p is the ray parameter.

5.2.2 Bayesian Inversion

Bayesian methods can be applied to geophysical inverse problems to provide quantitative uncertainty estimates and can include constraints from prior information

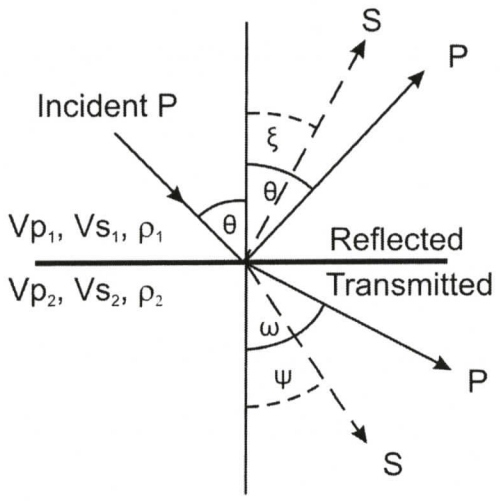

Figure 5.1 Schematic ray diagram of the partitioning of an incident P-wave into reflected and transmitted P- and converted S-waves at a half-space/half-space interface.

(e.g., Tarantola, 1987; Sen and Stoffa, 1996). The method used in this study follows the approach of Riedel et al. (2003), who inverted seafloor AVO data for seabed properties.

Consider a vector of N observed AVO data $\mathbf{R}^{\mathbf{obs}}$ (i.e., P-wave reflection coefficients at the N angles of incidence), related to a model $\mathbf{m} = [Vp_1, Vs_1, \rho_1, Vp_2, Vs_2, \rho_2]^T$ of physical parameters by a function $\mathbf{R}^{\mathbf{obs}} = \mathbf{R(m)} + \mathbf{n}$, where $\mathbf{R}$ represents the Zoeppritz equations. For Gaussian-distributed errors $\mathbf{n}$ with data covariance matrix $\mathbf{C_D}$, the likelihood function is

$$L\left(\mathbf{R}^{\text{obs}}\middle|\mathbf{m}\right)=\frac{1}{(2\pi)^{N/2}\left|\mathbf{C_D}\right|^{1/2}}\exp\left\{-\frac{1}{2}\left[\mathbf{R(m)}-\mathbf{R}^{\text{obs}}\right]^T\mathbf{C_D}^{-1}\left[\mathbf{R(m)}-\mathbf{R}^{\text{obs}}\right]\right\}. \tag{5.3}$$

In Bayesian inversion, the data and model vectors are considered random variables that obey Bayes' rule, which can be written as

$$P\left(\mathbf{m}\,|\mathbf{R}^{\text{obs}}\right)\propto L\left(\mathbf{R}^{\text{obs}}\middle|\mathbf{m}\right)P\left(\mathbf{m}\right), \tag{5.4}$$

where $P(\mathbf{m}|\mathbf{R}^{\text{obs}})$ represents the posterior probability distribution (PPD) and $P(\mathbf{m})$ is the prior distribution. For likelihood $L(\mathbf{R}^{\text{obs}}|\mathbf{m}) \propto \exp[-E(\mathbf{m})]$, where the error function $E(\mathbf{m})$

is the argument of the exponential function in Equation 5.3, the normalized PPD may be written as

$$P(\mathbf{m}|\mathbf{R}^{\text{obs}}) = \frac{\exp[-\lambda(\mathbf{m})]}{\int \exp[-\lambda(\mathbf{m}')]d\mathbf{m}'}, \tag{5.5}$$

where $\lambda(\mathbf{m}) = E(\mathbf{m}) - \ln P(\mathbf{m})$, and the domain of integration spans the model space.

From a Bayesian viewpoint, $P(\mathbf{m}|\mathbf{R}^{\text{obs}})$ is the general solution of the inverse problem; however, to interpret the PPD for multidimensional problems requires the computation of integral properties (moments) of the distribution, such as the posterior mean, model covariance matrix, and marginal probability distribution (MPD) of parameter m_i, defined respectively as

$$\langle \mathbf{m} \rangle = \int \mathbf{m}' P(\mathbf{m}'|\mathbf{R}^{\text{obs}}) d\mathbf{m}', \tag{5.6}$$

$$\mathbf{C}_{\text{M}} = \int (\mathbf{m}' - \langle \mathbf{m} \rangle)(\mathbf{m}' - \langle \mathbf{m} \rangle)^T P(\mathbf{m}'|\mathbf{R}^{\text{obs}}) d\mathbf{m}', \tag{5.7}$$

$$P(m_i|\mathbf{R}^{\text{obs}}) = \int \delta(m_i' - m_i) P(\mathbf{m}'|\mathbf{R}^{\text{obs}}) d\mathbf{m}', \tag{5.8}$$

where δ is the Dirac delta function. Two-dimensional (joint) MPDs illustrate interrelationships between parameters and are defined similarly to Equation 5.8. Equations 5.6-5.8 and can be written in the general form

$$I = \int f(\mathbf{m}') P(\mathbf{m}'|\mathbf{R}^{\text{obs}}) d\mathbf{m}'. \tag{5.9}$$

MPDs can also be used to calculate highest probability density "credibility intervals": the smallest interval in the model space containing a given percentage of the total probability. To solve the integral of Equation 5.8 for nonlinear problems, a Metropolis Gibbs' sampling (GS) approach is used (Dosso, 2002; Riedel et al., 2003). The model is

perturbed repeatedly, with perturbations accepted if a uniform random number η on [0,1] satisfies

$$\eta \leq \exp[-\Delta E]. \tag{5.10}$$

Markov chain analysis (Gilks et al., 1996) verifies that, for a large number of perturbations, the GS equilibrium distribution is equivalent to the PPD. Hence, the integral I can be estimated by means of $f(\mathbf{m})$ as evaluated from the sample of Q models collected by GS (e.g., Sen and Stoffa, 1996; Riedel et al., 2003):

$$I \approx \frac{1}{Q}\sum_{i=1}^{Q} f(\mathbf{m}_i). \tag{5.11}$$

The efficiency of the sampling is greatly enhanced by rotating to a principal component system by diagonalizing an estimate of the model covariance matrix $\mathbf{C_M}$. Initially, a linearized estimate of $\mathbf{C_M}$ is used; this is adaptively updated as the sampling proceeds.

Convergence is based on applying the GS procedure in parallel to simultaneously collect two independent samples of models. When the maximum difference between the cumulative MPD's for all parameters is smaller than a pre-set threshold, the procedure has converged and the final sample is taken to be the union of the two independent samples (Dosso, 2002).

Bayesian inversion requires an estimate of the data covariance matrix $\mathbf{C_D}$, including both measurement and theory errors. Here, $\mathbf{C_D}$ is assumed to be of the form:

$$\mathbf{C_D} = \hat{\sigma}^2\mathbf{I} + \mathbf{C_0}, \tag{5.12}$$

where $\hat{\sigma}$ is the standard deviation of the uncorrelated component of the data errors, and $\mathbf{C_0}$ represents correlated errors arising from the data processing (discussed later, in Section 5.4.1). The maximum-likelihood estimate for $\hat{\sigma}$ is given by

$$\hat{\sigma}^2 = \frac{1}{N-M}\left|\mathbf{R}(\hat{\mathbf{m}}) - \mathbf{R}^{\text{obs}}\right|^2, \tag{5.13}$$

where M is the number of model parameters, and $\hat{\mathbf{m}}$ is the maximum-likelihood model estimate, determined here using a hybrid optimization algorithm, which adaptively combines fast simulated annealing with the local downhill simplex method (Dosso et al., 2001).

5.3 Synthetic Studies

5.3.1 Model Design

To assess the reliability of AVO analysis in marine gas hydrate studies, synthetic test cases representative of AVO data for BSRs are considered. The model consists of a planar interface between two half spaces, with model parameters Vp_1, Vs_1, ρ_1, Vp_2, Vs_2, and ρ_2 (Figure 5.1). The interface is designed to represent the base of the GHSZ, with model parameters representative of realistic gas hydrate/free gas concentration scenarios. P- and S-wave velocities for both media are chosen based on the Helgerud (2001) gas hydrate in-frame rock-physics model (see Section 2.2.3), for given gas hydrate and free gas concentrations in the upper and lower media respectively. The rock-physics model is based on effective medium theory, and considers the gas hydrate as a component of the load-bearing sediment matrix, but without grain cementation. The model predicts the occurrence of gas hydrate to enhance both P- and S-wave velocity, but less so than would a gas hydrate cementation type model (e.g., Dvorkin and Nur, 1993). The gas hydrate in-

frame model is supported by downhole VSP data from ODP Leg 164 Hole 995 at the Blake-Bahama Ridge gas hydrate site (Helgerud, 2001). A key feature of the rock-physics model is that while *Vs* in the upper medium is sensitive to gas hydrate occurrence, it is nearly unaffected in the lower medium by the presence of free gas in the pore space because the replacement of brine with gas does not affect the sediment shear modulus (Gassmann, 1951). At higher gas concentrations, the density effect on the fluid change can significantly affect the S-wave velocity; however, this is not a concern here, with free gas concentrations on the order of 1% of the pore space. Also, the base of the GHSZ does not coincide with a lithologic boundary (e.g., Westbrook et al., 1994), so the physical parameter values derived from the rock-physics model in the upper and lower media are calculated for sediments of identical lithology. The densities chosen for the model are consistent with downhole well log measurements from ODP Leg 146 (Westbrook et al., 1994), Leg 204 (Tréhu et al., 2003), and IODP Expedition 311 (Riedel et al., 2006), and reflect the increase of density with depth due to porosity loss (~50% porosity at BSR depths) related to sediment compaction (e.g., Hamilton, 1976). Table 5.1 summarizes the physical parameters adopted for the true model for a scenario with 15% gas hydrate pore-space saturation above the BSR and 1% free gas saturation below. This model gives values for Vp_1 and Vp_2 representative of average values obtained from NMO velocity analysis in Northern Cascadia (Yuan et al., 1996).

Synthetic AVO data are generated from the true model parameters using the Zoeppritz equations (Equation 5.1), with data noise level and angular range chosen to emulate typical AVO data. Two synthetic AVO data sets for the true model are generated

	Vp (m/s)	Vs (m/s)	ρ (kg/m^3)
Upper medium	1768	421	1800
Lower medium	1481	350	1850

Table 5.1 Physical parameters adopted for the 15% gas hydrate/1% free gas model.

(Figure 5.2), which both have angular ranges of 0-80° and include random independent Gaussian-distributed errors of 0.01 and 0.05 standard deviation. These data are representative of a case with $Vp_1 > Vp_2$, giving negative reflection coefficients and no critical angle. The synthetic AVO data are inverted, using the Bayesian approach, to determine uncertainties in physical parameters and in gas hydrate and free gas concentrations. Table 5.2 summarizes all the synthetic cases considered in this section.

5.3.2 Factors for Successful AVO Inversion

To determine the most important factors affecting the uncertainty in AVO, this study begins with a scenario that provides well constrained results. The synthetic AVO curve for this scenario (referred to as case 1a) represents a best-case for data quality, in terms of angular range and data noise level. From the synthetic AVO curve, parameter estimates and uncertainties are computed using the Bayesian inversion approach, for the case of known upper medium parameters and wide uniform bounds for the lower medium (parameter bounds are summarized in Table 5.3). The resulting MPDs are shown in Figure 5.3 (case 1a), represented by histograms normalized so that the integral over the parameter bounds is unity. In this case, Vp_2, Vs_2, and ρ_2 are well constrained by the inversion. This is analogous to the successful AVO inversion for physical parameters of

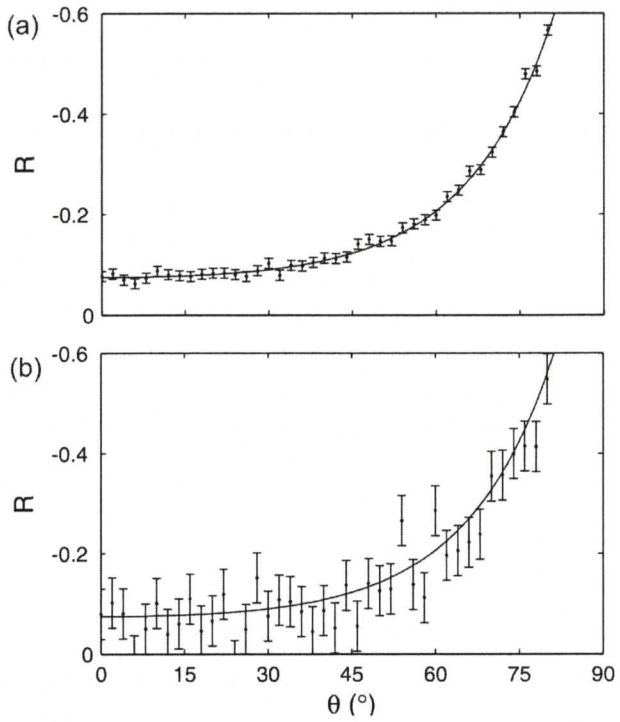

Figure 5.2 Synthetic AVO data with varying amounts of random Gaussian noise. In (a), $\sigma = 0.01$, while in (b), $\sigma = 0.05$. One-standard-deviation error bars are shown and the solid line is the error-free AVO curve. These AVO data are generated from the true model summarized in Table 5.1.

seabed sediments achieved by Riedel et al. (2003), where the upper medium is the water column, with well known physical properties.

Data of this quality and angular range are seldom available from MCS surveys, and the physical parameters of the upper medium are usually poorly known. To determine the effect of each of these factors independently, three additional synthetic cases are tested. In case 1b, the standard deviation of the errors on the synthetic data is increased from 0.01 to 0.05 (Figure 5.2b); in case 1c, the range of incidence angles is reduced from 0-80° to 0-40°; and in case 1d, physical parameters for both media are considered unknown. Cases 1a-d are summarized in Table 5.3, and inversion results are

	Model 1: Factors for successful AVO inversion	Model 2: Inversion with additional constraints
Case a	Reference model	No prior information
Case b	Increased data noise level	Density constraints
Case c	Decreased angular range	Vp – Vs relation constraints
Case d	Unknown upper parameters	P-wave velocity constraints

Table 5.2 Summary of all synthetic models considered in Section 5.3.

Parameter	Vp_1 (m/s)	Vs_1 (m/s)	ρ_1 (kg/m^3)	Vp_2 (m/s)	Vs_2 (m/s)	ρ_2 (kg/m^3)	Angular range (°)	σ data err.
True value	1768	421	1800	1481	350	1850	-	-
Case 1a	-	-	-	-	-	-	0-80	0.01
Lower bound	-	-	-	10	10	1000	-	-
Upper bound	-	-	-	3000	2000	2500	-	-
Case 1b	-	-	-	-	-	-	0-80	**0.05**
Lower bound	-	-	-	10	10	1000	-	-
Upper bound	-	-	-	3000	2000	2500	-	-
Case 1c	-	-	-	-	-	-	**0-40**	0.01
Lower bound	-	-	-	10	10	1000	-	-
Upper bound	-	-	-	3000	2000	2500	-	-
Case 1d	-	-	-	-	-	-	0-80	0.01
Lower bound	**1000**	**10**	**1000**	10	10	1000	-	-
Upper bound	**3000**	**2000**	**2500**	3000	2000	2500	-	-

Table 5.3 True model physical parameters for a 15% gas hydrate/1% free gas model, prior bounds, angular range and data quality used for cases 1a-d. The specific modification of each case from case 1a is shown in bold.

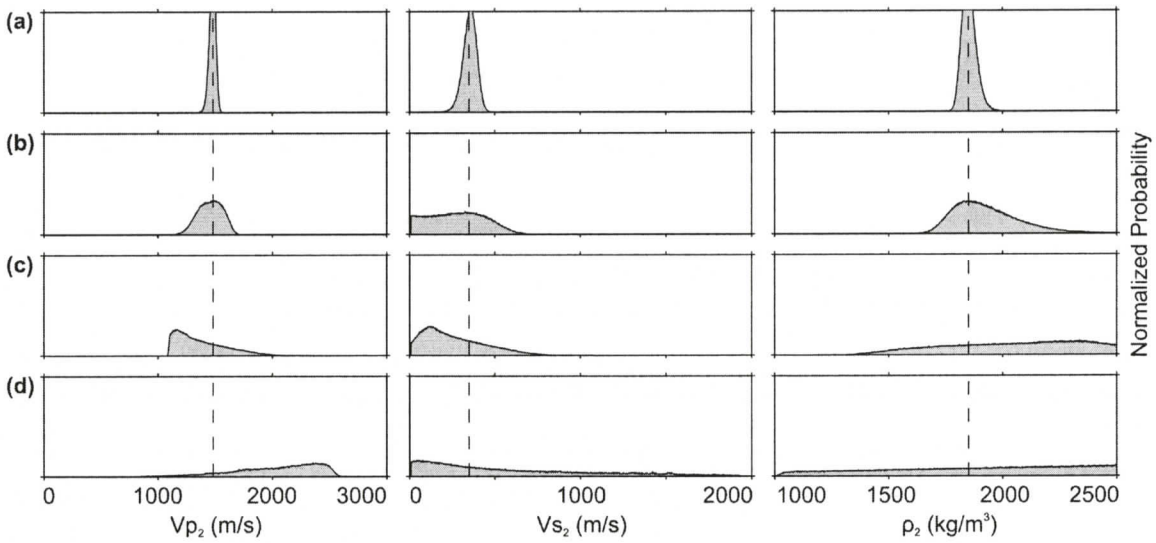

Figure 5.3 Marginal probability distributions for parameters of the lower medium from synthetic cases 1a-d, normalized so that the area of each distribution is unity. Dashed lines indicate the true parameter values. (a) Case 1a, the reference model, (b) case 1b, with σ = 0.05, (c) case 1c, with angular range of 0-40°, and (d) case 1d, with parameters of the upper medium unknown.

shown as MPDs in Figure 5.3. These distributions indicate that the factors affecting the uncertainty in inversion results are, in order of importance: (1) the number of unknown parameters, (2) the range of incidence angles, and (3) the data noise level.

The information from individual parameter MPDs can be complemented by joint parameter MPDs (Figure 5.4), which provide information on parameter correlations. In cases 1a-c, a positive correlation is observed between Vp_2 and Vs_2, while a negative correlation exists between Vp_2 and ρ_2, and between Vs_2 and ρ_2. Even though individual parameters are not well determined in all cases, the inversion does provide information on how parameters can vary with respect to each other. For example, the observed negative correlation between Vp_2 and ρ_2 exists because the data provides enough

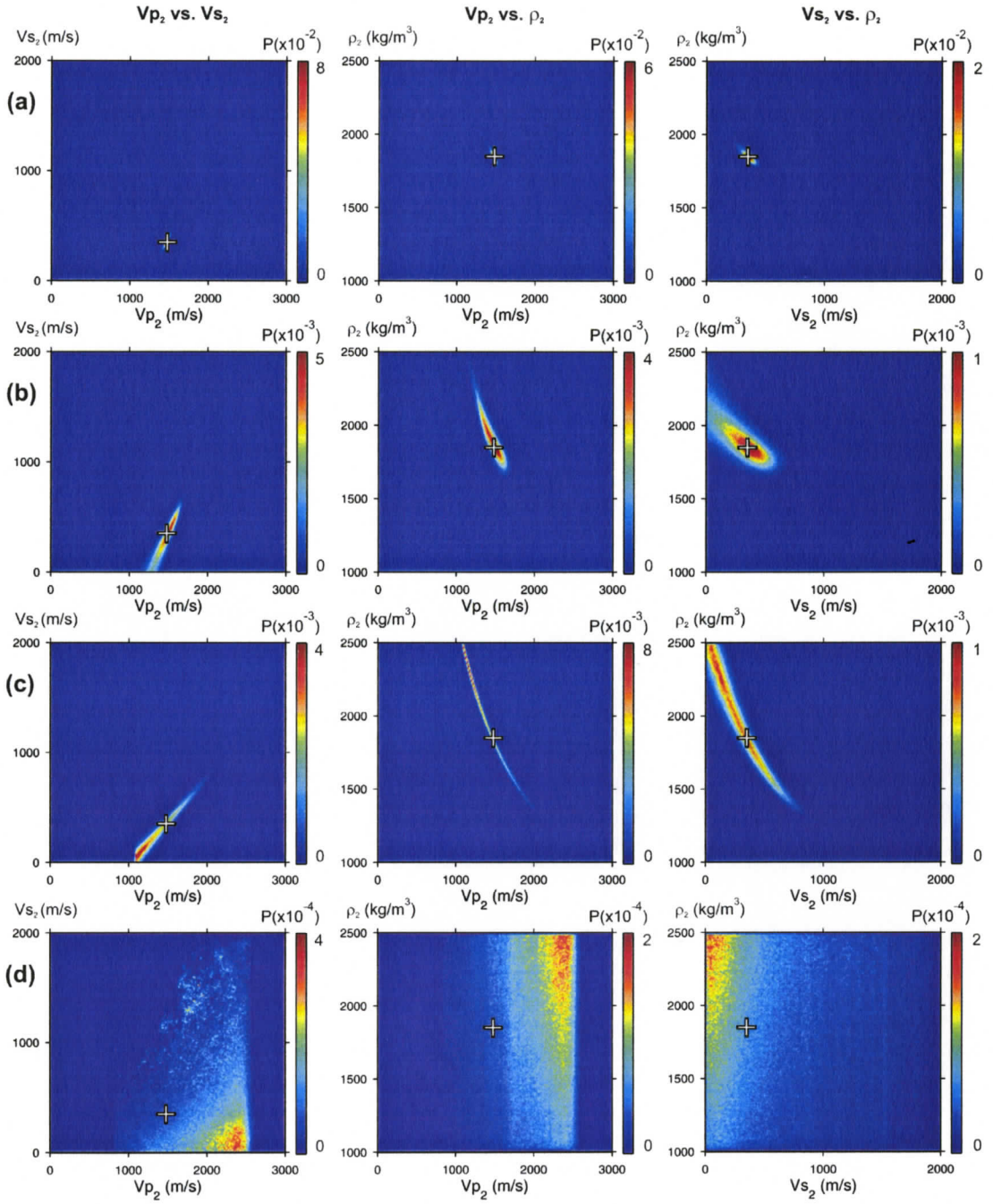

Figure 5.4 Joint marginal probability distributions of selected parameters from synthetic cases 1a-d. The colorbar scale is normalized probability (P), and the cross indicates the true parameter values. (a) Case 1a, the reference model, (b) case 1b, with $\sigma = 0.05$, (c) case 1c, with angular range of 0-40°, and (d) case 1d, with parameters of the upper medium unknown.

information to resolve P-wave impedance, but not to distinguish between contributions from density and P-wave velocity.

5.3.3 Inversion with Additional Constraints

This section considers a second set of synthetic test cases using the data from Figure 5.2a to investigate the improvement in parameter resolution that can be achieved using prior information in the form of narrow parameter bounds or specified parameter interrelationships. Re-parameterizations of the results are also applied, recognizing that the goal of this analysis is not to determine individual model parameters, but rather to determine gas hydrate and free gas concentrations. Inversion results are re-parameterized in terms of: (1) the fractional change in P-wave velocity $\Delta Vp/Vp$, (2) the fractional change in S-wave velocity $\Delta Vs/Vs$, and (3) the squared S- to P-wave velocity ratio $(Vs/Vp)^2$, where Δ represents the difference between the lower and upper media, and Vp, Vs, or ρ without a subscript indicates the mean value of the two media. For the purposes of this paper, these new parameters are referred to as "parameter combinations", and $\Delta Vp/Vp$ and $\Delta Vs/Vs$ are referred to as P- and S-wave reflectivity. This parameterization is useful for AVO analysis because it highlights relationships between the original parameters that are typically well resolved by reflection seismic data (i.e., seismic reflections provide more information about the change in physical parameters across the interface than about the parameters themselves).

In case 2a, the parameters of both media are unknown: the inversion is computed using uniform bounds on all parameters, wider than those expected for unconsolidated sediments. In case 2b, tighter prior bounds are applied to the density of both media.

Uniform prior bounds for ρ_1 and ρ_2 at the BSR are set to be 1800 ± 100 and 1850 ± 100 kg/m^3 respectively (the occurrence of gas hydrate or of free gas in relatively low concentration has little effect on bulk density). The requirement $\rho_1 \leq \rho_2$ is also imposed, forcing an increase in density with depth, related to porosity loss and sediment compaction (e.g., Hamilton, 1976). In case 2c, a further constraint is imposed in which Vs_1 is related to Vp_1 through a linear relationship, based on the gas hydrate in-frame rock-physics model given by Helgerud (2001), with deviations from this trend of no more than ± 200 m/s allowed for Vs_1

$$Vs_1 = (0.4004 Vp_1 - 292) \pm 200, \qquad (5.14)$$

a relationship that is similar to the mudrock relation of Castagna et al. (1985), within the range of expected values. Case 2d also includes constraints on P-wave velocities from a hypothetical normal moveout (NMO) velocity analysis. Uncertainties in NMO velocities are estimated by Yuan et al. (1994) to be ± 5% for carefully determined interval velocities, corresponding approximately to ± 100 m/s at BSR depths. Conservative uncertainty estimates of ± 150 m/s and ± 200 m/s for Vp_1 and Vp_2 are used here as uniform prior bounds with respect to true model values. The wider bounds for Vp_2 reflect the greater uncertainty in NMO velocities in the free gas zone beneath the BSR. MPDs and joint MPDs for the inverted physical parameters and parameter combinations of cases 2a-d are displayed in Figures 5.5-5.7, and Table 5.4 provides a summary of all cases.

5.3.4 Inversion Results

The MPDs for case 2a show that individual model parameters cannot be resolved if wide parameter bounds are used without additional prior information (Figure 5.5, case

Parameter	Vp_1 (m/s)	Vs_1 (m/s)	ρ_1 (kg/m^3)	Vp_2 (m/s)	Vs_2 (m/s)	ρ_2 (kg/m^3)
True value	1768	421	1800	1481	350	1850
Case 2a	-	-	-	-	-	-
Bounds	1000-3000	10-2000	1000-2500	10-3000	10-2000	1000-2500
Case 2b	-	-	-	-	-	-
Bounds	1000-3000	10-2000	**1800 ±100**	10-3000	10-2000	**1850 ±100**
Other	$\rho_1 \leq \rho_2$					
Case 2c	-	-	-	-	-	-
Bounds	1000-3000	10-2000	1800 ±100	10-3000	10-2000	1850 ±100
Other	**Vs_1 [m/s] = (0.4004 Vp_1 – 291.9) ± 200;** $\rho_1 \leq \rho_2$					
Case 2d	-	-	-	-	-	-
Bounds	**1768 ±150**	10-2000	1800 ±100	**1481 ±200**	10-2000	1850 ±100
Other	Vs_1 [m/s] = (0.4004 Vp_1 – 291.9) ± 200; $\rho_1 \leq \rho_2$					

Table 5.4 True model physical parameters for a 15% gas hydrate/1% free gas model and prior bounds for cases 2a-d. The constraint added to the subsequent case is shown in bold.

2a). However, joint MPDs (Figure 5.6, case 2a) show strong positive correlations between both Vp_1 and Vp_2, and Vs_1 and Vs_2 (correlation coefficients of 0.995 and 0.986). The correlation between P-wave velocities is a result of the data accurately resolving the P-wave impedance contrast. P-wave velocities (and densities) across the boundary must vary in a specific way in order to fit the AVO data. A similar argument can be made for the correlation between Vs_1 and Vs_2. These two inter-parameter correlations ($Vp_1 - Vp_2$ and $Vs_1 - Vs_2$) are tightly constrained when results are shown in terms of the parameter combinations (Figure 5.7, case 2a), and MPDs indicate that the P-wave reflectivity is well constrained, but the S-wave reflectivity is underestimated.

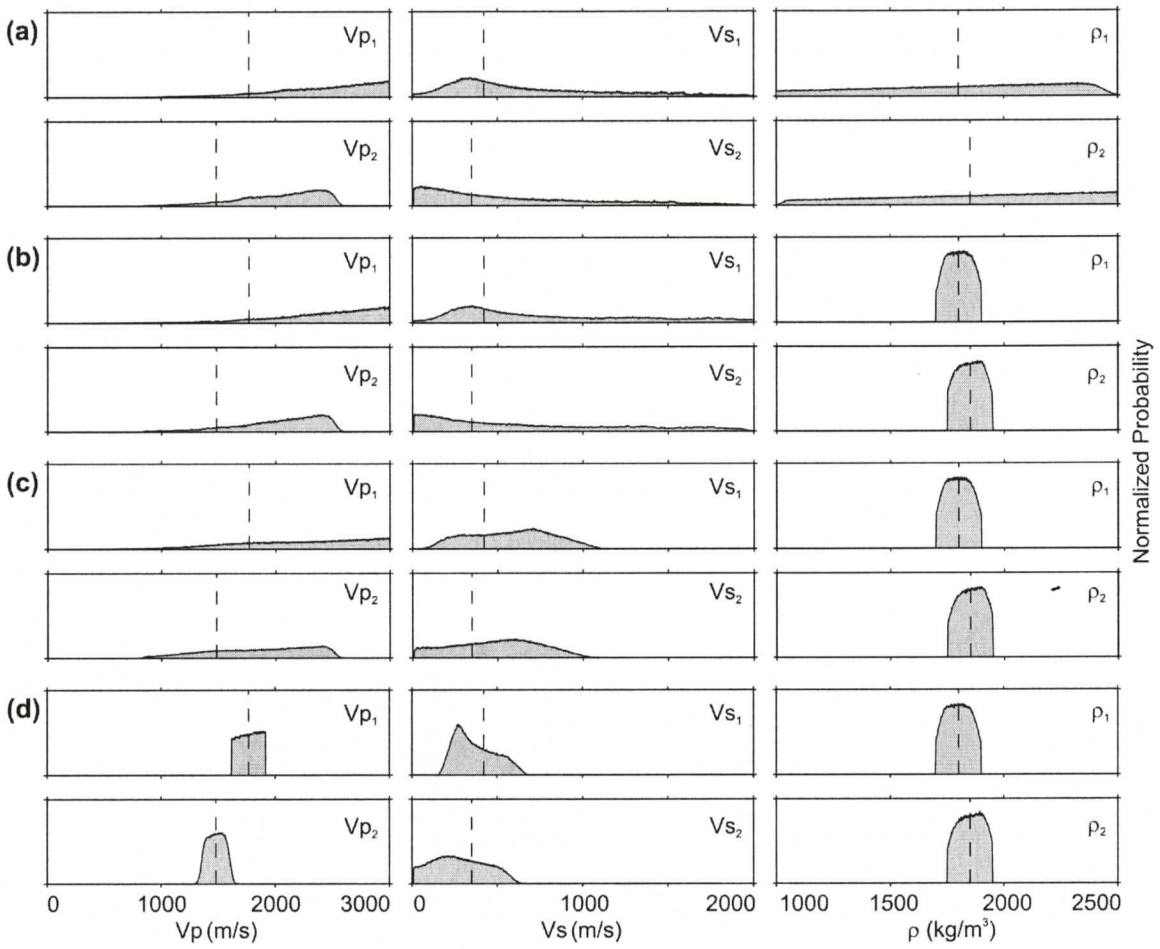

Figure 5.5 Marginal probability distributions for parameters of the upper and lower media from synthetic cases 2a-d, normalized so that the area of each distribution is unity. Dashed lines indicate the true parameter values. (a) Case 2a, with no additional prior information, (b) case 2b, with prior constraints on density, (c) case 2c, with prior constraints on density and the Vp_1 - Vs_1 relation , and (d) case 2d, with prior constraints on density, the Vp_1 - Vs_1 relation, and P-wave velocity.

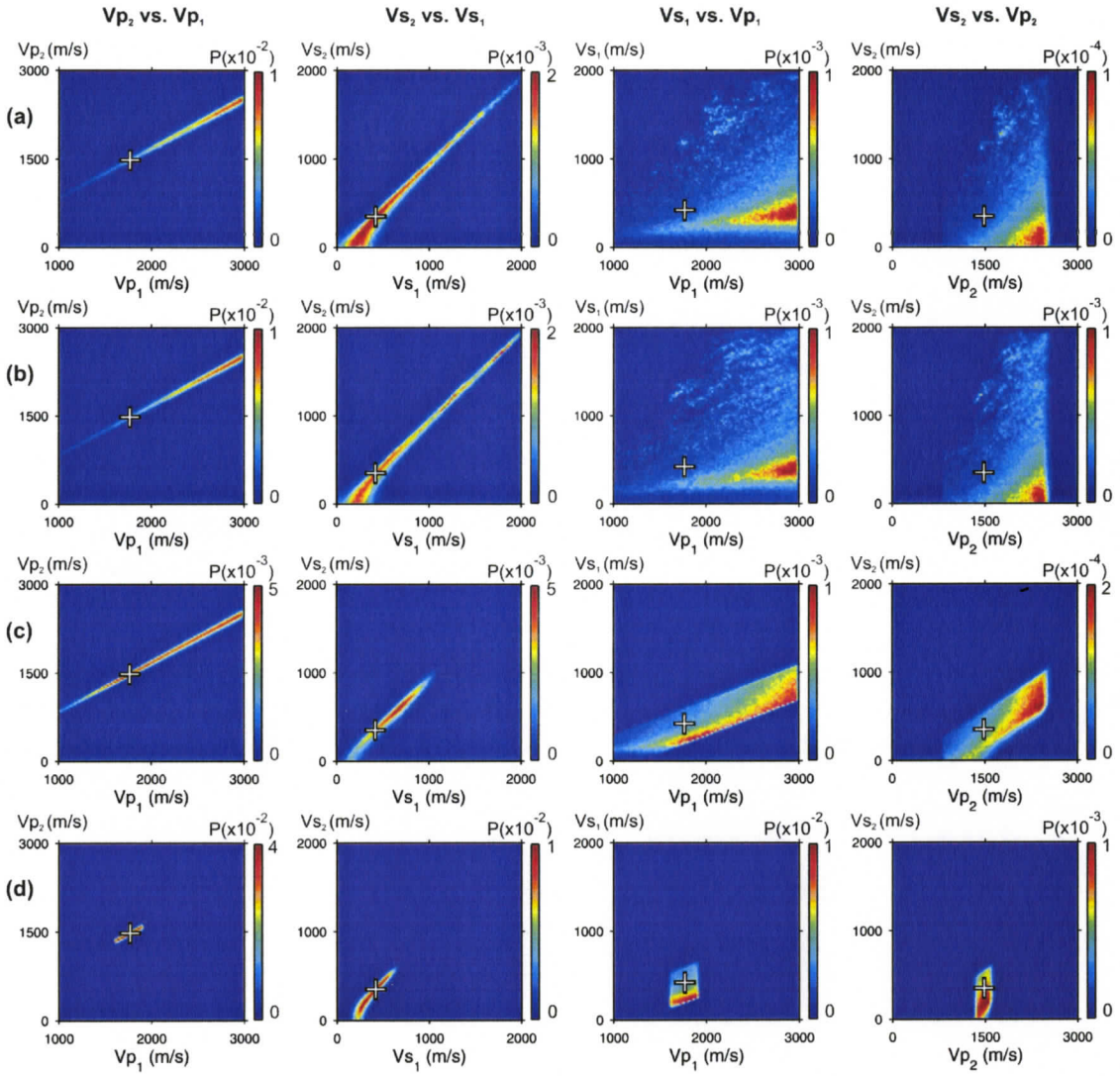

Figure 5.6 Joint marginal probability distributions of selected parameters from synthetic cases 2a-d. The colorbar scale is normalized probability (P), and the cross indicates the true parameter values. (a) Case 2a, with no additional prior information, (b) case 2b, with prior constraints on density, (c) case 2c, with prior constraints on density and the Vp_1 - Vs_1 relation , and (d) case 2d, with prior constraints on density, the Vp_1 - Vs_1 relation, and P-wave velocity.

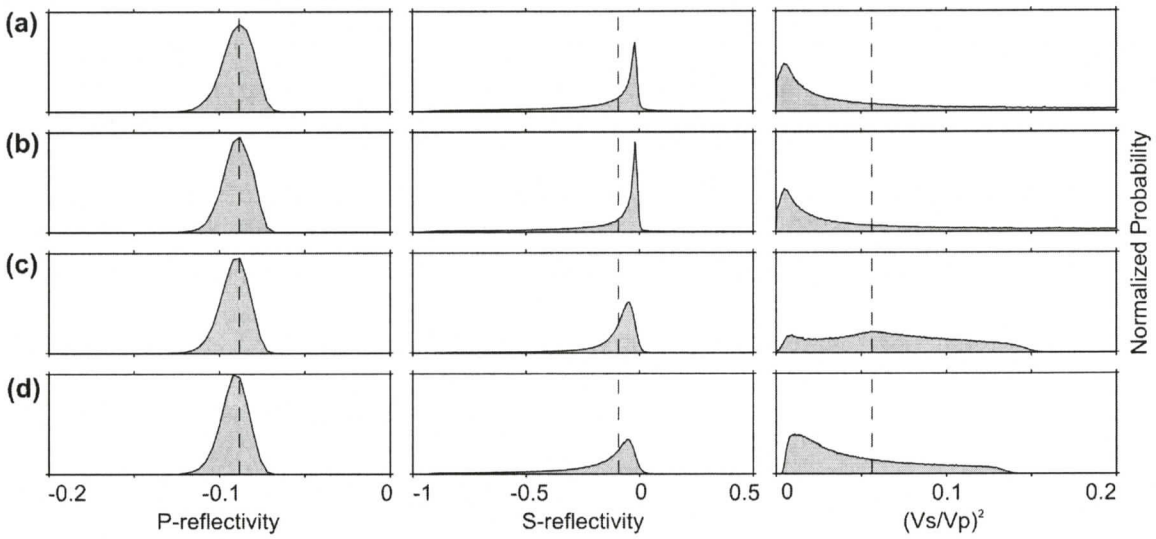

Figure 5.7 Marginal probability distributions of parameter combinations from synthetic cases 2a-d, normalized so that the area of each distribution is unity. Dashed lines indicate the true parameter values. (a) Case 2a, with no additional prior information, (b) case 2b, with prior constraints on density, (c) case 2c, with prior constraints on density and the Vp_1 - Vs_1 relation, and (d) case 2d, with prior constraints on density, the Vp_1 - Vs_1 relation , and P-wave velocity.

In case 2b, with prior density constraints, MPDs and joint MPDs of all parameters are nearly identical to those of case 2a (Figures 5.5-5.7), with the exception of density MPDs. This indicates that the additional density constraints do not provide significant information about the other parameters.

In an attempt to improve S-wave reflectivity resolution, case 2c includes a constraint which relates S-wave velocity to P-wave velocity in the upper media through Equation 5.14. MPDs of individual model parameters (Figure 5.5, case 2c) are still too wide to resolve individual parameter values, while joint MPDs (Figure 5.6, case 2c) show strong positive correlations between Vp_1 and Vp_2, and Vs_1 and Vs_2 (correlation coefficients of 0.997 and 0.977). The observed correlation between Vp_1 and Vs_1

(correlation coefficient of 0.877) is a result of the prior relationship imposed on these parameters, which in turn forces a weaker correlation between Vp_2 and Vs_2. MPDs of the parameter combinations show well constrained distributions for P- and S-wave reflectivity (Figure 5.7, case 2c), because of strong correlations between the physical parameters. The S-wave reflectivity is less well resolved than the P-wave reflectivity, but it is no longer skewed towards a value of zero. MPDs of the parameter combinations also show that $(Vs/Vp)^2$ remains poorly resolved. This demonstrates that the data provide more information about P-wave velocity contrasts than S-wave velocity contrasts, and almost no information about the relation between S- and P-wave velocities. The inversion was also tested using narrower bounds on Equation 5.14, but results were not significantly improved.

In case 2d, prior information is added to Vp_1 and Vp_2 by limiting P-wave velocity bounds, based on estimated uncertainties hypothetically obtained from NMO velocity analysis. With this prior information, Vp_1 and Vp_2 are constrained better than in previous cases, but are not further constrained by the data than by the prior, because MPDs of Vp_1 and Vp_2 are undetermined (relatively flat) within the prior bounds (Figure 5.5, case 2d). This suggests that for determining P-wave velocities, AVO is not as informative as NMO velocity analysis. For MPDs of the parameter combinations, the effect of the additional P-wave velocity constraints on the resolution of the inter-parameter relationships is negligible (Figure 5.7, case 2d).

The results clearly show the inability of the data to provide information about the $Vp - Vs$ relationship in each medium (Figure 5.6, all cases). This greatly limits the ability of AVO to independently constrain gas hydrate and free gas concentrations. In all cases,

the best resolved parameter (P-wave reflectivity) depends on Vp_1 and Vp_2, so its value does not depend uniquely on gas hydrate or free gas concentration. However, the parameter interrelationships observed in Figure 5.6 justify the choice of P-wave reflectivity, S-wave reflectivity, and $(Vs/Vp)^2$ as an appropriate re-parameterization, because they highlight the strongest correlations observed between individual parameters.

Of the four cases tested, case 2d exhibits the most tightly constrained distributions (Figure 5.7d), because it includes the most prior information. Of the individual MPDs of case 2d, S- and P-wave reflectivity are the best constrained parameters, and should therefore provide the most information on gas hydrate and free gas concentrations. A joint MPD of these parameters is shown in Figure 5.8 as a contour plot, with individual contours indicating different credibility levels. The MPD is overlain with a grid indicating S- and P-wave reflectivity values for various gas hydrate and free gas concentrations. The grid values are calculated from the gas hydrate in-frame rock-physics model (Helgerud, 2001) by forward modeling: Vp_1, Vs_1, Vp_2, and Vs_2 are calculated for different gas hydrate and free gas concentrations, which are then used to compute P- and S-reflectivity. The grid provides a means to translate inversion results, given in terms of physical parameters, into gas hydrate and free gas concentrations, via rock-physics modeling. The intersection of the grid with a given credibility level contour of the MPD provides a quantitative range of gas hydrate/free gas concentration scenarios that are consistent with the synthetic AVO data and prior. For example, both a 0% gas hydrate/3% free gas scenario, and a 25% gas hydrate/0% free gas scenario satisfy the AVO data to a 90% credibility level. The poor S-wave reflectivity resolution does not

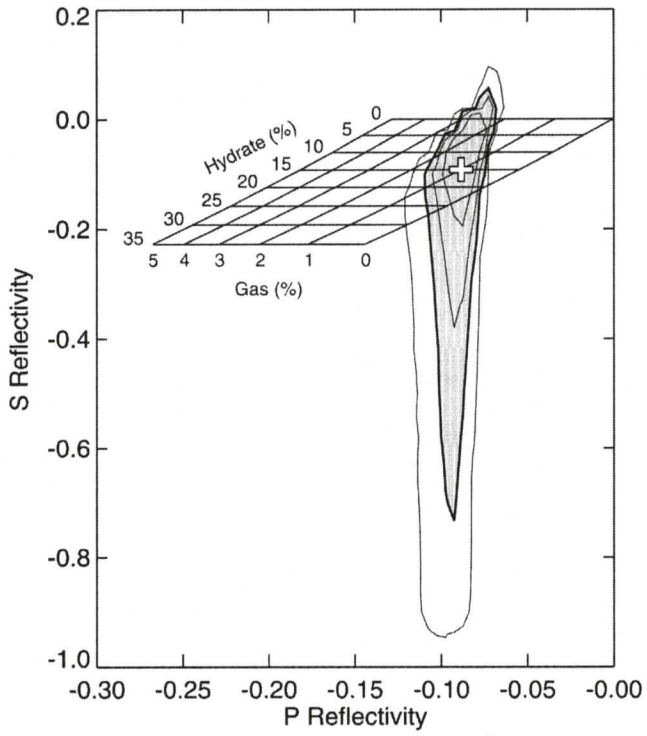

Figure 5.8 Joint marginal probability distribution of S- vs. P-wave reflectivity for synthetic case 2d, with prior constraints on density, the Vp_I - Vs_I relation, and P-wave velocity. The distribution is shown as a contour plot with the 90% credibility contour shaded in. From outermost to innermost, the contours represent 99%, 90%, 75%, and 50% credibility intervals. Contours are overlain with a grid showing where models with varying gas hydrate/free gas concentration scenarios lie in S- vs. P-wave reflectivity space. True model parameter values are indicated by the white cross. Grid nodes falling within the shaded contour represent gas hydrate/free gas concentration scenarios that could have produced these AVO data, at a 90% credibility level.

allow high gas hydrate/low free gas concentration scenarios to be distinguished from low gas hydrate/high free gas concentration scenarios.

For completeness, a case representative of an upper limit of gas hydrate and free gas concentration was also tested: inversion of synthetic AVO data for a true model with 25% gas hydrate and 2% free gas yielded similarly poorly constrained results.

5.4 Inversion of Northern Cascadia Data

5.4.1 Data and Processing

This section considers AVO data from a MCS line in Northern Cascadia, offshore Vancouver Island. The seismic data is presented and discussed by Spence et al. (1991a and b). The location chosen for the AVO inversion is on the mid-continental slope, where a prominent BSR is present. Because the MCS line (line 89-08) is in the dip direction, a location with relatively flat topography and apparent horizontal subsurface structure is chosen to avoid complications due to dipping reflectors. The location is close to ODP Site 889/890 (Leg 146) and IODP Site U1327 (Expedition 311), where the base of the GHSZ occurs at a depth of 225 m (Westbrook et al., 1994; Riedel et al., 2006), and reliable P-wave velocity and density information are available from well logs. Figure 5.9 shows a stacked section of the area of interest and the super-CDP gather used in the inversion.

The MCS survey provided amplitude data as a function of source-receiver offset (acquisition parameters summarized in Section 4.1.3). For quantitative AVO analysis, BSR reflection coefficients as a function of BSR incidence angles are required. True BSR incidence angles were obtained from source-receiver offsets by ray tracing through a 1-D

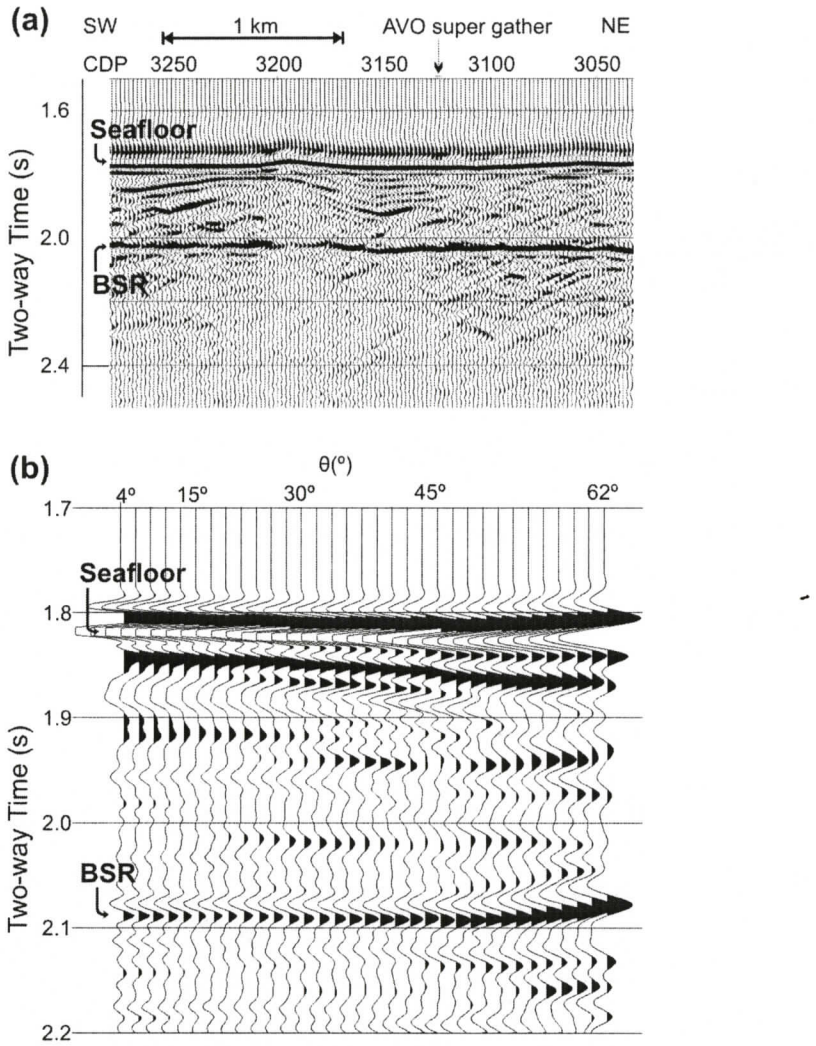

Figure 5.9 (a) Stacked seismic section of the area of interest, near IODP Site U1327, and (b) super CDP gather of traces used in the inversion, where θ is the BSR incidence angle.

velocity model derived from semblance velocity analysis: at the maximum offset of 3783 m, in water depth of 1300 m, the incidence angle at the seafloor was 49°, and increased to 67° at the BSR (225 m below the seafloor), due to increasing velocity with depth. The calculation of angle-dependent reflection coefficients required a true-amplitude data processing scheme (e.g., Duren, 1991). The processing is divided into time- and offset-dependent corrections. The time-dependent corrections to be considered are for geometric

spreading and attenuation. Simplified geometric spreading corrections were obtained by multiplying arrival amplitudes by their arrival traveltimes; since the BSR is at such a shallow depth below the seafloor, this correction is a good approximation for the BSR as well as the seafloor reflection. Because of the shallow depth of the BSR and the short travel path through sediment, corrections for attenuation are considered unnecessary, given attenuation estimates in marine gas hydrate-bearing sediments (Wood et al., 2000). For offset dependent corrections, previous work on this MCS survey (e.g., Hyndman and Spence, 1992; Yuan et al., 1999) used corrections for source and receiver directivity based on hydrophone array attenuation as a function of incidence angle (Sheriff and Geldart, 1982), and source waveform as a function of outgoing angle provided by Digicon Geophysical Corporation. Because of the difficulty in quantifying the uncertainty in these corrections (especially the source waveform function), the alternate approach taken here is to account for all offset-dependent corrections by calibration of the measured seafloor AVO to the seafloor AVO expected for a realistic model of the seafloor, based on ODP drilling results (Westbrook et al., 1994; Expedition 311 Scientist, 2005) and seismic NMO analyses (e.g., see Andreassen et al., 1995, who used the same method). This is an empirical approach to derive a pooled offset-dependent correction that essentially combines all of the uncertainties due to source/receiver directivity and variable seafloor characteristics via trace normalization. However, rather than utilizing a single value for each of the seafloor physical parameters, the method is extended by using a range of values to quantify the uncertainty of the pooled offset-dependent correction. A Monte Carlo simulation is carried out, where a large sample of expected seafloor AVO curves are generated from the Zoeppritz equations (Equation 5.1), by randomly choosing

seabed parameters from Gaussian probability distributions representing the best estimates of the expected value and standard deviation for Vp_{sf}, Vs_{sf} and ρ_{sf} of 1570 ± 20 m/s, 170 ± 40 m/s, and 1760 ± 50 kg/m^3 respectively. Fixed values of 1460 m/s and 1020 kg/m^3 are used for seawater velocity and density. Each seafloor AVO curve R_{sf} of the Monte Carlo sample is used to compute a BSR AVO curve R_{bsr}, which accounts for offset-dependent corrections, given expected seafloor AVO for that particular trial of the Monte Carlo simulation:

$$R_{bsr} = \frac{A_{bsr}}{A_{sf}} R_{sf} \left(1 - R_{sf}^2\right)^{-1}, \tag{5.15}$$

where A_{sf} and A_{bsr} are seafloor and BSR amplitudes after time-dependent corrections, chosen as the peak signal level for a given reflection, measured prior to NMO, and averaged at each angle (offset) over 4 adjacent CDPs to improve the signal-to-noise ratio. After time-dependent corrections, the ratio A_{bsr}/A_{sf} remains fixed at a given angle, so the offset-dependent corrections are achieved in Equation 5.15 by scaling the amplitude ratio in a given trace by a factor of $R_{sf}\left(1 - R_{sf}^2\right)^{-1}$, where R_{sf} depends on the realization of the Monte Carlo simulation. The factor $\left(1 - R_{sf}^2\right)^{-1}$ accounts for transmission loss at the seafloor (Yuan et al., 1999).

The BSR AVO data used in the inversion (Figure 5.10a) are calculated, at each trace, as the sample mean of R_{bsr} over the Monte Carlo simulation, for that trace. The sample of R_{bsr} data are then used to compute a covariance matrix representing the uncertainty in directivity corrections

$$\mathbf{C}_0 = \left\langle \left(\mathbf{r} - \langle \mathbf{r} \rangle\right)\left(\mathbf{r} - \langle \mathbf{r} \rangle\right)^T \right\rangle, \tag{5.16}$$

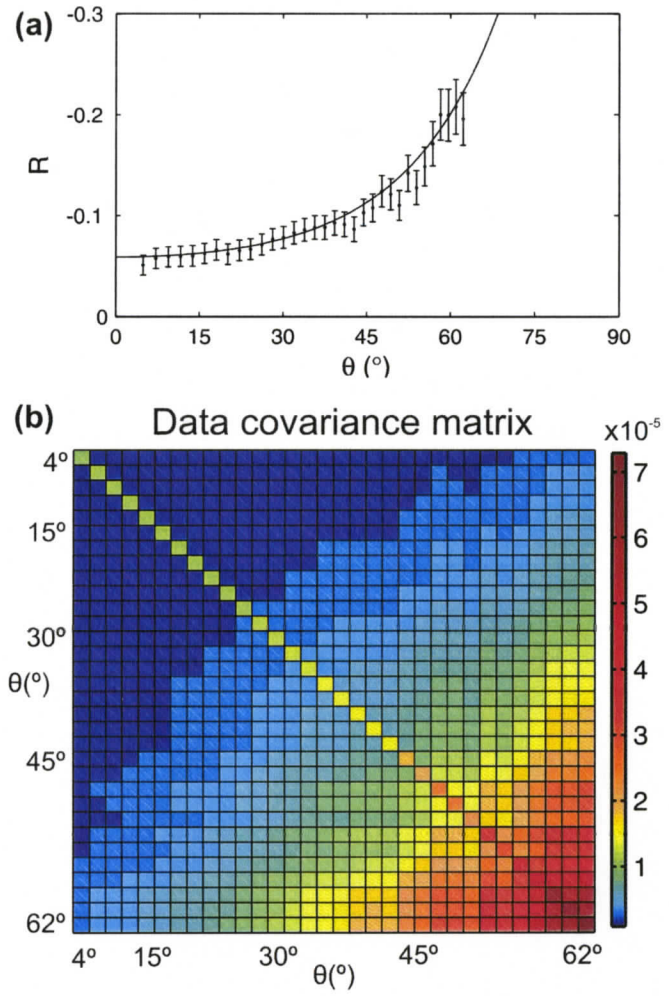

Figure 5.10 (a) BSR AVO data from MCS line 89-08, CDPs 3123-1326, near IODP Site U1327. Reflection coefficients are derived from true-amplitude processed data, and angles are BSR incidence angles obtained from ray tracing. One-standard-deviation error bars are the square root of the corresponding diagonal element of the data covariance matrix. The solid line is the predicted AVO for maximum-likelihood model parameter estimates. (b) Data covariance matrix including both correlated and random error components. Rows and columns of matrix correspond to the AVO data points shown in (a). The colorbar scale is the covariance of reflection coefficients.

where $\mathbf{r}$ is a vector of the BSR AVO data R_{bsr} for a given realization of the Monte Carlo simulation.

The complete data covariance matrix $\mathbf{C_D}$, which considers both measurement errors and uncertainties in the directivity correction, is obtained via Equation 5.12, and is shown in Figure 5.10b. The independent, identically-distributed component of the error $\hat{\sigma}^2$ (related to random noise) is calculated from Equation 5.13, with $\hat{\mathbf{m}}$ obtained by minimizing the negative log likelihood function over $\mathbf{m}$ via adaptive simplex simulated annealing (Dosso et al., 2001). The covariance matrix $\mathbf{C_D}$ is then used in the Gibbs' sampling procedure of the Bayesian inversion.

5.4.2 Inversion Results

To invert the processed AVO data, all the prior information used in case 2d is applied. Constraints on the density and the Vp_1 - Vs_1 relationship are used, and uniform prior bounds for Vp_1 and Vp_2 are chosen based on NMO velocities for the upper and lower medium, estimated at 1795 ± 150 m/s and 1494 ± 200 m/s respectively. Inversion results (Figure 5.11) are slightly less well constrained than for synthetic case 2d, which is explained by the narrower angular range in the measured data. Inversion results obtained without accounting for uncertainty in the seafloor AVO gave a slightly more negative P-wave reflectivity estimate (an average difference of -0.03), and had little effect on S-wave reflectivity results. Although the true answer, of course, is unknown, the use of a full data covariance matrix represents a more realistic treatment of data uncertainties.

As in case 2d, the only parameters that are not well constrained from prior information are Vs_1 and Vs_2, but individual parameter MPDs (Figure 5.11a) show that the data do not usefully constrain them. Even though the MPD of Vs_1 peaks at 385 m/s (10%

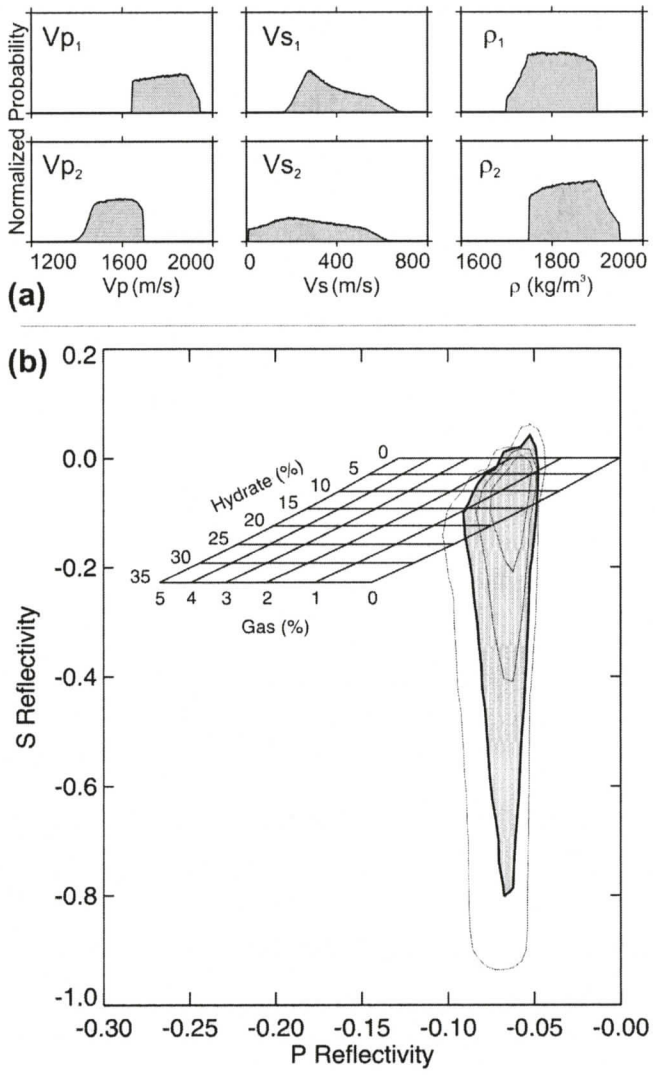

Figure 5.11 Parameter marginal probability distributions (MPDs) of inverted AVO data. (a) MPDs of individual parameters. (b) Joint MPD of S- vs. P-wave reflectivity shown as a contour plot with the 90% credibility contour shaded in. From outermost to innermost, the contours represent 99%, 90%, 75%, and 50% credibility intervals. Contours are overlain with a grid showing where models with varying gas hydrate/free gas concentration scenarios lie in S- vs. P-wave reflectivity space. Grid nodes falling within the shaded contour represent gas hydrate/free gas concentration scenarios that could have produced these AVO data, at a 90% credibility level.

gas hydrate concentration based on the rock-physics model), the 90% credibility interval for Vs_1 calculated from the MPD is 300-520 m/s (0-30% gas hydrate concentration). The limited S-wave velocity information is also apparent in the joint MPD of S- vs. P-wave reflectivity (Figure 5.11b), where the S-wave reflectivity is particularly poorly constrained. The intersection of the joint MPD of S- vs. P-wave reflectivity with the grid of gas hydrate and free gas concentrations provides a quantitative estimate of the range of scenarios that satisfy the AVO data: the contour plot indicates that at a 90% credibility level, that gas hydrate and free gas concentrations immediately above and below the BSR are only constrained to be 0-23% and 0-2%, respectively. The measured negative reflection coefficients of course require that there be either some amount of gas hydrate or free gas.

To understand why AVO does not provide adequate constraints on gas hydrate and free gas concentrations, the relationships between P- and S-wave reflectivity, and gas hydrate and free gas concentrations must be examined in more detail. Figure 5.11b shows that the P-wave reflectivity is well constrained by the inversion (between -0.09 and -0.05, at a 90% credibility level). However, even if it were perfectly constrained, it would not provide a unique solution for gas hydrate or free gas concentration. For example, at a P-reflectivity of -0.10, the gas hydrate concentration can range from 0% to 25%, and free gas, from 0% to 3%. This is because the P-reflectivity is a measure of change in P-wave velocity across the BSR, which can be due to either gas hydrate above, or free gas below, or (most likely) some combination of the two (note that the 0% free gas case can be excluded if VSP, sonic log, or NMO velocities shows clear P-wave velocity reduction relative to the no-gas reference velocity below the BSR). Furthermore, the constraints on

P-reflectivity obtained from the AVO inversion could have simply been determined from the near offset reflection coefficients, without the use of AVO.

Because the S-wave velocity in the lower medium does not change significantly with varying free gas concentration, the S-wave reflectivity is insensitive to free gas occurrence: the grid in Figure 5.11b shows that if the free gas concentration is varied while holding gas hydrate concentration fixed, S-wave reflectivity remains constant. A unique dependence of S-wave reflectivity on gas hydrate concentration is therefore implied by the rock-physics model (at fixed porosity and mineralogy). The grid in Figure 5.11b shows that an increase in gas hydrate concentration of 5% will cause a decrease in S-wave reflectivity of ~0.03, illustrating that good S-wave reflectivity resolution would provide valuable constraints on gas hydrate concentration. However, Figure 5.11b clearly shows that the AVO data do not provide nearly enough S-wave reflectivity resolution to constrain gas hydrate concentration. Because the data do not usefully constrain S-wave velocity or S-wave reflectivity, the analysis shows that the AVO method in gas hydrate studies provides no additional information to the analysis of near offset reflection coefficients or NMO velocity analysis in determining gas hydrate and free gas concentrations.

5.5 Ostrander Gas Sand Model

The poor constraint provided by AVO in gas hydrate BSR studies prompts the question of the usefulness of this tool for other geophysical problems, such as those pertaining to oil and gas. To address this question, the Bayesian AVO inversion is applied to reflections from the top of the sand layer in the now classic Ostrander (1984)

Parameter	Vp_1 (m/s)	Vs_1 (m/s)	ρ_1 (kg/m^3)	Vp_2 (m/s)	Vs_2 (m/s)	ρ_2 (kg/m^3)
True value	3048	1244	2400	2438	1626	2140
Bounds	10-5000	10-3000	2400 ±100	10-5000	10-3000	2140 ±100
Other	Vs_1 [m/s] = (0.862 Vp_1 – 1172) ± 400					

Table 5.5 True model physical parameters for Ostrander's (1984) gas sand model and prior bounds for the inversion.

gas sand model (a low velocity gas-charged sandstone layer between high velocity shale layers). Physical parameters for each layer given by Ostrander (1984) are summarized in Table 5.5. A major difference between Ostrander's gas sand model and the gas hydrate models is that the gas sand model represents consolidated sediments, with greater values for Vp, Vs and ρ. As in the gas hydrate case, gas in the sand unit reduces Vp. However, the upper unit in Ostrander's model has reduced Vs, representative of typical shale beds. Probabilistic AVO inversion is commonly used in oil and gas type problems (e.g., Drufuca and Mazzotti, 1995; Avseth et al., 2001; Buland and Omre, 2003; Mazzotti and Zamboni, 2003; Hampson et al., 2004) to provide quantitative estimates of lithology, porosity, and/or pore-space saturation. The purpose of this part of the study is to compare the applicability of AVO in gas hydrate BSRs to gas sand reflections, by determining how well AVO can detect the presence of gas in the sand unit.

Synthetic AVO data generated from Ostrander's model using the Zoeppritz equations are shown in Figure 5.12. The angular range is 0-80°, and Gaussian-distributed random errors with standard deviation of 0.01 are included. The synthetic AVO data are inverted using the same Bayesian approach. Prior information used is that the densities of

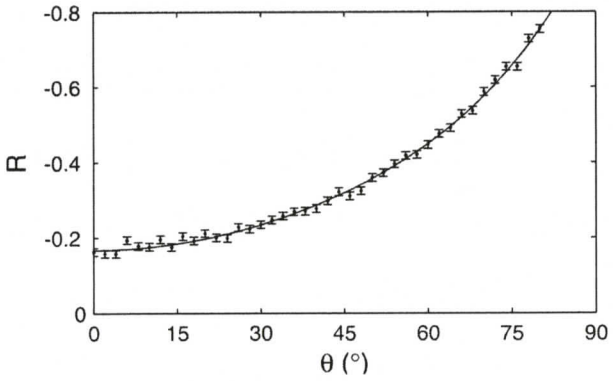

Figure 5.12 Synthetic AVO data generated from reflections off the top of the Ostrander gas sand. Random Gaussian noise with $\sigma = 0.01$ is added to the data. One-standard-deviation error bars are shown and the solid line is the error-free AVO curve.

both media are constrained by well log data, and that Vp_1 and Vs_1 (in the shale) are related by Castagna et al.'s (1985) mudrock relation. This equation is reordered so as to accept a reasonable range of Vs_1 values for a given Vp_1

$$Vs_1 = (0.862Vp_1 - 1172) \pm 400. \tag{5.17}$$

True model parameters and prior constraints are summarized in Table 5.5.

Inversion results are shown as joint MPDs of model parameters in Figure 5.13. Of interest is the observed correlation between Vp_2 and Vs_2 (Figure 5.13d), because the relationship between these parameters is affected by the presence of gas. Castagna et al. (1985) showed that water-saturated sandstones and shales plot along the mudrock line in $Vp - Vs$ space. Smith and Gidlow (1987), and Fatti et al. (1994) further showed that gas-charged sandstones plot away from the mudrock line, with reduced Vp for a given Vs. Physically, this occurs because the presence of gas in the sand acts to reduce P-wave velocities, while having little or no effect on S-wave velocities (e.g., Gregory, 1976).

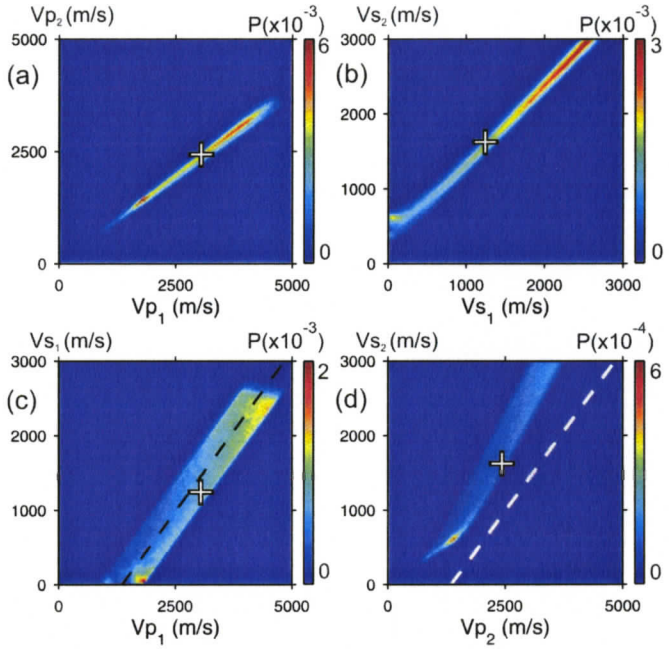

Figure 5.13 Joint marginal probability distributions of selected parameters from Ostrander's gas sand model. The colorbar scale is normalized probability (P), and the crosses indicate true parameter values. (a) shows Vp_2 vs. Vp_1, (b) shows Vs_2 vs. Vs_1, (c) shows Vs_1 vs. Vp_1 (in the shale), and (d) shows Vs_2 vs. Vp_2 (in the gas sand). In (c) and (d), the dashed line is the mudrock line, indicating the expected Vp - Vs trend for shales and water-saturated sandstones.

This effect is clearly observed in the joint MPD of Vs_2 vs. Vp_2 (Figure 5.13d), as the distribution occurs away from the mudrock line, qualitatively indicating that the sand is gas-charged. For quantitative estimates and uncertainties of formation parameters such as porosity, an appropriate rock-physics model is needed (e.g., Gassmann, 1951).

The successful application of the AVO inversion scheme to Ostrander's gas sand model and its failure for gas hydrate BSRs demonstrates that the usefulness of AVO is dependent on the physical properties of the material in question. AVO inversion for the

gas sand model resolves a relationship between Vp_2 and Vs_2 which allows gas-saturated sandstones to be distinguished from wet sandstones.

5.6 Discussion

This chapter examined the applicability of AVO in determining gas hydrate and free gas concentrations above and below a BSR interface. The synthetic AVO analysis for gas hydrate BSRs indicate that it is generally not possible to resolve all physical parameters (Vp_1, Vs_1, ρ_1, Vp_2, Vs_2, and ρ_2) at the BSR interface using MCS data. The study suggested that the most important factors affecting the AVO uncertainty are prior knowledge of the properties of the upper media and the angular range of the data.

Useful constraints on gas hydrate and free gas concentrations at the BSR interface do not require all parameters be individually constrained; information about inter-parameter relationships can be diagnostic. The inversion shows that P-wave reflectivity is the best resolved parameter, followed by S-wave reflectivity, with little information about the $Vp - Vs$ relationship. From a physical point of view, parameters such as P- and S-wave reflectivity (which depend on properties of both media) are best resolved because of the nature of the data: measured seismic reflections occur because of changes in physical properties across an impedance boundary. The lack of information content of the data with respect to the $Vp - Vs$ relationship in either medium greatly limits independent determination of gas hydrate and free gas concentrations.

A further source of uncertainty is the adequacy of the model in representing the base of the GHSZ. By analyzing BSR reflection coefficients as a function of frequency, Chapman et al. (2002) showed that the base of the GHSZ corresponds to a gradational change from sediments containing gas hydrate to sediments containing free gas.

However, the half-space/half-space model used here is probably an adequate representation of the BSR when considering low-frequency seismic data.

Inversion of AVO data from offshore Vancouver Island, Canada, is interpreted as a joint marginal probability distribution (MPD) of P- and S-wave reflectivity, overlain with a grid of P- and S-wave reflectivity values for different gas hydrate/free gas concentration scenarios, determined from a rock-physics model. This approach provides a means to interpret parameter MPDs in terms gas hydrate and free gas concentration estimates. At a 90% credibility level, gas hydrate and free gas concentrations at the study location are poorly constrained, i.e., 0-23% and 0-2% immediately above and below the BSR. Furthermore, synthetic cases that used larger angular ranges and included smaller data errors gave a similar degree of constraint, demonstrating that an improvement in data quality or angular range does not significantly improve the results.

The joint MPD of P- and S-wave reflectivity shows the range of gas hydrate/free gas concentration scenarios that satisfy both the data and prior. The distribution is poorly constrained because of poor S-wave reflectivity resolution, which can be understood by examining the rock-physics model: according to the gas hydrate in-frame model used, where gas hydrate occurs as a load-bearing component of the sediment matrix, *Vs* for a medium with 15% gas hydrate concentration is 421 m/s, while *Vs* for a medium with 1% free gas is 350 m/s, a change of only 71 m/s. This degree of resolution cannot be expected from marine MCS data, where only P-waves are measured directly, and *Vs* information is obtained indirectly through *Vp* information and AVO, since uncertainties in *Vp* are estimated to be at least ± 100 m/s. As for P-wave velocity and density information, the inversion does not constrain their values any more than the prior

information, indicating that AVO is not a useful way to obtain information about these parameters. The most reliable method to obtain P-wave velocity information is NMO velocity analysis, whereas BSR P-wave reflectivity information is most easily obtained from near-vertical incidence BSR reflection coefficients.

The lack of success of AVO in this and other gas hydrate studies can be attributed to the fact that the BSR represents only a relatively small contrast in physical properties, and that BSRs studied here occur in unconsolidated sediments of ~50% porosity, with low S-wave velocities. Fundamentally, AVO is an indirect method of obtaining S-wave information, which is not sensitive enough to be useful in unconsolidated sediments. An alternative approach is the use of ocean-bottom receivers that directly measure the shear wavefield via P-S mode-converted waves (e.g., Stewart et al., 2002; Andreassen et al., 2003).

AVO inversion of synthetic data generated from Ostrander's gas sand model shows that the success of AVO is dependent on the properties of the sediment sections. In this case, inversion results show a strong relationship between S- and P-wave velocities in the sandstone unit, with values of these parameters diagnostically indicative of gas-charged sandstones. The improvement in inversion resolution for the gas sand case over the gas hydrate cases is attributed to the fact that in the gas sand case, (1) the formations are consolidated sediments with greater P- and S-wave velocities, allowing the relationship between *Vp* and *Vs* to be further constrained; (2) the contrast in physical properties at the boundary is greater, because it is a lithologic boundary (as opposed to a change in pore space saturation, as in the gas hydrate case), leading to a more diagnostic AVO curve and more resolvable P- and S-wave velocity contrasts; and (3) because in

Ostrander's model, where only properties of the sandstone unit are sought, the problem has less degrees of freedom than the gas hydrate case, where both gas hydrate and free gas concentrations are unknown. The success of the AVO inversion applied to the gas sand case suggests that AVO could potentially be a valuable method in areas where gas hydrate occurrence is controlled by lithologic variations on a seismic scale, such as thick, coarse-grained, gas hydrate-bearing units in the marine or permafrost setting. To properly assess this potential synthetic tests representative of these settings must first be undertaken.

The variable degree of success obtained in this AVO study highlights the need to include rigorous quantitative uncertainties in all AVO studies. The appeal of the Bayesian approach to inverting AVO data is that the results are accompanied by realistic quantitative error estimates, allowing the interpreter to accurately gauge the reliability of results.

Chapter 6

Discussion, Summary and Conclusions

6.1 Comparison of Results: Resistivity, Velocity, and AVO

6.1.1 Gas Hydrate Saturation Estimates

Well log, core, and VSP data collected during IODP Expedition 311, and MCS NMO velocities were used to obtain gas hydrate saturation estimates from electrical resistivity and seismic velocity measurements at the locations of the well transect. Figure 6.1 shows gas hydrate saturation estimates from the resistivity- and velocity-based analyses. The resistivity-based results shown are those calculated from the log density porosity, and the velocity-based results are those calculated by effective porosity reduction, using an empirical porosity-velocity relation established from smoothed MCS velocity and log porosity trends. In both cases gas hydrate saturation estimates are in reasonably good agreement with results from equivalent field experiments (MCS velocity-based estimates calculated in this study, and CSEM-based Archie analysis of Yuan and Edwards, 2000). In this study, results based on velocity measurements generally give higher gas hydrate saturation estimates than those calculated here from downhole resistivity logs, most notably at U1327, in the interval 140-220 m, and at

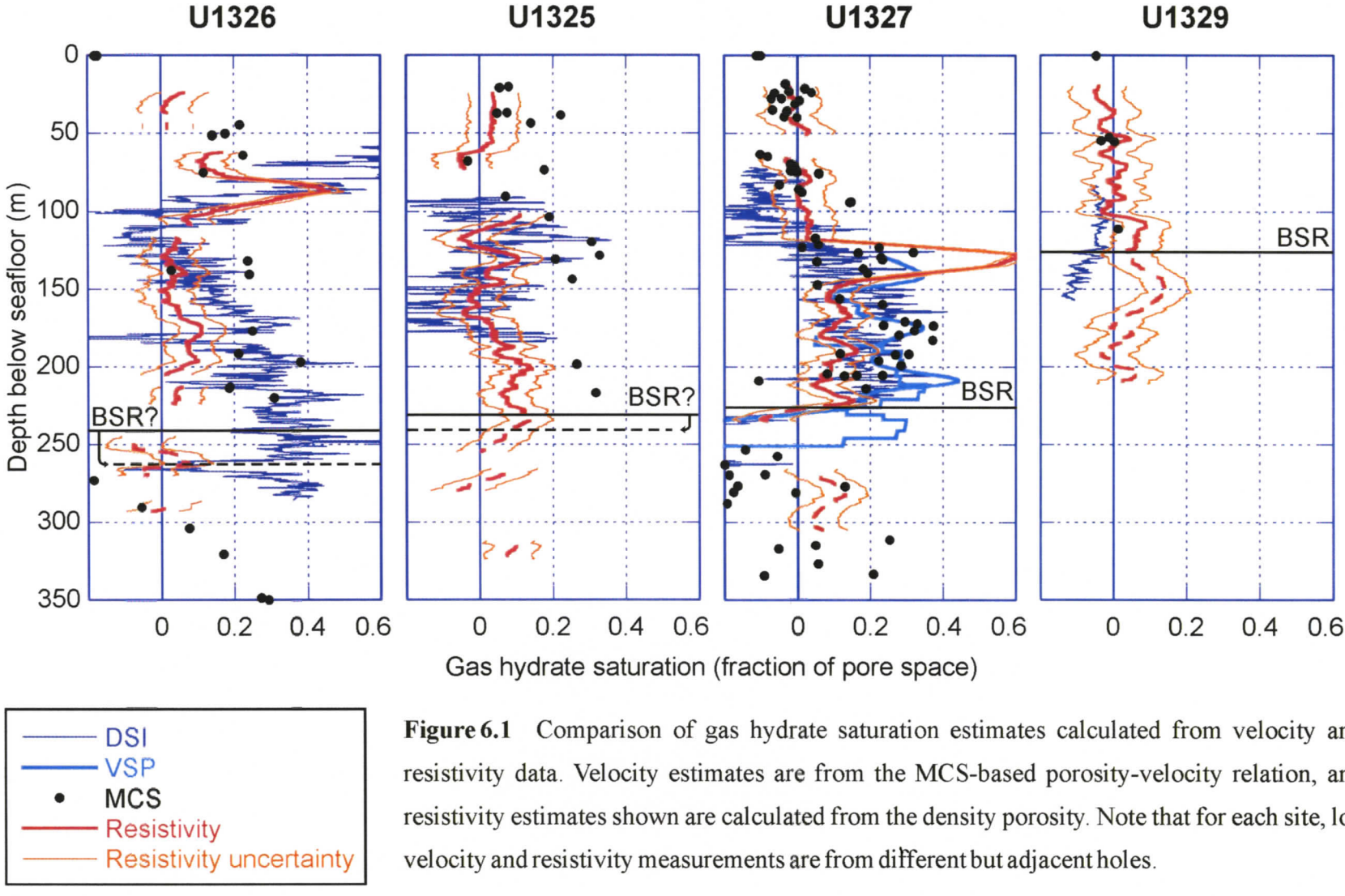

Figure 6.1 Comparison of gas hydrate saturation estimates calculated from velocity and resistivity data. Velocity estimates are from the MCS-based porosity-velocity relation, and resistivity estimates shown are calculated from the density porosity. Note that for each site, log velocity and resistivity measurements are from different but adjacent holes.

U1326 in the interval 150-240 m. Note that in the latter case, gas hydrate saturations from effective porosity reduction are probably overestimates, since the regional MCS no-hydrate reference velocity is most likely lower than the local no-hydrate reference, because porosities at this site are unusually low. However, gas hydrate saturation estimates from the gas hydrate in-frame rock-physics model in the same interval (~20% of the pore space) are also greater than resistivity-based estimates. The concentrated gas hydrate zone in U1326 in the interval 60-90 m is resolved by both resistivity and velocity measurements, whereas the concentrated gas hydrate zone in U1327, in the interval 120-138 m, is only observed in resistivity, a discrepancy attributed to inter-hole variability (Riedel et al., 2006). Both resistivity and velocity data indicate only a minimal amount of gas hydrate present at Site U1329 and in the upper portion of Sites U1325 and U1327.

The AVO study indicates that gas hydrate saturation is 0-23% of the pore space, in the interval immediately above the BSR, near Site U1327. Immediately below the BSR, free gas saturation is 0-2% of the pore space. However, results from the AVO analysis could have been more easily obtained from vertical incidence reflection coefficients and NMO velocity analysis. This leads to the conclusion that AVO analysis of BSRs is not a useful tool to estimate associated gas hydrate and free gas concentrations.

6.1.2 Uncertainties

The uncertainties in gas hydrate saturation estimates from resistivity and velocity measurements are primarily related to uncertainties in (1) the measurements themselves, (2) the estimated no-hydrate reference, and (3) the relation between velocity/resistivity and gas hydrate saturation.

Log resistivity measurements are generally of better quality than the log velocity measurements, because they do not rely as heavily on a good contact between the logging tool and the borehole wall. With no caliper log in the WL holes, it is difficult to identify the zones of poor velocity measurements. Also, since the sonic log is recorded by a WL tool, the measurement is made well after the hole is drilled, potentially disrupting in situ conditions. With cold seawater circulating through the well, it is possible that an annulus of gas hydrate could have formed around the borehole, which would not have been present in situ (Hyndman et al., 2001; Riedel et al., 2005). The resistivity data, measured while drilling, provide information that is more representative of in situ conditions. However, credibility is brought to the log velocity measurements, since they are generally in agreement with MCS and VSP velocities. Another aspect is that resistivity measurements can be obtained at higher resolution than velocity measurements: the LWD resistivity has a vertical resolution of 0.05-0.08 m, whereas the sonic log has a vertical resolution of 1.07 m. Considering the findings from IODP Expedition 311 that gas hydrate generally occurs as small nodules, or in fractures or thin sandy turbidite layers, it would seem that a high-resolution measurement is more appropriate to resolve gas hydrate occurrence. Finally, during IODP Expedition 311, velocity measurements were not accompanied by porosity measurements in the same hole. As a consequence, the porosity used in the gas hydrate saturation calculation had to be a smoothed trend from a different hole at the same site. Inter-hole variability then becomes a source of error and the use of a smoothed porosity-depth trend causes a loss of vertical resolution.

Significant uncertainties arise in estimating reference no-hydrate profiles for both resistivity and velocity. Uncertainties are probably more important for the reference no-

hydrate resistivity, because of the added uncertainty in estimating the in situ salinity. However, uncertainties in no-hydrate velocity references are also significant, because they are somewhat poorly calibrated: making undisturbed velocity measurements in sediments without gas hydrate or free gas has proven to be quite difficult. Instead, the reference velocity is estimated by extrapolating deep MCS velocities to shallower depths, or by rock-physics, where the reference velocity is quite sensitive to the mineral assemblage used.

Uncertainties in the relation between velocity/resistivity and gas hydrate saturation are the most difficult to gauge, since a benchmark estimate of gas hydrate saturation is generally not available. For the resistivity study, this uncertainty is essentially the uncertainty in the Archie saturation exponent n. Sensitivity analysis has however shown that the gas hydrate saturation estimate is not very sensitive to n, so long as the value chosen is reasonable, i.e., similar to the cementation exponent m. However, in zones of highly concentrated gas hydrate or heterogeneous gas hydrate textures (e.g., nodules, veins, or fracture filling), estimates of n based on simplistic models of pore-filling gas hydrate are likely in error. For the velocity study, the uncertainty in the relation between velocity and gas hydrate saturation arises from the uncertainty in the porosity-velocity relation. This relation is more uncertain at lower porosities, since effective porosity estimates are extrapolated outside the range of observed values. As a consequence, uncertainties become greater at larger gas hydrate concentrations. The other related uncertainty is that effective porosity reduction and/or effective medium theory are potentially inadequate model representations of how gas hydrate forms, especially in

zones of highly concentrated gas hydrate or heterogeneous gas hydrate textures (e.g., nodules, veins, or fracture filling).

On average, gas hydrate saturation estimates from velocity measurements are greater in this study than those obtained from resistivity measurements (Figure 6.1). The difference is on average 10-15% of the pore space. To achieve agreement between estimates would require either decreasing velocity-based estimates or increasing resistivity-based estimates. Velocity-based gas hydrate saturation estimates could be decreased if a model incorporating some amount of cementation was used (likely valid at least in zones of concentrated gas hydrate). For a given gas hydrate concentration, such a model would predict a greater velocity enhancement than an effective porosity reduction or gas hydrate in-frame model. Lower velocity-based gas hydrate saturation estimates could also be obtained from an effective porosity reduction model, if, for a given porosity, the porosity-velocity relation predicted a larger velocity than the relation used here. Alternatively, higher resistivity-based gas hydrate saturation estimates could be obtained if in situ salinity estimates were increased. A higher in situ salinity would result in a lower reference no-hydrate resistivity, and therefore greater resistivity increases relative to the no-hydrate reference. It is important to note that in the absence of justification for higher-than-seawater in situ salinities, the in situ salinity estimate can only be increased to a maximum of that of seawater. As a consequence, the only site where a plausible salinity increase could affect resistivity-based estimates enough for agreement with velocity-based estimates is Site U1327. However, the approach outlined in Section 3.3 provided a means to estimate the in situ salinity, and suggested that such a salinity increase is not justified at U1327.

6.2 Evidence for Pervasive or Distributed Gas Hydrate Occurrence

A highly debated topic in gas hydrate studies is whether or not gas hydrate occurs pervasively in sediments above the BSR. The use of the term "pervasive" is somewhat ambiguous, in than it could signify either homogeneous gas hydrate occurrence throughout the pore space, or distributed gas hydrate relative to a given scale. During IODP Expedition 311, gas hydrate was repeatedly observed in nodules, veins, and fracture fill, and preferentially occurred in coarser-grained intervals (Riedel et al., 2006). This finding indicates that gas hydrate does not occur homogeneously throughout sediment pore space. However, this does not exclude distributed gas hydrate occurrence when viewed at a scale greater than some characteristic threshold.

Table 6.1 compares the different measurements used in this study (Site U1327) to identify gas hydrate, showing the vertical resolution of each measurement, and whether or not distributed gas hydrate is observed with that tool. It would appear that measurements with a vertical resolution smaller than a 10 cm scale (resistivity and salinity) can sample sediment containing no gas hydrate (the validity of this statement does hinge on the accuracy of the estimated no-hydrate salinity profile, calculated in Section 3.3). Conversely, measurements made on scales greater than 1 m seem to record distributed gas hydrate. It is possible then, that small scale (less than 0.10 m) heterogeneous gas hydrate occurrence (nodules, veins, fracture fill, or in sandier turbidites), averaged even over relatively small intervals (~1 m), could result in measurements of distributed gas hydrate.

Geophysical measurement	Vertical resolution (m)	Is distributed gas hydrate occurrence observed?
Core Salinity	~0.02	?, 0-3%*
High resolution log resistivity (R_t-R_o comparison)	0.05-0.08	No*
Log resistivity, 10 m running average (Full Archie analysis)	10	Yes, ~5-15%
Log velocity	1.07	Yes, ~15-20%
VSP	> 5	Yes, ~20-25%
MCS velocity	~ 70	Yes, ~15-25%
BSR AVO	~ 50	Yes, 0-23%

* *Based on calculated in situ salinity, Section 3.3.*

Table 6.1 Measurements that resolve gas hydrate at Site U1327, measurement scales, and whether or not distributed gas hydrate occurrence is observed.

The findings from IODP Expedtion 311 suggest that the regional control of fluid expulsion on gas hydrate occurrence is overprinted by local controls related to lithology, grain size, permeability, fluid advection rates, and local methane solubility (Riedel et al., 2005). However, it is difficult to entirely rule out the possibility that gas hydrate occurs pervasively, even in clays, since gas-hydrate-free clay recovered in cores could conceivably have contained a small amount of in situ gas hydrate that dissociated upon core recovery. If the core pore fluid freshening from a small amount of gas hydrate dissociation yielded a core salinity measurement that was within the uncertainty of the calculated in situ salinity, the gas hydrate associated with that small amount of freshening would inevitably go undetected.

6.3 Recommendations for Future Marine Gas Hydrate Studies

The conclusions of this thesis regarding the use of well log and seismic measurements to estimate marine gas hydrate distribution and concentration do suggest further work to be done in both resistivity and velocity studies of marine gas hydrate.

In terms of velocity studies, the Northern Cascadia gas hydrate area has been well mapped seismically (e.g., Spence et al., 1991a and b; Riedel 2001), and velocities derived from MCS are in good agreement with VSP and log velocities. It would seem that the difficulty is not in accurately measuring velocities, but rather in determining an appropriate reference velocity and porosity-velocity relation. To that end, repeated drilling at the Expedition 311 well sites is recommended, if velocity and porosity logging can be achieved in the same hole. If possible, a deep well should be drilled in the accretionary prism, far below the free gas zone, where no-hydrate/no-gas porosities and velocities can be measured. The hazards involved in drilling through the free gas zone could be mitigated if a vessel with a riser was available. In the end though, seismic velocity studies of gas hydrate are limited by the resolution at which measurements can be achieved: if the tools available only allow velocity to be measured on a meter scale, gas hydrate in small nodules, in fractures or thin sandier turbidite layers will not be resolved.

This study has clearly shown that AVO analysis of BSRs is not a valuable tool for measuring associated gas hydrate and free gas concentrations. AVO does not provide the necessary shear wave information to obtain well constrained results. Instead, shear waves should be measured using direct methods, such as shear wave logging, OBS experiments (e.g., Hobro et al., 2005; Jaiswal et al., 2006), or seafloor compliance experiments

(Willoughby and Edwards, 2000; Latychev and Edwards, 2003.). Learning about shear wave velocities in gas hydrate-bearing sediments could greatly improve our understanding of how gas hydrate forms, and how it affects the ambient sediment.

In terms of resistivity studies, this thesis has put forth a complete methodology to estimate gas hydrate concentration from log resistivity data, if the appropriate log and core data are available. These results should be complemented by regional resistivity studies, such as CSEM surveys (Yuan and Edwards, 2000; Schwalenberg et al., 2005). Even though the log resistivity analysis has yielded promising results, it must be recognized that the accuracy of the results depend on the applicability of Archie's relation for gas hydrate textures such as small nodules or fracture-filling veins that displace the ambient sediment.

Finally, it would be of great help in marine gas hydrate studies to have reliable and independent methods of measuring gas hydrate concentration. Salinity dilution and electrical resistivity are not truly independent methods, since the sediment resistivity is highly dependent on the pore fluid salinity, and seismic velocity-based estimates are not consistently reliable. Measurements of core thermal anomalies (Riedel et al., 2006) and magnetic susceptibility (Collett et al., 2005) are valuable tools, but are somewhat qualitative as of yet. One method that could provide a quantitative, accurate and independent measurement of gas hydrate concentration is the nuclear magnetic resonance (NMR) porosity logging tool (Takayama et al., 2005), which provides a direct measurement of gas-hydrate-excluding effective porosity. Although such a tool has been successfully used to measure gas hydrate in the permafrost environment, it does not, as of

yet, provide reliable results in clay-rich formations or in zones with low gas hydrate saturation ($S_h < 0.2$).

In general, much of the uncertainty involved in estimating gas hydrate concentration, regardless of the method used, comes from the lack of understanding of how gas hydrate forms in nature. The improvement of current gas hydrate formation models will require further drilling and improved coring techniques, so that sediment samples containing gas hydrate can be studied under relatively undisturbed conditions.

References

Andersen, K. K., N. Azuma, J. M. Barnola, M. Bigler, P. Biscaye, N. Caillon, J. Chappellaz, H. B. Clausen, D. DahlJensen, H. Fischer, J. Fluckiger, D. Fritzsche, Y. Fujii, K. Goto-Azuma, K. Gronvold, N. S. Gundestrup, M. Hansson, C. Huber, C. S. Hvidberg, S. J. Johnsen, U. Jonsell, J. Jouzel, S. Kipfstuhl, A. Landais, M. Leuenberger, R. Lorrain, V. Masson-Delmotte, H. Miller, H. Motoyama, H. Narita, T. Popp, S. O. Rasmussen, D. Raynaud, R. Rothlisberger, U. Ruth, D. Samyn, J. Schwander, H. Shoji, M. L. Siggard-Andersen, J. P. Steffensen, T. Stocker, A. E. Sveinbjornsdottir, A. Svensson, M. Takata, J. L. Tison, T. Thorsteinsson, O. Watanabe, F. Wilhelms, and J. W. C. White, 2004. High-resolution record of Northern Hemisphere climate extending into the last interglacial period, Nature, **431**, 147-151.

Andreassen, K., K. A. Berteussen, H. Sognnes, K. Henneberg, J. Langhammer and J. Mienert, 2003. Multicomponent ocean bottom cable data in gas hydrate investigation offshore Norway, Journal of Geophysical Research, **108**, 2399, doi:10.1029/2002JB002245.

Andreassen, K., P. E. Hart, and A. Grantz, 1995. Seismic studies of a bottom simulating reflection related to gas hydrate beneath the continental margin of the Beaufort Sea, Journal of Geophysical Research, **100**, 12,659-12,673.

Andreassen, K., P. E. Hart, and M. MacKay, 1997. Amplitude versus offset modeling of the bottom simulating reflection associated with submarine gas hydrates, Marine Geology, **137**, 25-40.

Archer, D., and B. Buffett, 2005. Time-dependent response of the global ocean clathrate reservoir to climatic and anthropogenic forcing, Geochemistry Geophysics Geosystems, **6**, Q03002.

Archie, G. E., 1942. The electrical resistivity log as an aid in determining some reservoir characteristics, Trans. AIME, **146**, 54-62.

Athy, L. F., 1930. Density, porosity, and compaction of sedimentary rocks, AAPG Bulletin, **14**, 1-24.

Augustin L, C. Barbante, P. R. F. Barnes, J. M. Barnola, M. Bigler, E. Castellano, O. Cattani, J. Chappellaz, D. DahlJensen, B. Delmonte, G. Dreyfus, G. Durand, S. Falourd, H. Fischer, J. Fluckiger, M. E. Hansson, P. Huybrechts, R. Jugie, S. J. Johnsen, J. Jouzel, P. Kaufmann, J. Kipfstuhl, F. Lambert, V. Y. Lipenkov, G. V. C. Littot, A. Longinelli, R. Lorrain, V. Maggi, V. Masson-Delmotte, H. Miller, R. Mulvaney, J. Oerlemans, H. Oerter, G. Orombelli, F. Parrenin, D. A. Peel, J. R. Petit, D. Raynaud, C. Ritz, U. Ruth, J. Schwander, U. Siegenthaler, R. Souchez, B. Stauffer, J. P. Steffensen, B. Stenni, T. F. Stocker, I. E. Tabacco, R. Udisti, R. S. W. van de Wal, M. van den Broeke, J. Weiss, F. Wilhelms, J. G. Winther, E. W. Wolff, and M. Zucchelli, 2004. Eight glacial cycles from an Antarctic ice core, Nature, **429**, 623-628.

Avseth, P., T. Mukerji, A. Jorstad, G. Mavko, and T. Veggerland, 2001. Seismic reservoir mapping from 3-D AVO in a North Sea turbidite system, Geophysics, **66**, 1157-1176.

Blum, P. 1997. Physical properties handbook: a guide to the shipboard measurement of physical properties of deep-sea cores, ODP Tech. Note, **26**.

Bondevik, S. J. I. Svendsen, G. Johsen, J. Mangerud, and P. E. Kaland, 1997. The Storegga tsunami along the Norwegian coast, its age and run-up, Boreas, **26**, 29-53.

Booth, J. S., W. J. Winters, and W. P. Dillon, 1994. Circumstantial evidence of gas hydrate and slope failure association on the United States Atlantic continental margin, *in* Sloan, E. D., Happel, J., and Hnatow, M. A. (eds.), Natural Gas Hydrates: Annuals of the New York Academy of Sciences, **715**, 487-489.

BP Statistical Review of World Energy, 2006. Accessed online 10/03/2006, http://www.bp.com/statisticalreview

Buland, A., and H. Omre, 2003. Bayesian linearized AVO inversion, Geophysics, **68**, 185-198.

Bünz, S., J. Mienert, and C Berndt, 2003. Geologic controls on the Storegga gas hydrate system of the mid-Norwegian continental margin, Earth and Planetary Science Letters, **209**, 291-307.

Bünz, S., J. Minert, M. Vanneste, and K. Andreassen, 2005. Gas hydrates at the Storegga Slide: Constraints from an analysis of Multicomponent, wide-angle seismic data, Geophysics, **70**, B19-B34.

Chand, S., T. A. Minshull, D. Gei, and H. M. Carcione, 2004. Elastic velocity models for gas-hydrate-bearing sediments – a comparison, Geophysical Journal International, **159**, 573-590.

Carcione, J. M. and U. Tinivella, 2000. Bottom-simulating reflectors: seismic velocities and AVO effects, Geophysics, **65**, 54-67.

Castagna, J. P., M. L. Batzle, and R. L. Eastwood, 1985. Relationships between compressional-wave and shear-wave velocities in clastic silicate rocks, Geophysics, **50**, 571-581.

Chapman, N. R., J. F. Gettrust, R. Walia, D. Hannay, G. D. Spence, W. T. Wood, and R. D. Hyndman, 2002., High-resolution, deep-towed, multichannel seismic survey of deep-sea gas hydrates off western Canada, Geophysics, **67**, 1038-1047.

Collett, T. S. 2000. Natural gas hydrate as a potential energy resource, *in* M. D. Max, ed., Natural Gas Hydrate in Oceanic and Permafrost Environments, Kluwer Academic Publications.

Collett, T. S., 2001. A review of well-log analysis techniques used to assess gas-hydrate-bearing reservoirs, *in* C. K. Paull and W. P. Dillon, eds., Natural gas hydrates: occurrence, distribution, detection, American Geophysical Union Monographs **124**, 189-210.

Collett, T. S., and J. Ladd, 2000. Detection of gas hydrate with downhole logs and assessment of gas hydrate concentrations (saturations) and gas volumes on the Blake Ridge with electrical resistivity data: Proceedings of the Ocean Drilling Program, Scientific Results, **164**, 179-191.

Collett, T. S., R. E. Lewis, and S. R. Dallimore, 2005. JAPEX/JNOC/GSC et al. Mallik 5L-38 gas hydrate production research well downhole well-log and core montages, *in* S. R. Dallimore and T. S. Collett, eds., Scientific results from the Mallik 2002 gas hydrate production research well program, MacKenzie Delta, Northwest Territories, Canada, Geological Survey of Canada Bulletin, **585.**

Dallimore, S.R., and T. S. Collett, 2005. Summary and implications of the Mallik 2002 gas hydrate production research well program, *in* Dallimore, S.R., and T. S. Collett, eds., Scientific results from the Mallik 2002 gas hydrate production research well program, MacKenzie Delta, Northwest Territories, Canada, Geological Survey of Canada Bulletin, **585**, 1-36.

Davis, E. E., and, R. D. Hyndman, 1989. Accretion and recent deformation of sediments along the northern Cascadia subduction zone, Geological Society of America Bulletin, **101**, 1465-1480.

Dillon, W. P., M. W. Lee, K. Felhaber, and D. F. Coleman, 1993. Gas hydrates on the Atlantic continental margin of the United States – controls on concentration, *in* Howell, D. G. (ed.), The Future of Energy Gases, U. S. Geological Survey Professional Paper, **1570**, 313-330.

Dillon, W. P., J. W. Nealson, M. H. Taylor, M. W. Lee, R. M. Drury, and C. H. Anton, 2001. Seafloor collapse and methane venting associated with gas hydrate on the Blake Ridge – causes and implications to seafloor stability and methane release, in C. K. Paull and W. P. Dillon (eds.), Natural Gas Hydrates: Occurrence, Distribution, and Detection, 211-233.

Dix, C. H., 1955. Seismic velocities from surface measurements, Geophysics, **20**, 68-86.

Dosso, S. E., 2002. Quantifying uncertainties in geoacoustic inversion I: A fast Gibbs sampler approach, Journal of the Acoustical Society of America, **111**, 129-142.

Dosso, S. E., and P. L. Nielsen, 2002. Quantifying uncertainties in geoacoustic inversion II, Application to a broadband shallow-water experiment, Journal of the Acoustical Society of America, **111**, 142-159.

Dosso, S. E., M. J. Wilmut, and A. L. Lapinski, 2001. An adaptive hybrid algorithm for geoacoustic inversion, IEEE Journal of Oceanic Engineering, **26**, 324-336.

Drufuca, G., and A. Mazzotti, 1995. Ambiguities in AVO inversion of reflections from gas-sand, Geophysics: **60**, 134-141.

Duren, R. E., 1991. Seismic Range Equation, Geophysics, **56**, 1015-1026.

Dvorkin, J. and A. Nur, 1993. Rock physics for characterization of gas hydrates, *in* The future of energy gases, U.S. Geological Survey Professional Paper, **1570**.

Dvorkin, J., M. Prasad, A. Sakai, and D. Lavoie, 1999. Elasticity of marine sediments: rock physics modeling, Geophysical Research Letters, **26**, 1781-1784.

Ecker, C., J. Dvorkin, and A. Nur, 1998. Sediments with gas hydrates: Internal structure from seismic AVO, Geophysics, **68**, 1659-1669.

Fatti, J. L., G. C. Smith, P. J. Vail, P. J. Strauss, and P. R. Levitt, 1994. Detection of gas in sandstone reservoirs using AVO analysis: A 3-D seismic case history using the Geostack technique, Geophysics, **59**, 1362-1376.

Fink, C. R., and G. D. Spence, 1999. Methane hydrate distribution offshore Vancouver Island from detailed single channel seismic reflection data, Journal of Geophysical Research, **104**, 2909-2922.

Fofonoff, N. P., 1985. Physical properties of seawater: a new salinity scale and equation of state for seawater, Journal of Geophysical Research, **90**, 3332-3342.

Fyke, J. G., 2005. The effect of climate change on the marine methane hydrate stability zone, M.Sc. Thesis, University of Victoria.

Gassmann, F., 1951. On elasticity of porous media, Vierteljahresschrift der Naturforschenden Gesellschaft Zürich, **96**, 1-13.

Gettrust, J. N. R. Chapman, R. Walia, W. Wood, D. Hannay, D. Lindwall, G. D. Spence, K. Louden, and R. D. Hyndman, 1999. High resolution seismic studies of deep sea gas hydrate using the DTAGS deep towed multichannel system, EOS Transactions, AGU, 80, 38, 439-440.

Gilks, W. R., S. Richardson, and G. J. Spiegelhalter, 1996. Markov chain Monte Carlo in practice, Chapman and Hall.

Gregory, A. R., 1976. Fluid saturation effects on dynamic elastic properties of sedimentary rocks, Geophysics, **41**, 895-921.

Goldberg, D., R. H. Wilkins, and D. Moos, 1986. Seismic modeling of diagenetic effects in Cenozoic marine sediments, Deep Sea Drilling Project, Initial Reports, **95**, 589-599.

Hale, D., 1984. Dip-moveout by Fourier transform, Geophysics, **49**, 741-757.

Hamilton, E. L., 1976. Variations of density and porosity with depth in deep-sea sediments, Journal of Sedimentary Petrology, **46**, 280-300.

Hampson D., B. Russell, and M. Cardamone, 2004. Uncertainty in AVO – How can we measure it?, CSEG Recorder, **29**, no.3, 5-11.

Haq, B. L., 2000. Climatic Impact of Natural Gas Hydrate, *in* M. D. Max (ed.), Natural Gas Hydrate in Oceanic and Permafrost Environments, Kluwer Academic Publishers, 137-148.

Harvey, L. D. D., and Z. Huang, 1995. Evaluation of the potential impact of methane clathrate destabilization on future warming, Journal of Geophysical Research, **100**, 2905-2926.

Hearst, J. R., P. H. Nelson, F. L. Paillet, 2000. Well logging for physical properties, John Wiley & Sons Ltd.

Helgerud, M. B., 2001. Wave speeds in gas hydrate and sediments containing gas hydrate: a laboratory and modeling study, Ph.D. thesis, Stanford University.

Hesse, R., 2003. Pore water anomalies of submarine gas hydrate zones as a tool to assess hydrate abundance and distribution in the subsurface. What have we learned in the past decade?, Earth Science Reviews, **61**, 149-179.

Hilfer, R., 1991. Geometric and dielectric characterization of porous media, Physical review, **44**, 60-75.

Hill, R., 1952. The elastic behavior of crystalline aggregate, Proc. Physical Soc., **A65**, 349-354.

Hobro, J. W. D., T. A. Minshull, S. C. Singh, and S. Chand, 2005. A three-dimensional seismic tomography study of the gas hydrate stability zone, offshore Vancouver Island, 2005. Journal of Geophysical Research, 110, B09102, doi:10.1029/2004JB003477.

Hyndman, R. D., and E. E. Davis, 1992. A mechanism for the formation of methane hydrate and seafloor bottom-simulating reflectors by vertical fluid expulsion, Journal of Geophysical Research, **97**, 7025-7041.

Hyndman, R. D., G. F. Moore, and K. Moran, 1993. Velocity, porosity, and pore-fluid loss from the Nankai subduction zone accretionary prism, Proceedings of the Ocean Drilling Program, Scientific Results, **131**, 211-220.

Hyndman, R. D., and G. D. Spence, 1992. A seismic study of methane hydrate bottom simulating reflectors, Journal of Geophysical Research, **97**, 6683-6698.

Hyndman, R. D., G. D. Spence, N. R. Chapman, M. Riedel, and R. N. Edwards, 2001. Geophysical Studies of Marine Gas Hydrate in Northern Cascadia, *in* C. K. Paull and W. P. Dillon, eds., Natural gas hydrates: occurrence, distribution, detection, American Geophysical Union Monographs **124**, 273-295.

Hyndman, R. D., T. Yuan, and K. Moran, 1999. The concentration of deep sea gas hydrates from downhole electrical resistivity logs and laboratory data, Earth and Planetary Science Letters, **172**, 167-177.

Ioannidis, M. A., M. J. Kwiecien, and I. Chatzis, 1997. Electrical conductivity and percolation aspects of statistically homogeneous porous media, Transport in porous media, **29**, 61-83.

Jackson, P. D., D. Taylor-Smith, and P. N. Stanford, 1978. Resistivity-porosity-particle shape for marine sands, Geophysics, **43**, 1250-1268.

Jaiswal, P., C. A. Zelt, and I. A. Pecher, 2006. Seismic characterization of a gas hydrate system in the Gulf of Mexico using wide-aperture data, Geophysical Journal International, **165**, 108-120.

Kastner, M., K. A. Kvenvolden, M. J. Whiticar, A. Camerlenghi, and T. D. Lorenson, 1995. Relation between pore fluid chemistry and gas hydrate associated with bottom-simulating reflectors at the Cascadia Margin, Sites 889 and 892, Proceedings of the Ocean Drilling Program, Scientific Results, **146**, 175-187.

Kayen, R. E. and H. J. Lee, 1991. Pleistocene slope instability of gas hydrate-ladden sediment of the Beaufort Sea margin, Marine Geotech., **10**, 125-141.

Kvenvolden, K. 1993. Gas hydrates – geologic perspective and global change, Reviews of Geophysics, **31**, 173-187.

Kvenvolden, K. A., G. D. Ginsburgh, and V. A. Soloviev, 1993. Worldwide distribution of subaquatic gas hydrates, Geo-Marine Letters, **13**, 32-40.

Latychev, K., and R. N. Edwards, 2003. On the compliance method and the assessment of three-dimensional gas hydrate deposits, Geophysical Journal International, 155, 923-952.

Lee, M. W., D. R. Hutchinson, W. P. Dillon, J. J. Miller, W. F. Agena, and B. A. Swift, 1993. Method of estimating the amount of in situ gas hydrates in deep marine sediments, Marine and Petroleum Geology, **10**, 496-506.

Malinverno, A. and V. A. Briggs, 2004. Expanded uncertainty quantifications in inverse problems: hierarchical Bayes and empirical Bayes, Geophysics, **69**, 1005-1016.

Mazzotti, A. and E. Zamboni, 2003. Petrophysical inversion of AVA data, Geophysical Prospecting, **51**, 517-530.

Milkov, A. V., 2004. Global estimates of hydrate-bound gas in marine sediments: how much is really out there?, Earth-Science Reviews, **66**, 183-197.

Mindlin, R. D., 1949. Compliance of elastic bodies in contact, Trans. ASME, **71**, A-259.

Minshull, T. A., C. S. Singh and G. K. Westbrook, 1994. Seismic velocity structure at a gas hydrate reflector, offshore western Columbia, full waveform inversion, Journal of Geophysical Research, **99**, 4715-4734.

Ostrander, W. J., 1984. Plane-wave reflection coefficients for gas sands at nonnormal angles of incidence, Geophysics, **49**, 1637-1648.

Paull, C. K., W. III, Ussler, and W. P. Dillon, 1991. Is the extent of glaciation limited by marine gas-hydrates?, Geophysical Research Letters, **18**, 432-434.

Paull, C. K., W. III, Ussler, and W. P. Dillon, 2000. Potential role of gas hydrate decomposition in generating submarine slope failures, *in* M. D. Max (ed.), Natural Gas Hydrate in Oceanic and Permafrost Environments, Kluwer Academic Publishers, 149-156.

Pearson, C. F., P. M. Halleck, P. L. McGulre, R. Hermes, and M. Matthews, 1983. Natural gas hydrate; a review of in situ properties, Journal of Physical Chemistry, **87**, 4180-4185.

Pecher, I. A., T. A. Minshull, S. C. Singh, and R. vonHuene, 1996. Velocity structure of a bottom simulating reflector offshore Peru: results from full waveform inversion, Earth and Planetary Sciences Letters, **139**, 459-469.

Petit, J.R., J. Jouzel, D. Raynaud, N. I. Barkov, J.-M. Barnola, I. Basile, M. Benders, J. Chappellaz, M. Davis, G. Delague, M. Delmotte, V. M. Kotlyakov, M. Legrand, V. Y. Lipenkov, C. Lorius, L. Pepin, C. Ritz, E. Saltzman, and M. Stievenard, 1999. Climate and atmospheric history of the past 420,000 years from the Vostok ice core, Antarctica, Nature, **399**, 429-436.

Reuss, A., 1929. Berechnung der Fliessgrenze von Mischkristallen auf Grund der Plastizitätsbedingung fur Einkristalle, Zeitschrift fur Angewandte Mathematik und Mechanik, **9**, 49-58.

Riddihough, R. P., 1984. Recent movements of the Juan de Fuca plate system, Journal of Geophysical Research, **89**, 6980-6994.

Riedel, M., 2001. 3-D seismic investigations of Northern Cascadia marine gas hydrates, Ph.D. Thesis, University of Victoria.

Riedel, M., T. S. Collett, and R. D. Hyndman, 2005. Gas hydrate concentration estimates from chlorinity, electrical resistivity and seismic velocity, Geological Survey of Canada Open File Report, **4934**.

Riedel, M., T. S. Collett, M. J. Malone, and the Expedition311 Scientists, 2006. Proceedings of the Integrated Ocean Drilling Program, Expedition Report, **311,** doi:10.2204/iodp.proc.311.101.2006. Accessed online 11/01/2006, http://iodp.tamu.edu/publications/exp311/311toc.htm

Riedel, M., Dosso, S. E., and Beran, L., 2003. Uncertainty estimation for amplitude variation with offset (AVO) inversion, Geophysics, **68**, 1485-1496.

Riedel, M., R. D. Hyndman, G. D. Spence, and N. R. Chapman, 2002. Seismic investigations of a vent field associated with gas hydrates, offshore Vancouver Island, Journal of Geophysical Research, **107**, 2200.

Schwalenberg, K., E. C. Willoughby, R. Mir, and R. N. Edwards, 2005. Marine gas hydrate electromagnetic signatures in Cascadia and their correlation with seismic blank zones, First Break, **23**, 57-63.

Sen, M. K., and P. L. Stoffa, 1996. Bayesian inference, Gibbs' sampler and uncertainty estimation in geophysical inversion, Geophysical Prospecting, **44**, 313-350.

Sheriff R. E., and L. P. Geldart, 1982. Exploration seismology volume 1, History, Theory, Data Acquisition, Cambridge University Press.

Singh, S. C., and T. A. Minshull, 1994. Velocity structure of a gas hydrate reflector at Ocean Drilling Program site 889 from a global seismic waveform inversion, Journal of Geophysical Research, **99**, 24,221-24,233.

Smith, G. C., and P. M. Gidlow, 1987. Weighted stacking for rock property estimation and detection of gas, Geophysical Prospecting, **35**, 993-1014.

Spapenberg, E., 2001. Modeling of the influence of gas hydrate content on the electrical properties of porous sediments, Journal of Geophysical Research, **106**, 6535-6548.

Spence, G. D., R. D. Hyndman, E. E. Davis, and C. J. Yorath, 1991a. Marine multichannel seismic reflection data across the continental margin of Vancouver Island, Geological Survey of Canada Open File Report, **2391**.

Spence, G. D., R. D. Hyndman, E. E. Davis, and C. J. Yorath, 1991b. Seismic structure of the northern Cascadia accretionary prism: Evidence from new multichannel seismic reflection data, *in* R. Meissner, L. Brown, H.-J. Durbaum, W. Franks, K. Fuchs, and F. Seifert, eds., Continental Lithosphere: Deep Seismic Reflections, Geodynamics Series, **22**, 257-263.

Stewart, R. R., J. E. Gaiser, R. J. Brown, and D. C. Lawton, 2002. Converted wave seismic exploration: Methods, Geophysics, **67**, 1348-1363.

Swanson, B. F., 1979. Visualizing pores and nonwetting phase in porous rock, J. Petr. Tech., **32**, 1459-1464.

Takayama, T., M. Nishi, T. Uchida, K. Akihisa, F. Sawamura, and K. Ochiai, 2005. Gas hydrate saturation analysis using density and nuclear magnetic resonance logs from the JAPEX/JNOC/GSC et al. Mallik 5L-38 gas hydrate production research well, *in* S. R. Dallimore and T. S. Collett, eds., Scientific results from the Mallik 2002 gas hydrate production research well program, MacKenzie Delta, Northwest Territories, Canada, Geological Survey of Canada Bulletin, **585.**

Tarantola, A., 1987. Inverse problem theory: Methods for data fitting and model parameter estimation, Elsevier Science Publishers Co.

Tertzakian, P., 2006. A thousand barrels a second, McGraw-Hill.

Tréhu, A. M., G. Bohrmann, F. Rack, M. E. Torres, and Leg 204 Scientific Party, 2003. Proceedings of the Ocean Drilling Program, Initial Reports, **204**.

Westbrook, G. K., B. Carson, R. Musgrave, and Shipboard Scientific Party, 1994. Proceedings of the Ocean Drilling Program, Initial Reports, **146**.

Willoughby, E. C., and R. N. Edwards, 2000. Shear velocities in Cascadia from seafloor compliance measurements, Geophysical Research Letters, **27**, 1021-1024.

Willoughby, E. C., K. Latychev, R. N. Edwards, K. Schwalenberg, and R. D. Hyndman, 2006. Seafloor compliance imaging of marine gas hydrate deposits and cold vent structures, Journal of Geophysical Research, submitted.

Winsauer, W. O., H. M. Shearin, Jr., P. H. Mason, et al., 1952. Resistivity of brine-saturated sands in relation to pore geometry, Bulletin of the AAPG, **36**, 253-277.

Winters, W. J., 2000. Data report: effects of drying methods and temperatures in water content and porosity of sediment from the Blake Ridge, Proceedings of the Ocean Drilling Program, Scientific Results, **164**, 431-34.

Wood, A. B., 1941. A text book of sound, Macmillan, 235-248.

Wood, W. T., W. S. Holbrook, and H. Hoskins, 2000. In situ measurements of P-wave attenuation in the methane hydrate- and gas-bearing sediments of the Blake Ridge, Proceedings of the Ocean Drilling Program, Scientific Results, **164**, 365-272.

Wyllie, M. R. J., A. R. Gregory, and G. H. F. Gardner, 1958. An experimental investigation of factors affecting elastic wave velocities in porous media, Geophysics, **23**, 459-493.

Yuan, J., and R. N. Edwards, 2000. The assessment of marine gas hydrates through electrical remote sounding: Hydrate without a BSR?, Geophysical Research Letters, **27**, 2397-2400.

Yuan, T., R.D. Hyndman, G. D. Spence, and B. Desmons, 1996. Velocity structure of a bottom-simulating reflector and deep sea gas hydrate concentrations on the Cascadia continental slope, Journal of Geophysical Research, **101**, 13655-13671.

Yuan, T., G. D. Spence, and R. D. Hyndman, 1994. Seismic velocities and inferred porosities in the accretionary wedge sediments at the Cascadia margin, Journal of Geophysical Research, **99**, 4413-4427.

Yuan, T., G. D. Spence, R. D. Hyndman, T. A. Minshull and S. C. Singh, 1999. Seismic velocity studies of a gas hydrate bottom-simulating reflector on the northern Cascadia continental margin, Amplitude modeling and full waveform inversion: Journal of Geophysical Research, **104**, 1179-1191.

Zoeppritz, R., 1919. On the reflection and propagation of seismic waves, Erdbebenwellen VIIIB; Göttinger Nachrichten, **I**, 66-84.

Appendix

Model for Elastic Properties of Gas Hydrate-Bearing Sediments

This section presents the rock-physics model used in this study to predict the elastic properties of gas hydrate-bearing marine sediments. The parameters used to determine the elastic properties of an effective medium consisting of gas hydrate-bearing sediments are the elastic properties of the sediment constituents, the porosity, and the effective pressure (depth). The model was developed by Helgerud (2001), who provides a detailed description of the model.

A.1 Baseline Model for Fully Water-Saturated Sediments

A baseline model for fully water-saturated sediments, developed by Dvorkin et al. (1999) is taken as a starting point for the effective medium modeling of elastic parameters. For porosities (φ) above the critical porosity (φ_c, taken as 0.36), the bulk (K_{dry}) and shear (G_{dry}) moduli of dry marine sediments can be expressed as:

$$K_{dry} = \left[\frac{\frac{1-\varphi}{1-\varphi_c}}{K_{HM} + \frac{4}{3} G_{HM}} + \frac{\frac{\varphi-\varphi_c}{1-\varphi_c}}{\frac{4}{3} G_{HM}} \right]^{-1} - \frac{4}{3} G_{HM}, \qquad \text{(A.1)}$$

$$G_{dry} = \left[\frac{\frac{1-\varphi}{1-\varphi_c}}{G_{HM} + Z} + \frac{\frac{\varphi-\varphi_c}{1-\varphi_c}}{Z} \right]^{-1} - Z, \tag{A.2}$$

$$Z = \frac{G_{HM}}{6} \left(\frac{9K_{HM} + 8G_{HM}}{K_{HM} + 2G_{HM}} \right),$$

where the effective bulk (K_{HM}) and shear (G_{HM}) moduli of the dry rock frame at critical porosity is calculated from Hertz-Mindlin theory (Mindlin, 1949):

$$K_{HM} = \left[\frac{n^2 (1-\varphi_c)^2 G^2}{18\pi^2 (1-\nu)^2} P_{eff} \right]^{1/3}, \tag{A.3}$$

$$G_{HM} = \frac{5-4\nu}{5(2-\nu)} \left[\frac{3n^2 (1-\varphi_c)^2 G^2}{2\pi^2 (1-\nu)^2} P_{eff} \right]^{1/3}, \tag{A.4}$$

$$\nu = \frac{3K - 2G}{2(2K + G)}.$$

The average number of grain contacts n is taken to be 8. Note that Equations A.1 to A.4 are not particularly sensitive to the choice of φ_c and n, so long as their chosen values are physically reasonable. The effective pressure P_{eff} is calculated as the difference between lithostatic and hydrostatic pressure:

$$P_{eff} = Dg(\rho_b - \rho_w), \tag{A.5}$$

where D is the depth below the seafloor, g is the gravitational acceleration, and ρ_b and ρ_w are the densities of the bulk sediment and water.

The bulk (K) and shear (G) moduli of the solid phase are calculated for mixed mineralogy from those of individual constituents, using Hill's (1952) average formula:

$$K = \frac{1}{2} \left[\sum_{i=1}^{m} f_i K_i + \left(\sum_{i=1}^{m} \frac{f_i}{K_i} \right)^{-1} \right], \tag{A.6}$$

$$G = \frac{1}{2}\left[\sum_{i=1}^{m} f_i G_i + \left(\sum_{i=1}^{m} \frac{f_i}{G_i}\right)^{-1}\right], \tag{A.7}$$

where m is the number of mineral constituents, f_i is the volumetric fraction of the i-th constituent of the solid phase, and K_i and G_i are the bulk and shear moduli of the i-th constituent. The solid phase density is taken as the volumetrically weighted average of individual mineral constituent densities ρ_i:

$$\rho_{solid} = \sum_{i=1}^{m} f_i \rho_i \,. \tag{A.8}$$

For a sediment saturated with pore fluid of bulk modulus K_f, the bulk (K_{sat}) and shear (G_{sat}) moduli are calculated from Gassmann's (1951) equations:

$$K_{sat} = K\frac{\varphi K_{dry} - (1-\varphi)K_f K_{dry}/K + K_f}{(1-\varphi)K_f + \varphi K - K_f K_{dry}/K}, \tag{A.9}$$

$$G_{sat} = G_{dry} \,. \tag{A.10}$$

P- and S-wave velocities are then calculated from the fluid-saturated elastic moduli:

$$V_p = \sqrt{\frac{K_{sat} + \frac{4}{3}G_{sat}}{\rho_b}}, \tag{A.11}$$

$$V_s = \sqrt{\frac{G_{sat}}{\rho_b}}, \tag{A.12}$$

where the bulk density ρ_b is:

$$\rho_b = \varphi\rho_w + (1-\varphi)\rho_{solid} \,. \tag{A.13}$$

A.2 Gas Hydrate Formation in the Pore Fluid

If the presence of gas hydrate in marine sediments is accounted for by assuming that gas hydrate forms in the pore space such that it is suspended in the pore fluid, it affects only the elastic moduli of the pore fluid and density; it does not affect the stiffness of the frame. The effective bulk modulus of the composite pore fluid $\overline{K}_f$ is calculated using the Reuss (1929) isostress average of the water (K_w) and gas hydrate (K_h) bulk moduli:

$$\overline{K}_f = \left[\frac{S_h}{K_h} + \frac{1 - S_h}{K_w} \right]^{-1}, \qquad \text{(A.14)}$$

where S_h is the volumetric fraction of the pore space occupied by gas hydrate.

A.3 Gas Hydrate Formation in the Sediment Frame

If gas hydrate is modeled to form as part of the load-bearing sediment frame, the dry sediment bulk and shear moduli must be recalculated. The new porosity is;

$$\overline{\varphi} = \varphi(1 - S_h). \qquad \text{(A.15)}$$

The effective solid phase moduli of the gas hydrate and sediment mixture are recalculated from Equation A.6 and A.7, by replacing f_i with:

$$\bar{f}_i = f_i \frac{1 - \varphi}{1 - \overline{\varphi}}, \qquad \text{(A.16)}$$

And the gas hydrate is considered as an additional component of the mineral mix with

$$\bar{f}_h = \frac{S_h}{1 - \overline{\varphi}}. \qquad \text{(A.17)}$$

A.4 Free Gas Occurrence in the Pore Fluid

The occurrence of free gas in the pore fluid is treated using the same approach as the gas hydrate in-pore model (Section A.2). In this case, the effective bulk modulus of the composite pore fluid is the Reuss (1929) isostress average of the water (K_w) and gas (K_g) bulk moduli:

$$\overline{K}_f = \left[\frac{S_w}{K_w} + \frac{1 - S_w}{K_g} \right]^{-1}, \tag{A.18}$$

where S_w is the volumetric fraction of the pore space occupied by free gas. The bulk density must also be recalculated from:

$$\rho_b = \varphi\left(S_w \rho_w + (1 - S_w)\rho_g\right) + (1 - \varphi)\rho_{solid}, \tag{A.19}$$

where ρ_g is the density of the free gas.